Observations and Modeling of Tropical Planetary Atmospheres

Thesis by

Anne Laraia

In Partial Fulfillment of the Requirements

for the Degree of

Doctor of Philosophy

California Institute of Technology

Pasadena, California

2016

(Defended June 22, 2015)

To my brother Chris and my sister Emma:

Always together, never apart, maybe in distance but never at heart.

Acknowledgments

I could not have completed this thesis without the support of my advisors, colleagues, friends and family. I had the great fortune of working with three faculty members during my time at Caltech: Simona Bordoni, Andy Ingersoll and Tapio Schneider. I'd like to thank Simona for taking me on as a third year student and giving me guidance, independence and for being a role model. Andy Ingersoll encouraged and guided me in a project in planetary science even though it was out of my discipline. Thank you to Tapio Schnedier for your continued support over the last 5 years. I'd also like to thank Paul Wennberg for your helpful feedback throughout my PhD career and Andy Thompson for your willingness to join my committee on short notice. I am deeply grateful for all of the opportunities, support and guidance with which my committee has provided me during my time at Caltech.

Early on in my PhD experience I received a ton of help from older Caltech students, post-docs and staff scientists. I'd like to thank Xavier Levine, Tim Merlis, and Yohai Kaspi for helping me get started running the GCM. Special thanks to Junjun Liu who provided a lot of guidance (and MATLAB code!) to me for my superrotation project. Shawn Ewald got me started and answered continuous questions about IDL for my Saturn project.

I have had the pleasure of sharing an office with some great students throughout the years. I'd like to give a special thanks to Toby Bischoff, Jennifer Walker and Jinqiang Chen for being great office mates who I've become close with over the years. It has been a pleasure sitting next to you and getting to know you.

Thanks to Lindsay Yee, who started off as an older graduate student lending advice and support and became a lifelong friend. I'd like to give another shout out to Matt Coggon, who has been such a great friend to me. You have always been such a reliable person that I can trust and whom I admire.

The Women Mentoring Women Program at Caltech was and is my safety net. Through this program I was connected with my mentor, Jill Craven, who is my Caltech sister. I treasure our friendship. Thank you so much for being there for me for the past five years. I don't think I could have done it without the constant laughing together. You really brightened my life here.

None of this would have been possible without my loving and supportive family. Thank you Mom and Dad for encouraging me and always being there for me. Thanks to my brother Chris and my sister Emma for your visits, phone calls and love throughout this five-year journey. I'm dedicating this to the two of you.

Lastly, I'd like to thank my incredible husband Steve Gardner, who embarked on a long-distance relationship with me for 2.5 years when I decided to go to Caltech. While I was a student at Caltech we got engaged, moved in together, and got married. These five years will be special to me in so many ways, and you are a huge part of that. Thank you for moving across the country to be with me, and for loving me and supporting me through my ups and downs as a graduate student.

Abstract

This thesis is a comprised of three different projects within the topic of tropical atmospheric dynamics. First, I analyze observations of thermal radiation from Saturn's atmosphere and from them, determine the latitudinal distribution of ammonia vapor near the 1.5-bar pressure level. The most prominent feature of the observations is the high brightness temperature of Saturn's subtropical latitudes on either side of the equator. After comparing the observations to a microwave radiative transfer model, I find that these subtropical bands require very low ammonia relative humidity below the ammonia cloud layer in order to achieve the high brightness temperatures observed. We suggest that these bright subtropical bands represent dry zones created by a meridionally overturning circulation.

Second, I use a dry atmospheric general circulation model to study equatorial superrotation in terrestrial atmospheres. A wide range of atmospheres are simulated by varying three parameters: the pole-equator radiative equilibrium temperature contrast, the convective lapse rate, and the planetary rotation rate. A scaling theory is developed that establishes conditions under which superrotation occurs in terrestrial atmospheres. The scaling arguments show that superrotation is favored when the off-equatorial baroclinicity and planetary rotation rates are low. Similarly, superrotation is favored when the convective heating strengthens, which may account for the superrotation seen in extreme global-warming simulations.

Third, I use a moist slab-ocean general circulation model to study the impact of a zonally-symmetric continent on the distribution of monsoonal precipitation. I

show that adding a hemispheric asymmetry in surface heat capacity is sufficient to cause symmetry breaking in both the spatial and temporal distribution of precipitation. This spatial symmetry breaking can be understood from a large-scale energetic perspective, while the temporal symmetry breaking requires consideration of the dynamical response to the heat capacity asymmetry and the seasonal cycle of insolation. Interestingly, the idealized monsoonal precipitation bears resemblance to precipitation in the Indian monsoon sector, suggesting that this work may provide insight into the causes of the temporally asymmetric distribution of precipitation over southeast Asia.

Contents

List of Figures

List of Tables

Chapter 1

Introduction

Earth's tropical atmosphere, residing in the region surrounding the equator, has very different dynamical characteristics than those of other latitudes and is significantly less well understood. In the tropics, horizontal atmospheric temperature and pressure gradients are constrained to be small outside of the boundary layer, and the effects of planetary rotation are smallest at the equator where the Coriolis force goes to zero. Thus, quasi-geostrophy that governs middle and high latitude dynamics is not appropriate for the tropics. Also, unlike middle and high latitudes, diabatic heating plays a large role in the energy budget in the tropics.

Earth's tropics is characterized by an annually-averaged excess of net radiation: more incoming solar radiation is absorbed than outgoing longwave radiation emitted (Fig. 1.1). The extratropics, on the other hand, have a deficit of net radiation. This occurs because spherical planetary bodies with Earth-like obliquities are differentially heated by the sun such that, over the course of a year, the equator receives more sunlight than the poles. To balance this excess radiation in the tropics and deficit at higher latitudes, the atmosphere and ocean must transport energy from the equator toward the poles. On Earth, the poleward energy transport of the atmosphere is accomplished by the meridionally overturning circulation in the tropics and by weather systems, or eddies, in midlatitudes.

In 1735, Hadley provided the first comprehensive theory of the tropical overturn-

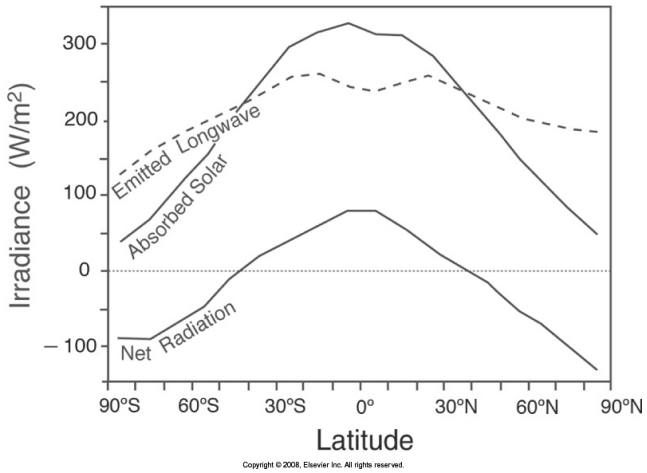

Figure 1.1: Absorbed shortwave, outgoing longwave, and net radiation (W m^{-2}) in Earth's annual mean as a function of latitude. Net radiation is the absorbed solar minus the emitted longwave radiation. Figure is from Marshall and Plumb (2007).

ing circulation, with solar heating in the tropics causing the air to rise, flow poleward at upper levels, and sink by differential cooling at higher latitudes. The return flow occurs at the surface, where the effects of friction balance the Coriolis force, causing the surface winds to be deflected to the west. He postulated that angular momentum conservation in the upper branch of the circulation causes zonal winds to become more westerly as the air moves poleward, and that when the air sinks the westerlies are transferred to the surface. Drag on the surface easterlies transfers angular momentum from the surface to the atmosphere in low latitudes, and drag on the westerlies in higher latitudes transfers it back to the surface. Thus Earth's angular momentum is conserved. This thermally direct circulation therefore transports both heat and angular momentum from the tropics to higher latitudes. Since then the importance of large-scale eddies in maintaining angular-momentum conservation has been demonstrated. These eddies make up much of the atmospheric transport of heat and momentum in midlatitudes.

However, Hadley wasn't too far off: A meridional cross-section of Earth's tropical atmosphere in the annual mean reveals two overturning cells, known as Hadley cells, that transport heat and momentum from the equator toward the poles. In the zonal

direction, there are weak easterlies at all levels extending from 30°N to 30°S, accompanied by weak meridional temperature gradients. The ascending branch of Hadley cell, located at the boundary of the two cells, is the intertropical convergence zone (ITCZ). The ITCZ is a band of deep convection (e.g., thunderstorms) that moves north and south in the tropics with the seasons. Monsoons are a manifestation of the seasonal migrations of the ITCZ over subtropical continents, whereby an onset of intense rainfall occurs that persists through the summer months. Most of the annually-averaged rainfall on Earth falls in tropical latitudes, which makes understanding tropical atmospheric dynamics and how it changes with climate a priority.

Although there is pressing motivation to understand tropical dynamics on our own planet, tropical atmospheric dynamics is an interesting fluid dynamical problem in general. The different sizes, surfaces, rotation rates, orbital parameters, and chemical makeups of the planets contribute to the wide range of atmospheres present in our solar system. Venus, Jupiter and Saturn, for example, have superrotating atmospheres, meaning that the atmosphere is spinning faster than the solid-body planet (or the core of the planet) itself at the equator. This is in stark contrast to Earth, which has a subrotating atmosphere, and suggests that superrotation may be the norm rather than the exception.

This thesis explores three elements of tropical planetary atmospheres. First, I use microwave observations of Saturn's atmosphere to determine the gaseous ammonia distribution and hypothesize about what it implies for the tropical circulation (Chapter 2). Unlike on Earth, observations of Saturn's thick atmosphere, especially below the main cloud deck, are scarce and difficult to make. In this chapter I determined the latitudinal distribution of ammonia, a condensable vapor in Saturn's atmosphere, near the 1-bar level. Because ammonia is condensable, it is analogous to water vapor in Earth's atmosphere. When the atmosphere is saturated or very dry (e.g., 100% versus 0% relative humidity), one might be able to infer the direction of vertical mo-

tion in the atmosphere. On Earth, for example, there are dry regions in the subtropics on either side of the equator. This is where Earth's deserts are located. These dry regions coincide with atmospheric downwelling from the Hadley circulation. We view ammonia vapor similarly on Saturn, and speculate on the tropical circulation given the latitudinal distribution of ammonia vapor.

In Chapter 3 I use an atmospheric general circulation model (GCM) to study superrotation in terrestrial atmospheres (i.e., planets with solid surfaces). Superrotation occurs when the angular momentum of the atmosphere exceeds that of the solid-body planet beneath it, or, in the case of the gas giants, relative to the rotation of their cores and magnetic fields. Superrotation is ubiquitous in our solar system, but, as previously mentioned, it is not a phenomenon observed in Earth's troposphere. Earth-like climate models have, however, demonstrated a transition to superrotation under extreme global warming scenarios (e.g., Caballero and Huber 2010). The work done in Chapter 3 helps us to understand under which conditions superrotation arises in terrestrial atmospheres.

Finally, I use a slab ocean idealized GCM to study the fundamental dynamics of a monsoon system over an idealized continent (Chapter 4). Monsoons are seasonal migrations of the intertropical convergence zone, or ITCZ, over subtropical continents. Although monsoons are important features of the summertime tropical circulation on Earth, we still lack a coherent understanding of them. In this work we find that the seasonal progression of the ITCZ, even over a very gross idealization of an Asia continental configuration and in a model with simplified physics, mimics that of the ITCZ in the Indian monsoon sector. Idealized studies like the one in Chapter 4 may provide insights into fundamental dynamical and thermodynamical mechanisms controlling the existence and seasonality of monsoons and provide useful constraints for diagnosing output from comprehensive GCMs, such as those in the CMIP5 archive.

Although the three projects presented in this thesis use different methods and

have different specific motivations, the underlying theme is clear: We want to have a comprehensive understanding of tropical atmospheric dynamics. Both models and observations are essential to this, and I have used both here. Different planets present different challenges and push the limits of our understanding. The contributions of this work bring us closer to achieving this goal.

Chapter 2

Analysis of Saturn's thermal emission at 2.2-cm wavelength: spatial distribution of ammonia vapor

[0]Reprinted from Elsevier. Formal publication located at doi:10.1016/j.icarus.2013.06.017

Icarus 226 (2013) 641–654

Contents lists available at SciVerse ScienceDirect

Icarus

journal homepage: www.elsevier.com/locate/icarus

Analysis of Saturn's thermal emission at 2.2-cm wavelength: Spatial distribution of ammonia vapor

A.L. Laraia [a,*], A.P. Ingersoll [a], M.A. Janssen [b], S. Gulkis [b], F. Oyafuso [b], M. Allison [c]

[a] California Institute of Technology, Pasadena, CA 91125, United States
[b] Jet Propulsion Laboratory, California Institute of Technology, Pasadena, CA 91109, United States
[c] NASA Goddard Institute for Space Studies, New York, NY 10025, United States

ARTICLE INFO

Article history:
Available online 27 June 2013

Keywords:
Saturn, Atmosphere
Atmospheres, Structure
Atmospheres, Composition
Atmospheres, Dynamics
Radio observations

ABSTRACT

This work focuses on determining the latitudinal structure of ammonia vapor in Saturn's cloud layer near 1.5 bars using the brightness temperature maps derived from the Cassini RADAR (Elachi et al. [2004], Space Sci. Rev. 115, 71–110) instrument, which works in a passive mode to measure thermal emission from Saturn at 2.2-cm wavelength. We perform an analysis of five brightness temperature maps that span epochs from 2005 to 2011, which are presented in a companion paper by Janssen et al. (Janssen, M.A., Ingersoll, A.P., Allison, M.D., Gulkis, S., Laraia, A.L., Baines, K., Edgington, S., Anderson, Y., Kelleher, K., Oyafuso, F. [2013]. Icarus, this issue). The brightness temperature maps are representative of the spatial distribution of ammonia vapor, since ammonia gas is the only effective opacity source in Saturn's atmosphere at 2.2-cm wavelength. Relatively high brightness temperatures indicate relatively low ammonia relative humidity (RH), and vice versa. We compare the observed brightness temperatures to brightness temperatures computed using the Juno atmospheric microwave radiative transfer (JAMRT) program which includes both the means to calculate a tropospheric atmosphere model for Saturn and the means to carry out radiative transfer calculations at microwave frequencies. The reference atmosphere to which we compare has a 3× solar deep mixing ratio of ammonia (we use 1.352×10^{-4} for the solar mixing ratio of ammonia vapor relative to H_2; see Atreya [2010]. In: Galileo's Medicean Moons – Their Impact on 400 years of Discovery. Cambridge University Press, pp. 130–140 (Chapter 16)) and is fully saturated above its cloud base. The maps are comprised of residual brightness temperatures—observed brightness temperature minus the model brightness temperature of the saturated atmosphere.

The most prominent feature throughout all five maps is the high brightness temperature of Saturn's subtropical latitudes near ±9° (planetographic). These latitudes bracket the equator, which has some of the lowest brightness temperatures observed on the planet. The observed high brightness temperatures indicate that the atmosphere is sub-saturated, locally, with respect to fully saturated ammonia in the cloud region. Saturn's northern hemisphere storm was also captured in the March 20, 2011 map, and is very bright, reaching brightness temperatures of 166 K compared to 148 K for the saturated atmosphere model. We find that both the subtropical bands and the 2010–2011 northern storm require very low ammonia RH below the ammonia cloud layer, which is located near 1.5 bars in the reference atmosphere, in order to achieve the high brightness temperatures observed. The disturbances in the southern hemisphere between −42° and −47° also require very low ammonia RH at levels below the ammonia cloud base. Aside from these local and regional anomalies, we find that Saturn's atmosphere has on average 70 ± 15% ammonia relative humidity in the cloud region. We present three options to explain the high 2.2-cm brightness temperatures. One is that the dryness, i.e., the low RH, is due to higher than average atmospheric temperatures with constant ammonia mixing ratios. The second is that the bright subtropical bands represent dry zones created by a meridionally overturning circulation, much like the Hadley circulation on Earth. The last is that the drying in both the southern hemisphere storms and 2010–2011 northern storm is an intrinsic property of convection in giant planet atmospheres. Some combination of the latter two options is argued as the likely explanation.

1. Introduction

The instruments on board the Cassini orbiter have provided the giant planets community with a plethora of data on Saturn's

* Corresponding author.
E-mail address: alaraia@caltech.edu (A.L. Laraia).

0019-1035/$ - see front matter © 2013 Elsevier Inc. All rights reserved.
http://dx.doi.org/10.1016/j.icarus.2013.06.017

atmosphere for the past decade. Ideally, we would like to get a comprehensive picture of Saturn's atmosphere that reconciles the general circulation, the cloud and haze distributions and compositions, the zonal wind profile, and the storm locations and dynamics. One major observational roadblock is that the stratospheric and upper tropospheric clouds and hazes on Saturn block our view of the atmosphere beneath them.

The location and magnitude of the zonal jets at the cloud tops are well known from Voyager measurements (Sánchez-Lavega et al., 2000). The broad, strongly superrotating jet centered on the equator is a distinctive feature, with alternating eastward and westward jets to either side of the equator. Unlike Jupiter, convection on Saturn appears in both westward and eastward jets (Del Genio et al., 2009). Convective events on Saturn are intermittent, and the cause of the intermittency is uncertain. Saturn electrostatic discharges, or SEDs (Kaiser et al., 1983; Porco et al., 2005; Fischer et al., 2006, 2007), have been observed in convective storms and are indicative of lightning at depth. What causes these convective outbursts on Saturn, and how do they contribute to or maintain the general circulation? How does deep convection work on Saturn, and how does it fit together with the latitudinal belt-zone structure of the giant planets? Answers to these questions have been difficult to obtain. The 2.2-cm observations analyzed in this work provide new data on the distribution of ammonia vapor in and beneath the ammonia clouds, and will help diagnose the atmospheric dynamics at work inside the convective storms.

The structure of Saturn's clouds and hazes is still being studied, although the general features are understood. The equatorial zone is a region of constant high clouds and thick haze, whereas the midlatitudes (generally between ±20° and ±60°) are regions of smaller, more variable clouds (West et al., 2009). The vertical structure and composition of these clouds and hazes is not well known, but Cassini observations made by the ISS (imaging science subsystem), VIMS (Visual and Infrared Mapping Spectrometer) and CIRS (Composite Infrared Spectrometer) instruments are closing our knowledge gaps in these areas. Tied to the distribution of clouds and hazes is the distribution of tropospheric gases, for example ammonia and phosphine. How does the latitudinal distribution of clouds, hazes, and tropospheric gases coincide with Saturn's belt-zone structure? Knowing the spatial distribution of these gases can help us determine the dynamical mechanisms that produce the spatial patterns themselves. For example, vertical motion, caused by either convection or large-scale meridional overturning, plays a key role in determining where clouds and hazes will or will not form.

This work focuses on determining the latitudinal structure of ammonia vapor in Saturn's ammonia cloud layer using the brightness temperature maps derived from the Cassini RADAR (Elachi et al., 2004) instrument, which works in a passive mode to measure thermal emission from Saturn at 2.2-cm wavelength. These maps are presented in a companion paper by Janssen et al. (2013, this issue), hereafter referred to as J13. The maps provide data on the spatial distribution of ammonia vapor in the pressure range 1–2 bars, in the vicinity of the ammonia ice cloud. We believe these maps provide information about Saturn's meridional circulation. The 2.2-cm data have better spatial resolution and sensitivity than any other microwave data on Saturn. The calibration of Cassini's RADAR instrument, described in detail in Janssen et al. (2009) and J13, is accurate and was validated using both Saturn and more recent Titan observations as described in J13.

Section 2 describes the 2.2-cm observations and the radiative transfer model used in our analysis. The brightness temperature maps are described in Section 3. Section 4 compares the observations to the output from the radiative transfer model. Discussion and implications for Saturn's atmospheric dynamics are given in Section 5, and conclusions are given in Section 6.

2. Observations and radiative transfer model

Cassini's RADAR radiometer was used to map Saturn during five equatorial periapsis passes occurring between 2005 and 2011. The maps were formed from continuous pole-to-pole scans taken through Saturn nadir during the periapsis passes, allowing the rotation of Saturn to sweep the scan westward in longitude. The observations and mapping are described in detail in J13 along with the calibration and error analysis. We refer the reader to Section 2 of J13 for a description of the observations and observational approach, and to Section 3.2 of J13 for a description of the map-generating process.

The reference model used to calculate the residual brightness temperature maps is also described in detail in Section 3.1 of J13. The model and radiative transfer calculations were made using the Juno atmospheric microwave radiative transfer (JAMRT, Janssen et al., 2005, in preparation) program, which is in development for the Juno Microwave Radiometer (MWR) experiment on Jupiter. To match the RADAR observations, radiative transfer calculations are carried out at 2.2-cm wavelength (13.78 GHz), and brightness temperatures are output for each observation. This model builds an atmosphere with user-prescribed physical parameters, such as the vertical mixing ratio profiles of ammonia, phosphine and water. Temperature and pressure profiles are calculated assuming hydrostatic equilibrium using both wet and dry adiabats. The reference model assumes a moist adiabatic temperature profile with 100% relative humidity (RH), with a dry adiabatic profile below cloud base, such that the temperature is monotonically decreasing from the bottom to the top layer of the model atmosphere. The adiabats include the contributions from the NH_4SH and H_2O clouds, although the weighting function drops to essentially zero before we reach the water cloud at great depth. A temperature of 134.8 K (Lindal et al., 1985) is specified at a pressure of 1 bar, and the model temperature profile is slaved to this reference value. We varied this value in order to test the sensitivity of the 2.2-cm brightness temperature to variations in the 1-bar temperature, and found the brightness temperature to be only minimally sensitive to this reference value (see Section 5.1). The topmost level of the model is the level at which the temperature reaches 110 K, which is 560 mb for the (134.8 K, 1 bar) reference point. The model assumes a completely transparent atmosphere above 110 K and therefore ignores this region of the atmosphere. The deepest level of the model atmosphere is 1000 bars, which is well below the pressure level sensed by the 2.2-cm observations, and the vertical layers are 100 m thick. The model also includes the emission angle dependence (limb darkening) of the brightness temperature.

Table 1 gives the atmospheric constituents and their respective abundances in the model atmosphere, including the values used for the solar abundances. H_2O, NH_3, PH_3, and H_2S are the condensable gases (Atreya, 2010). H_2S reacts with NH_3 to form an NH_4SH cloud with a base around 5 bars. An ammonia ice cloud forms above this, with a base around 1.5 bars. The water cloud is deeper (base ~10 bars) and out of the sensitivity range of the 2.2-cm

Table 1
Abundances of atmospheric constituents in the JAMRT program. Solar and enrichment values are from Atreya (2010), who calculated solar abundances from the photospheric values of Grevesse et al. (2005).

Constituent	Solar abundance (relative to H_2)	Enrichment relative to solar
He	0.195	0.6955
CH_4	5.50×10^{-4}	9.4
H_2O	1.026×10^{-3}	3.0
NH_3	1.352×10^{-4}	3.0
H_2S	3.10×10^{-5}	5.0
Ar	7.24×10^{-6}	1.0
PH_3	5.14×10^{-7}	7.5

weighting function. In the model, the presence of the ammonia ice cloud particles does not affect the 2.2-cm brightness temperature significantly, although the depletion of ammonia vapor by the formation of the clouds does. Using Cassini Visible and Infrared Imaging Spectrometer (VIMS) data, Fletcher et al. (2011a) find evidence of a compact cloud deck in the 2.5–2.8 bar region. They point out that this is "deeper than the predicted condensation altitudes for pure NH_3 clouds (1.47–1.81 bars) and higher than the predicted condensation altitudes for the NH_4SH cloud (4.56–5.72 bars)." They conclude, "The VIMS 2.5–2.8 cloud cannot be identified unambiguously using the present data set." Resolving this discrepancy is beyond the scope of this paper, so we use an equilibrium condensation model similar to that referred by Fletcher et al. (2011a), even though it does not entirely fit their interpretation of the VIMS data. For a more in-depth description of the JAMRT program, see Section 3.1 of J13.

Because we only have data at one wavelength, there arises the unavoidable ambiguity of whether temperature or ammonia is the cause of the variations in brightness temperature. Our analysis assumes that atmospheric temperature is constant with latitude in the sensitivity range of 1–2 bars, and that variations in the ammonia mixing ratio cause brightness temperature variations. From a data-fitting point of view, one could also perform this analysis assuming that the mixing ratio of ammonia is constant with latitude and that atmospheric temperature fluctuations cause brightness temperature variations. In general, brightness variations can be due to both fluctuations in ammonia concentration and atmospheric temperature from latitude to latitude, and these are not easily separated. We think that ammonia dominating the brightness temperature variations at 2-cm wavelength is the right choice, based on both the fact that emission from ammonia within the cloud region is strongly buffered against temperature variations, and also the extreme sensitivity of condensation/evaporation to vertical motions, as exhibited in the Earth's tropics. Large-scale subsidence, for example, will cause a "drying" of the atmosphere at certain latitudes, and could potentially produce a thermal emission pattern like the one we observe on Saturn. Our interpretation of the brightness temperature variations as variations in ammonia abundance is consistent with Grossman et al. (1989), who analyzed thermal emission from Saturn at 2- and 6-cm wavelength. They argue that large temperature deviations (on the order of 8 K in their paper) would be difficult to sustain in the presence of convection.

There are two basic ways to increase the brightness temperature Tb. Either increase the atmospheric temperature T with constant ammonia mixing ratio, or else hold T constant and lower the ammonia mixing ratio. In both cases the relative humidity (RH) goes down. If RH stays constant, an increase (decrease) in temperature is offset by an increase (decrease) in ammonia abundance due to the Clausius–Clapeyron relation, and the brightness temperature stays the same. Thus Tb is measuring RH in the sense that high RH gives low Tb and vice versa. When we refer to "drying out" of the atmosphere, we are referring to low RH acting to produce high Tb.

We varied two parameters of the model to produce departures from the reference model: the enrichment factor of ammonia relative to the solar abundance (EF), and the ammonia depletion factor (DF). The enrichment factor EF is defined as the deep mixing ratio of ammonia vapor, expressed in terms of the solar abundance of ammonia (Table 1). In the model ammonia is uniformly mixed below the level where it reacts with H_2S to form an ammonium hydrosulfide cloud. It is partially depleted from that level up to the ammonia condensation level, where the mixing ratio of ammonia falls off according to the saturation vapor pressure dependence on temperature (the Clausius–Clapeyron relation). The deep abundance of ammonia is not precisely known on Saturn, but is thought to be in the range 2–4× solar (Atreya, 2010). We vary EF from 2 to 8 in this work (corresponding to volume mixing ratios of 2.3–9.4×10^{-4}). This range encompasses previous estimates for the deep abundance of gaseous ammonia, for example $4–6 \times 10^{-4}$ reported by Briggs and Sackett (1989) and 5×10^{-4} reported by de Pater and Massie (1985) from VLA measurements.

The depletion factor DF_X is chosen to allow an additional depletion of ammonia above some level X. Beginning with an ammonia mixing ratio distribution determined for an atmosphere with a given EF, DF_X is simply a scale factor between 0 and 1 that multiplies the vertical distribution of ammonia above level X. It is intended purely as a first-order parameter to investigate ammonia depletions likely to occur in more realistic dynamical atmospheres. In applying DF_X we ignore any perturbations implied for other components of the model atmosphere such as the cloud base height or the temperature profile. For example, in the cloud layer, DF_{cb} would correspond to the relative humidity (RH) of ammonia, where we choose the cloud base as our level X. In the following we choose DF_{cb} and a second choice DF_{5bar}, with level X as the 5-bar pressure level, to effectively bracket the cases we will study for ammonia depletion. We will show that both parameters are needed to explain the observed 2-cm brightness temperatures.

Figs. 1–3 demonstrate the effects of varying EF and DF in the model atmosphere. Fig. 1 shows two ammonia profiles, given by the heavy solid (EF = 8) and dashed (EF = 3) lines, both with DF = 1 (at all altitudes). The ammonia mixing ratios are less than 3 and 8× solar at the 2.5-bar limit of Fig. 1 because the NH_4SH cloud has a base around 5 bars and depletes the ammonia above. The light solid and dashed lines are the weighting functions that correspond to the 8× solar and 3× solar ammonia profiles, respectively. The weighting function for 3× solar extends deeper because there is less ammonia at the 1.5–1.8 bar level to block the radiation from below. The dotted curves are the temperature profiles for the two atmospheres, which differ only very slightly at the 2.5 bar level (with the 3× solar case being slightly warmer than the 8× solar case). The calculated brightness temperatures for these two models are 148.0 K for 3× solar and 147.9 K for 8× solar ammonia. Increasing EF further has very little effect on the brightness temperature.

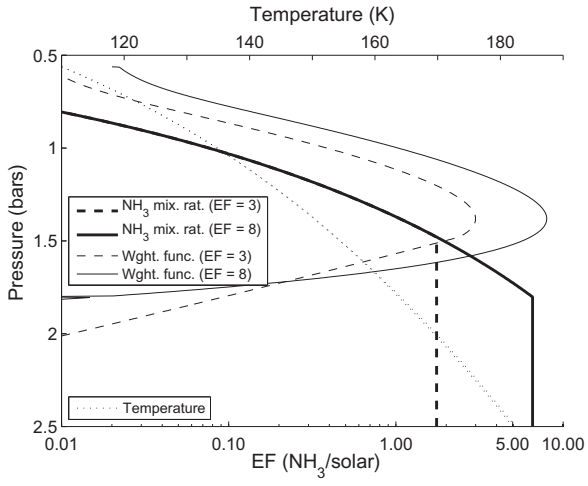

Fig. 1. Two vertical profiles of ammonia vapor with varying EF (bold lines). The solid and dashed bold lines are profiles with EF = 8 and 3, respectively, and the solid and dashed lines are their respective weighting functions. Their temperature profiles (top x-axis) are given by the dotted lines, which are almost identical in this pressure range, except that the 3× solar case is slightly warmer than the 8× solar case at 2.5 bars. The model brightness temperatures for the 3 and 8× solar cases are 148.0 K and 147.9 K, respectively.

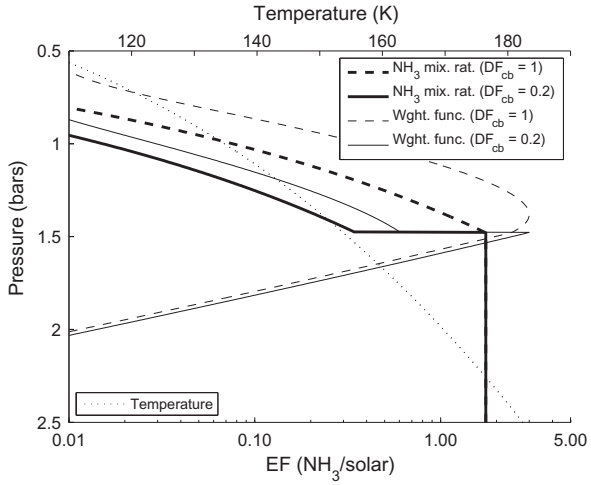

Fig. 2. Same as Fig. 1, but for constant EF = 3 and varying DF_{cb} (or ammonia RH in the cloud layer). In this case the two model atmospheres have the same temperature profile. The case with $DF_{cb} = 1$ is identical to the EF = 3 case in Fig. 1 (bold dashed line). There is a discontinuity in the ammonia mixing ratio at the cloud base for $DF_{cb} = 0.2$ (bold solid line) due to the way the DF parameter functions in the model. The model brightness temperatures are 148.0 K and 154.0 K for the $DF_{cb} = 1$ and 0.2, respectively.

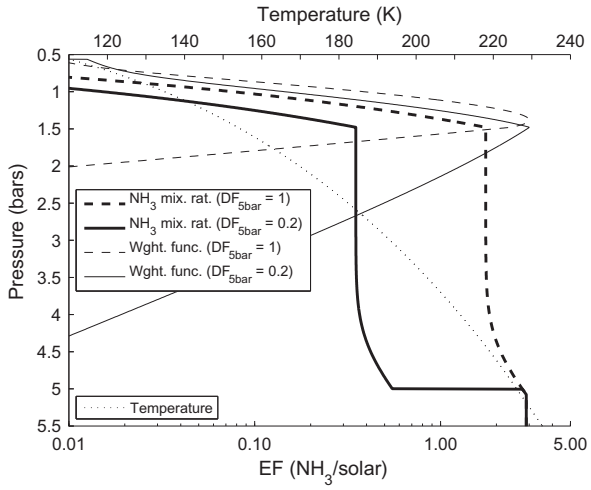

Fig. 3. Same as Figs. 1 and 2, but for constant EF = 3 and varying DF_{5bar}. Again, the $DF_{5bar} = 1$ case is the same as EF = 3 in Fig. 1 and $DF_{cb} = 1$ in Fig. 2. Note the change in scale of the *y*-axis. Like Fig. 2, there is a discontinuity in the ammonia mixing ratio at the level at which DF is applied (bold solid line), which is 5 bars for this case. The ammonia continues to be depleted between 4 and 5 bars because the formation of the NH_4SH cloud at 5 bars causes ammonia depletion there. The model brightness temperatures are 148.0 K and 161.2 K for $DF_{5bar} = 1$ and 0.2, respectively.

Fig. 2 is like Fig. 1 but with EF = 3 held constant and DF_{cb} varied. The heavy solid and dashed lines are for atmospheric profiles of $DF_{cb} = 0.2$ (RH = 20%) and 1 (RH = 100%), respectively. The dotted line is the temperature profile of both atmospheres. The calculated brightness temperatures for $DF_{cb} = 1$ and 0.2 are 148.0 K and 154.0 K respectively.

Fig. 3 is like Fig. 2, except DF_{5bar} is varied. Note the difference in scale of the *y*-axis between Fig. 3 and the previous two figures. In addition to the imposed depletion above the 5 bar level, the NH_4SH cloud also depletes ammonia above the 5 bar level, which is why there is still some ammonia depletion above 5 bars for $DF_{5bar} = 1$. The calculated brightness temperatures for $DF_{5bar} = 1$ and 0.2 are 148.0 K and 161.2 K, respectively.

The explanation for the differing brightness temperatures in each model atmosphere is as follows: If there is relatively less ammonia in a given atmospheric column (from the top down), then the 2.2-cm weighting function will have contributions from higher pressures. Because the model temperature falls off adiabatically with height at all levels, the 2.2-cm brightness temperature will be higher when there is less ammonia in the column, since we are probing a lower altitude in the atmosphere where the temperature is warmer. The opposite is true if there is relatively more ammonia in the column; namely, the resulting brightness temperature will be lower.

We chose to vary DF down to a level of 5 bars, which sparks the question: how deep is it necessary to deplete ammonia in order to achieve the observed brightness temperatures? Fig. 4 helps answer this question by displaying DF_X as a function of X, where X is the pressure level to which we deplete ammonia (EF = 3 for all of these calculations). Except for the smallest values of DF_X, the curves are flat for $X > 2$ bars. Depleting down to 5 bars is equivalent to depleting down to 2 bars, which means that the 2.2-cm weighting function is very small below 2 bars in this parameter regime (EF = 3, $0.1 \leqslant DF_X \leqslant 1$), and the brightness temperature is not very sensitive to depletion below the 2 bar level. For values of DF_X less than 0.1, the brightness temperature is very sensitive to the depth of depletion because the weighting function peaks at X bars for small DF_X. A similar plot was made for EF = 6, and the difference was that the brightness temperature of the 6× solar case was less than the 3× solar case by 1–7 K depending on the value of DF_X. The lower brightness temperatures for EF = 6 are to be expected because when EF is larger, there is less emission from the deeper levels and the upper levels must be depleted a little more to get the same brightness temperature.

3. Maps

After using the radiative transfer model to calculate the brightness temperature as a function of emission angle, the residual brightness temperatures were calculated relative to a saturated atmosphere (RH = 100% above the condensation level)

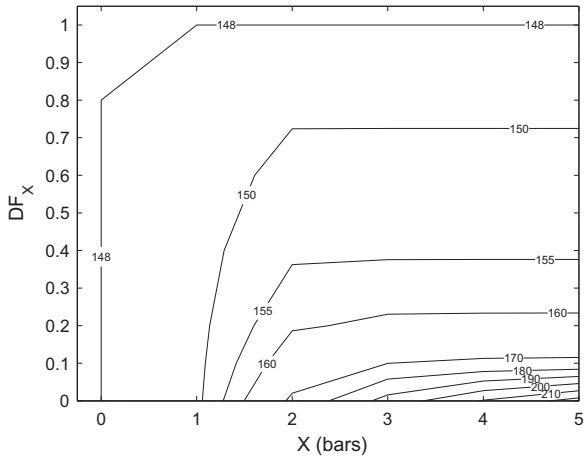

Fig. 4. Contours of model brightness temperature (in Kelvin) as a function of the depletion factor DF_X and X (the depth of depletion) for constant enrichment factor of ammonia relative to the solar abundance EF = 3. DF_X is a scalar parameter between 0 and 1 that multiplies the vertical distribution of ammonia above some pressure level X. Thus, $DF_X = 1$ is no depletion and $DF_X = 0$ is 100% depletion of ammonia vapor above level X.

model with the constituent enrichments given in Table 1. All future mention of residual brightness temperatures refers to the residuals from this 3× solar ammonia reference model, which was chosen based on the ability of the EF = 3 reference model to span the observed brightness temperatures better than the models with higher or lower values of EF (Section 4, Figs. 11 and 12). Fig. 5 is a map from December 9, 2009 of the 2.2-cm residual brightness temperature, created by the procedure explained in Section 3.2 of J13. There are four other maps analyzed in this work but not shown here: September 23, 2005, October 13, 2009, July 25, 2010 and March 20, 2011. They are presented in Fig. 9 of J13.

3.1. Obstruction by the rings

An issue persistent throughout all the maps is that the equator is obstructed by the rings (black region along equator in Fig. 5). The rings are optically thick scatterers with very little intrinsic thermal emission, and hence lower the measured brightness temperature in the northern (southern) hemisphere when the spacecraft is below (above) the ring plane. When the spacecraft is in the ring plane, the ring inclination angle is exactly 0° and the rings disappear from view, allowing full view of the equator. Fig. 6 demonstrates the effect of the ring obstruction on brightness temperature for the July 2010 map, the map for which the effect of the rings is most prominent (see Fig. 9 of J13). Each line is a different meridional (pole-to-pole) scan near the spacecraft's ring plane crossing (RPC), labeled with the ring inclination angle. For an example of a RPC scan see Fig. 5 near longitude 18°W, where the ring blockage at the equator goes to zero. During the July 2010 observation period, Cassini was moving rapidly across the ring plane. Thus the effect of the rings on the brightness temperature is large, 50% between two scans taken only minutes apart (e.g. from scan −0.019° to −0.377°). Fig. 6 demonstrates that ring inclination angles as small as 0.1° have large effects on the observed equatorial brightness temperature.

Cassini crossed the ring plane in four of the five maps. We test our ability to remove the ring effect with a model that assumes an isothermal (150 K) brightness temperature for the atmosphere and a ring brightness temperature of 25 K. With this model we synthesize the individual brightness scans taking into account the actual geometry of the spacecraft and the instrument. The right panel of Fig. 7 shows the results from this model for the four scans

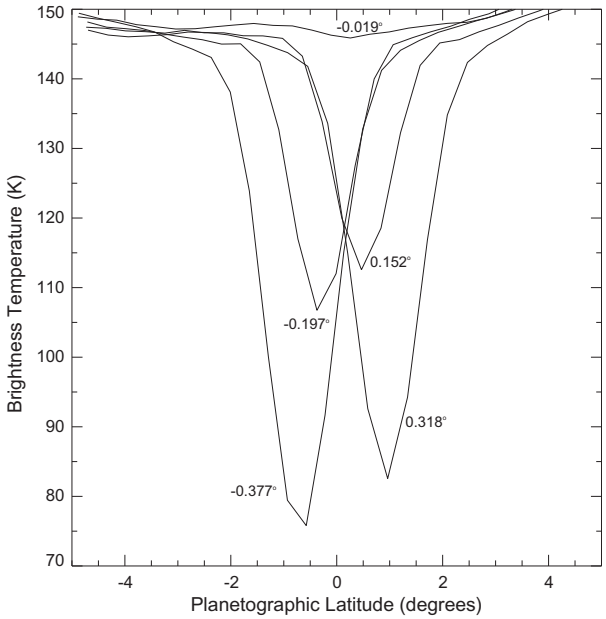

Fig. 6. Five individual scans around ring plane crossing (RPC) for the July 2010 map. Scans are labeled with their ring inclination angles as viewed by Cassini. The first scan, labeled 0.318°, was made while the spacecraft was in the southern hemisphere, therefore the ring blockage occurred in the northern hemisphere. As Cassini approached the ring plane, the effect of the rings became quite small. Because the spacecraft was moving fairly quickly across the ring plane in this map, the rings had a very large effect from one scan to the next.

closest to RPC for the December 2009 map, which has the smallest ring inclination angle while observing the equator. The labels are the same as in Fig. 6, but the scales along the *y*-axis are different. The left panel shows the observed brightness temperatures for the same scans. The model does not predict any dip in brightness temperature at the equator for the RPC scan (0.001° ring inclination angle), demonstrating that we are observing the true equatorial brightness temperature in this scan. In the left panel, the 0.001° scan is continuously flat through the equator (within ±2°), which does not occur for any other RPC scan except for the

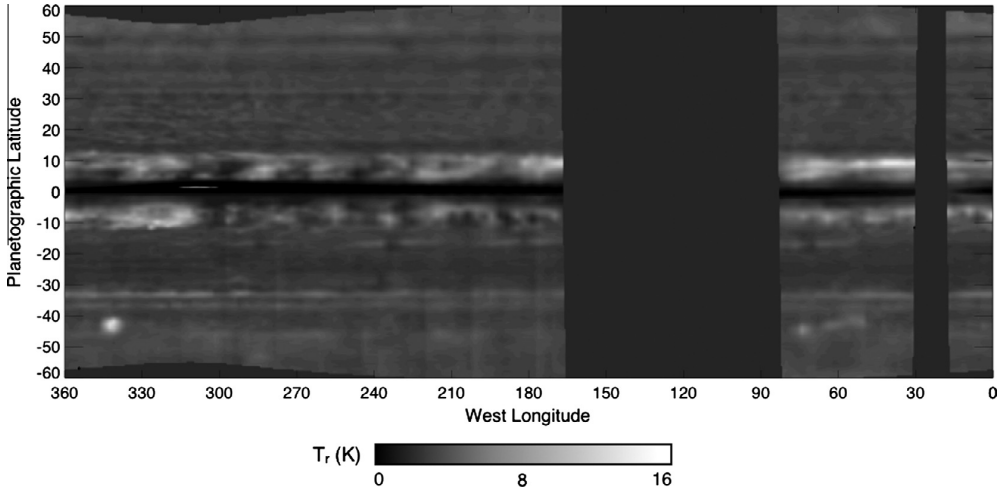

Fig. 5. 2.2-cm residual brightness temperature (in Kelvin) map of Saturn from December 9, 2009. The residual temperature is calculated by subtracting the brightness temperature from a fully-saturated reference model with 3× solar ammonia mixing ratio (Section 2) from the observed brightness temperature. The black band at the equator is due to the cold rings obstructing the atmosphere. Section 3.2 of J13 offers a detailed explanation of how the brightness temperature maps were generated.

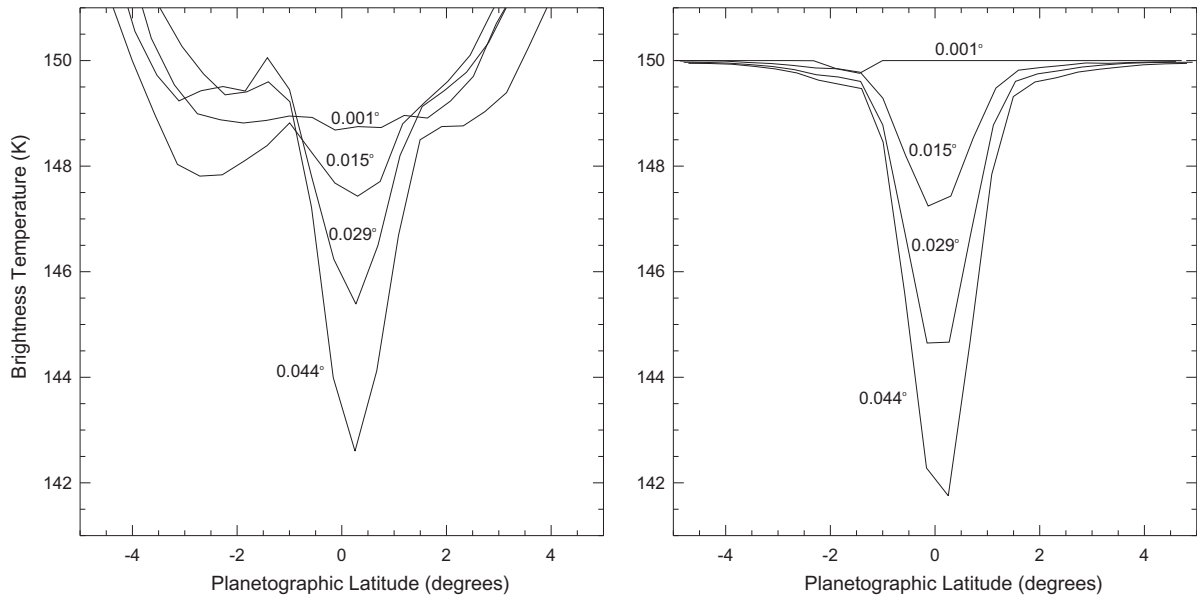

Fig. 7. Left panel: Same as Fig. 6 for the December 2009 map. The RPC scan for this map has the smallest ring inclination angle of all the maps (while viewing the equator), and is flat across the equator. This is the best view of the equatorial brightness temperature that we have of all five maps. Right panel: Same labeling, but for a simple beam convolution model that takes into account the Cassini–Saturn geometry and includes the A and B rings only. It assumes an isothermal atmosphere of 150 K, and takes the microwave brightness of both the A and B rings to be 25 K. According to this model, we actually see the equator with no ring blockage for the 0.001° scan.

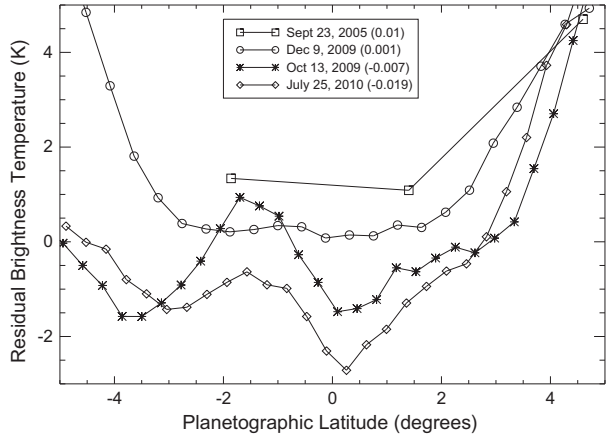

Fig. 8. Residual brightness temperatures for RPC scans of the four maps and their average. The ring inclination angle for each scan is in parentheses next to the date. Because of the low resolution of the September 2005 scan, the bright bands off the equator affect the equatorial brightness temperature, causing it to be 0.7 K too high. With this in mind, the four scans are within ±1.5 K. The December 2009 RPC scan is flat across the equator with a very small ring inclination angle. Thus it provides the true equatorial brightness temperature.

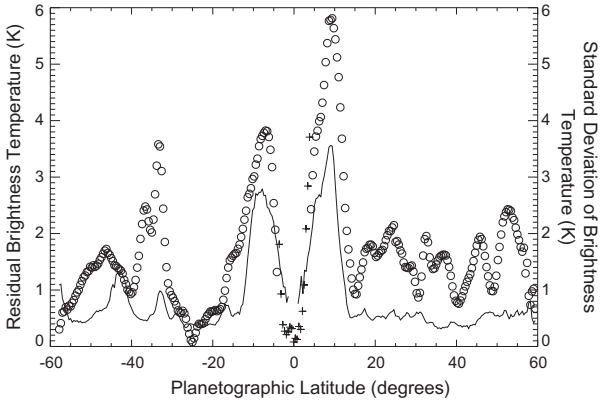

Fig. 9. Mean residual brightness temperature (open circle and + signs) and its mean standard deviation as a function of planetographic latitude (solid line) for all five maps, excluding the northern storm and the latitudes near the equator where the rings block the view of the atmosphere. Observations were sorted into latitude bins 0.4° wide since the latitudes are unevenly spaced. From −4° to +4° the single December 2009 RPC scan is used (+ signs), because it is the best view of the equatorial brightness temperature that we have of all the maps (Section 3.1). Standard deviations were calculated at each latitude for each map and then averaged. The average is weighted by the number of observations at a given latitude and date and the sum is over all five observation dates.

September 2005 scan, which is at very low resolution compared with the other three maps (Fig. 8). Thus we take the December RPC scan as the RPC scan that provides the true equatorial brightness temperature. The increase in brightness temperature at latitudes greater than 3° in both hemispheres is not in the model but is a real property of Saturn's atmosphere.

Fig. 8 displays residual brightness temperatures versus latitude for all four RPC scans. The scale along the *y*-axis is expanded relative to that in Figs. 6 and 7. The ring inclination angles for each scan are displayed in parentheses in the legend. The segment of the September 2005 map where the RPC occurred is at very low resolution (Fig. 9, J13), and is therefore affected by the two bright bands at ±9° with a contribution of about +0.7 K. Applying this correction to the September 2005 scan brings the residual brightness temperature down to 0.5 K at the equator. The observed residuals are consistent with ∼1 K variability in the equatorial region. We chose the December 2009 RPC scan to represent the equatorial brightness temperature for all five maps in Fig. 9 because it has the best geometry (lowest inclination at RPC) and produces the best picture of the equatorial brightness temperature that we have.

3.2. General features

With the exception of the March 2011 map, which has the 2010–2011 northern storm (Figs. 9 and 12, J13) or great white spot (Fischer et al., 2011; Sánchez-Lavega et al., 2011), all of the maps share the same general characteristics. In what follows, all latitudes are planetographic unless explicitly stated. In Fig. 5, the equatorial region, within 10° of the equator, is texturally anomalous compared with the rest of the map, even when excluding the effect of the rings. There is non-uniform high brightness near −9° and 9° that generally decreases towards the equator, which is obstructed by the rings for all scans except for the one during RPC. The brightness temperature variations on the maps are quite large, with variations of more than 10 K, and we investigate the causes of these variations. There are some structures in the southern hemisphere band between −42° and −47° (e.g. at 340°W and 75°W in Fig. 5), which is just south of the westward jet at −42° (−35° planetocentric) and has been the site of many lightning observations (Dyudina et al., 2007; Fischer et al., 2011). There are also two narrow bright bands at −33° and −37°, and a broad dark band from −15° to −30°.

The highest brightness temperature in the northern storm is 165.7 K (18.9 K residual brightness temperature). The highest brightness temperature in all five maps is 167.1 K (19.3 K residual brightness temperature), which occurs in the subtropical latitudes in the October 2009 map.

Fig. 9 shows the zonally averaged residual brightness temperature (open circles and + signs) and its standard deviation (solid line) as a function of latitude. Outside of ±4° latitude, the brightness temperatures are averaged over longitude and over all five maps (open circles), excluding the 2010–2011 northern storm and the latitudes near the equator where the rings block the view of the atmosphere. Within ±4° of the equator, a single RPC scan from the December 2009 map is used (+ symbols), as explained in Section 3.1. The standard deviation was computed with respect to longitude for each latitude outside ±4°, and then the weighted standard deviation for all five maps was calculated. The weights used in this calculation are the number of observations at a given latitude and date and the sum is over all five observation dates. The globally averaged residual brightness temperature from Fig. 9 is 1.7 ± 1.1 K, where the 1.1 K is real variability of the longitudinally-averaged brightnesses in Saturn's atmosphere.

The residual brightness temperatures shown in Fig. 9 are positive at every latitude. One important implication of this observation is that the atmosphere is always ammonia-depleted with respect to a fully-saturated 3× solar ammonia model (Table 1). A striking feature of Fig. 9 is the two relatively bright bands near ±9°, the subtropics of Saturn, with residuals of 3.8 K and 5.8 K in the southern and northern hemispheres, respectively (corresponding to brightness temperatures of 151.7 K and 153.7 K). These two bright latitudes surround a relatively low residual brightness temperature of 0.1 K (corresponding to a brightness temperature of 148.1 K) at the equator. At the equator the atmosphere is close to being saturated with ammonia. The subtropical bands are accompanied by elevated standard deviation, indicating that there is some structure in these regions. Another feature is the pair of bright bands around −36° and −34° with averaged residuals of 2.5 and 3.6 K respectively (corresponding to brightness temperatures of 149.2 and 150.5 K), which correspond to the two narrow bands in the southern hemisphere in Fig. 5. There are two regions with high standard deviation in the southern hemisphere, one near −33° (−28° planetocentric) and the other near −43° (−37° planetocentric). The latter is the latitude of storm alley and the site of the southern hemisphere lightning (Dyudina et al., 2007). The relatively high standard deviation in storm alley corresponds to the bright dots seen there (Fig. 5, longitude 345°W), which are likely to be holes in the ammonia layer associated with the holes in the clouds described by Dyudina et al. (2007). Dyudina et al. (in preparation) investigates the structure of these southern hemisphere storms and presents the lightning observations from both the southern storms and the 2010–2011 northern storm. The northern latitudes have relatively constant brightness temperatures, with fluctuations on the order of 1 K from latitude to latitude. The southern hemisphere has larger brightness temperature gradients than the northern hemisphere, for example almost a 4 K increase from −25° to −35°. For the northern storm (not included in Fig. 9), the standard deviation in the latitude band between 20° and 50° is much larger, reaching a peak value of 6 K at 40°.

When looking at the relatively bright spots within the bright subtropical bands in all five maps, it is natural to ask if there is any periodic structure in these regions. Jupiter, for example, had the equatorial plumes in the northern hemisphere with longitudinal wavenumber between 11 and 13 at the time of the Voyager encounters (Allison, 1990), and between 8 and 12 determined more recently (Arregi et al., 2006). To determine whether there is periodic structure in the subtropical bands of Saturn, we calculated the autocorrelation of the brightness temperature with respect to longitude for latitude bands between 6° and 10° in both hemispheres. We used binning to remedy the problems that arise due to unevenly spaced observation points and large gaps in the maps. For a given latitude, every pair of points was placed into a bin 3° wide based on the lag between the points. Thus the 0° lag bin has pairs of points with lags from 0° to 3°. The next bin is 3–6°, and so on. We did this for four maps, excluding the July 2010 map because the rings obstruct the majority of the subtropical bands. The resulting averaged correlation coefficients are plotted versus longitudinal lag in Fig. 10. The correlations in the southern hemisphere tend to fall off more rapidly than in the northern hemisphere, with the exception of the December 2009 map. This indicates that the bright spots in the northern hemisphere subtropical band have a greater longitudinal span than those in the southern hemisphere. Four of the eight panels in Fig. 10 reveal wave-like features with longitudinal periods ranging from 20° to 45° (zonal wavenumbers 18–8, respectively) for the 6−10° latitude range. The period varies from year to year, and there is no indication of a recurring dominant period. We did not find any wave-like features in other latitude ranges.

4. Comparison with radiative transfer model

Ammonia vapor is the only effective source of opacity in Saturn's atmosphere at 2.2-cm wavelength, as shown by Fig. 3 of J13 that plots absorption coefficient versus height for the relevant constituents. Ammonia is by far the dominant absorber in our sensitivity range. Thus the 2.2-cm brightness temperature maps yield information about the ammonia vapor distribution. To interpret the maps we used the JAMRT program described in Section 2 to calculate 2.2-cm brightness temperatures based on different vertical profiles of ammonia. We varied two parameters, EF and DF, also described in Section 2.

Figs. 1 and 2 suggest that we cannot get brightness temperature variations larger than 11 K by varying only EF (ammonia deep abundance) or DF_{cb} (ammonia RH in the cloud layer), since these two parameters only account for brightness temperature variations of up to 11 K. Fig. 11 demonstrates this by displaying the model brightness temperature (in Kelvin) as a function of DF_{cb} (or RH) and EF. All the calculations done in Figs. 11 and 12 were done at an emission angle of 0°. This is important to note because the model brightness temperatures decrease with increasing emission angle due to limb darkening. For example, a brightness temperature of 160 K at the equator would have a residual of 12 K, while a brightness temperature of 160 K at 40° (e.g., the 2010–2011 northern storm) would have a residual of 13.5 K.

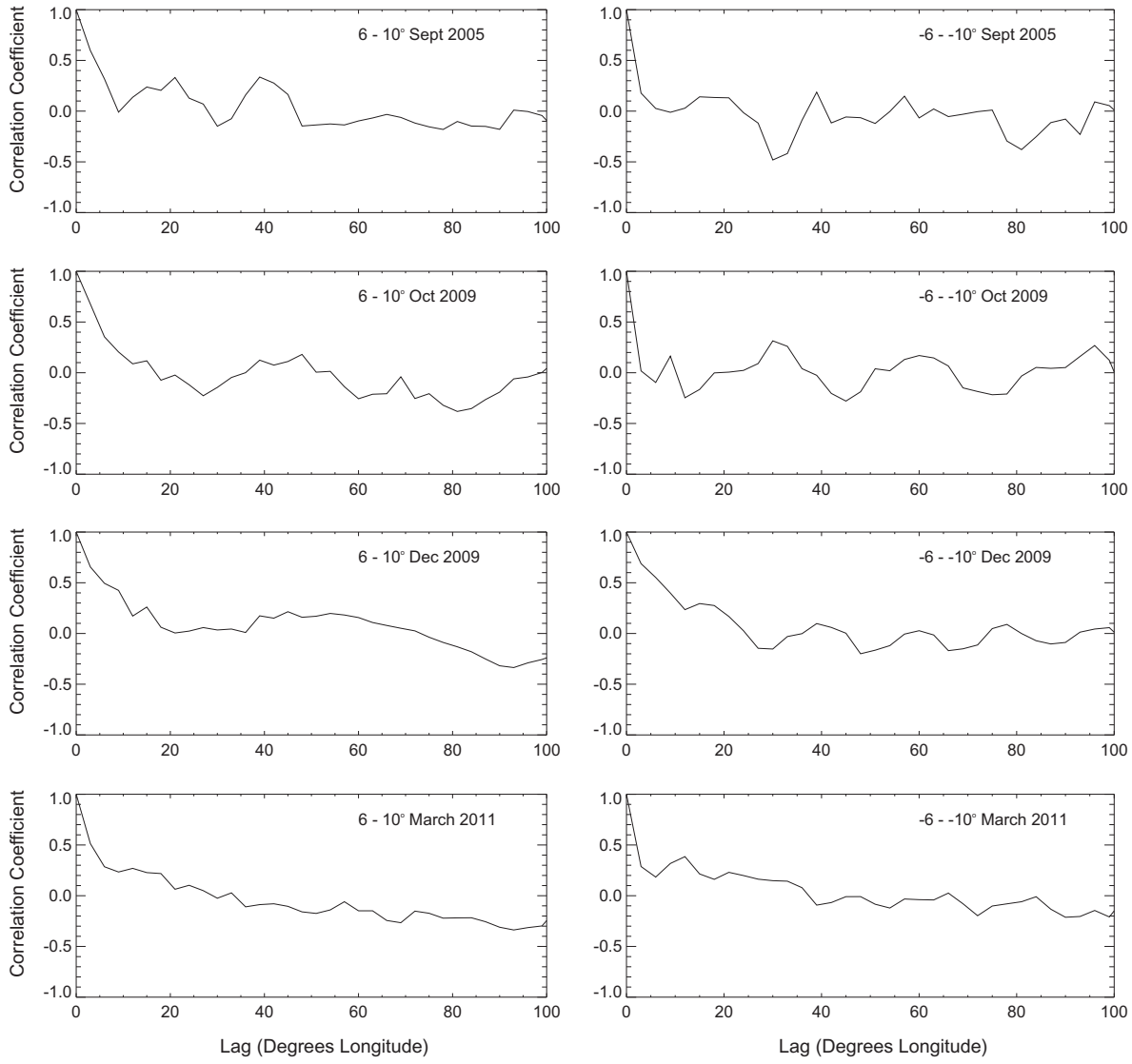

Fig. 10. Autocorrelations of brightness temperature with respect to longitude versus longitudinal lag. The panels display averages of the autocorrelations in the latitude bands from 6° to 10° in the northern hemisphere (left column) and the southern hemisphere (right column) for each map, excluding the July 2010 map due to the large amount of ring blockage in the subtropics.

In Fig. 11, as expected, the brightness temperatures increase with decreasing DF_{cb} (decreasing RH), since depletion of ammonia pushes the weighting function deeper into the atmosphere where it is warmer. However, as mentioned above, the largest temperature contrast that can be obtained in this parameter regime is 11 K (148–159 K, Fig. 11), which indicates that ammonia vapor must be depleted to levels deeper than the ammonia cloud in order to achieve the highest brightness temperatures seen in the maps (160+ K), provided that $DF_{cb} > 0.1$. If $DF_{cb} < 0.1$, then the ammonia concentration in the cloud region is almost zero, which is unlikely given ammonia concentrations reported by Fletcher et al. (2011a) for the 1–4 bar region. The idea that the formation of the NH_4SH cloud around 5 bars is the ammonia-depletion mechanism beneath the ammonia-ice cloud has been discussed by previous authors (e.g. Briggs and Sackett, 1989). Since our model includes the formation of this cloud (with H_2S enriched by 5× solar, Table 1), ammonia must be depleted even more than just by the NH_4SH cloud formation in order to agree with observations, unless H_2S is in reality enriched by more than 5× solar on Saturn.

There is a trend of increasing brightness with increasing EF at low DF_{cb} in Fig. 11. This is counter-intuitive, because increasing EF means more ammonia, but it is an artifact of the model and has an explanation. The DF_{cb} parameter depletes ammonia down to the ammonia cloud base, and for very low DF_{cb} that is where the weighting function peaks. As EF increases, the ammonia cloud base moves to deeper (and warmer) levels (Fig. 1), bringing the weighting function with it. The effect of lowering the altitude of the weighting function outweighs the effect of adding ammonia at deeper levels, and brightness temperature increases with increasing EF.

Fig. 12 is the same as Fig. 11, but for DF_{5bar}. Note that the contour interval has been increased from 1 to 4 K. As expected, the brightness temperature increases with decreasing DF_{5bar} and decreasing EF. By depleting the ammonia down to this deeper level (5 bars), we are able to achieve the 166–167 K brightness temperatures seen in the maps. This requires either $DF_{cb} < 0.1$ (Fig. 11, lower right portion) or a combination of $DF_{5bar} < 0.3$ and $EF < 4$ (Fig. 12, lower left corner). Figs. 11 and 12 are for rays propagating

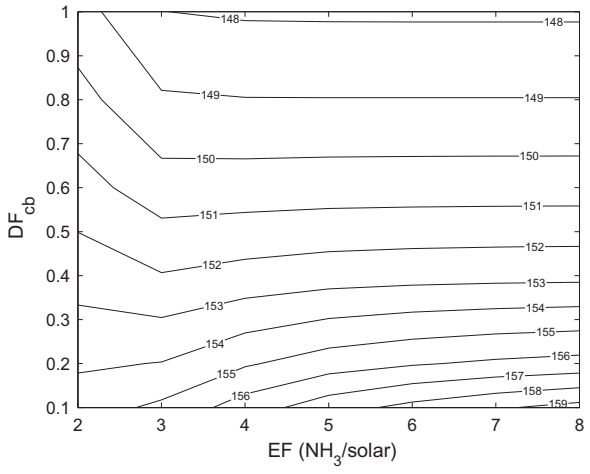

Fig. 11. Contours of model brightness temperature (in Kelvin) as a function of the ammonia depletion factor above the cloud base height, DF_{cb} (or RH), and the enrichment factor of ammonia relative to the solar abundance, EF. The warming trend at high EF is related to the way the cloud base changes with this parameter (see text for a more detailed explanation).

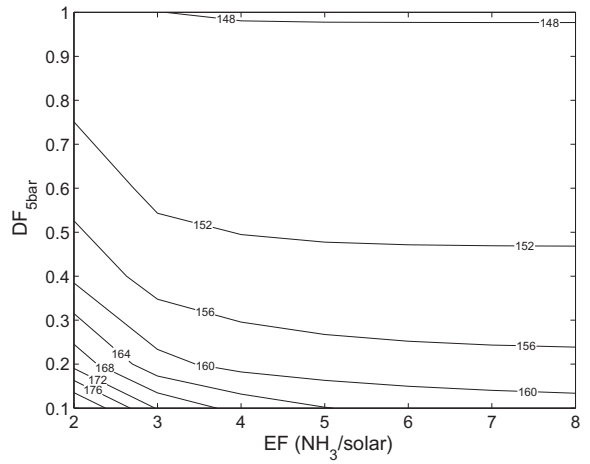

Fig. 12. Same as Fig. 11, but for the depletion factor above 5 bars, DF_{5bar}. Note the contour interval has been increased to 4 K.

vertically. Taking the limb darkening effect at 40° latitude into account means that brightness temperatures in the storm correspond to $DF_{5bar} = 0.1$ for EF = 3, which is a very large depletion (90%). The subtropical bright bands can be explained by either very low DF_{cb} or mid-range values of DF_{5bar}.

From our results it seems that ammonia lies near the 3× solar range, because at high EF values (EF > 4) it becomes impossible to achieve the highest observed brightness temperature (167 K) unless $DF_{5bar} < 0.1$ (Fig. 12). Such low values of DF are incompatible with other observations of ammonia (i.e. Fletcher et al., 2011a). Also, at low EF values (EF < 3) it becomes impossible to achieve the lowest observed brightness temperature (148 K at the equator) unless the atmosphere there is supersaturated. This is because saturation occurs at $T > 148$ K for EF < 3 (Figs. 11 and 12, top left corner). According to this analysis, Saturn's atmosphere lies in the 3–4× solar ammonia range, with fairly large depletion of ammonia extending below the cloud base in some regions.

Since the highest brightness temperature seen in all five maps is near 167 K (in the subtropical latitudes of the October 2009 map), depleting down to 2 bars could explain all the brightness temperatures we see (Fig. 4). In this case DF_{2bar} would have to be close to 0, which corresponds to no ammonia above 2 bars. This is not a likely scenario, so we focus on DF_{5bar} for the remainder of the paper, keeping in mind that DF_{5bar} is the same as DF_{3bar} or DF_{4bar} as long as $DF \geqslant 0.2$ (Fig. 4).

5. Discussion

The deep abundance of heavy elements such as nitrogen and carbon is not well known on Saturn. Estimates range from 2 to 4× solar (Atreya, 2010) for ammonia to 9–10× solar (Fletcher et al., 2012) for carbon. The solar values used in these estimates are those given in Table 1, and they are given with respect to H_2. Because we only have data at one wavelength, we cannot constrain EF and DF separately, we can only comment on possible combinations of the two parameters that give brightness temperatures consistent with the 2.2-cm data. However, as presented above, EF must lie in the 3–4× solar range in order to achieve the highest and lowest brightness temperatures observed at 2.2-cm. For the following discussion, we assume that EF = 3 and then we comment on the values of DF that would yield the observed brightness temperatures. Note that EF = 3, which corresponds to a deep volume mixing ratio of 3.6×10^{-4}, is fairly consistent with values reported by de Pater and Massie (1985) and Briggs and Sackett (1989), whose estimates are for pressure levels greater than 3 bars and the 2-bar level, respectively, and Fletcher et al. (2011a) for the 1–4 bar range at the equator. Our estimate is also consistent with the estimate of 1.2×10^{-4} obtained from VLA measurements by Grossman et al. (1989) for the condensation altitude.

5.1. All maps

Using the quantitative analysis from the radiative transfer model for 3× solar ammonia, we were able to convert the residual brightness temperatures to DF_{cb} values, or values of ammonia RH in the ammonia cloud layer. Fig. 13a shows a map of the ammonia RH for the March 2011 observation date, with the northern storm being the most prominent feature. Black regions would be regions where the atmosphere is supersaturated with respect to ammonia in the cloud layer (we do not see any). In this figure black corresponds to where the atmosphere looks very cold due to the ring obstruction. Blue regions are regions that require depletion of ammonia below the clouds in order to achieve those high brightness temperatures.

Fig. 9 shows that the global average residual brightness temperature relative to the saturated model is 1.7 ± 1.1 K, where the ±1.1 K is the real variability of longitudinally-averaged brightnesses in the atmosphere. Figs. 4, 11 and 12 give DF for various brightness temperature values, and the curves are almost flat for $X \geqslant 2$ bars (Fig. 4). In Fig. 11, each DF value is the RH at the corresponding brightness temperature. Taking brightness temperature Tb = 148 K as the saturated case and Tb = 149.7 ± 1.1 K as the global average (for EF = 3), we find that the average RH is 70 ± 15% in the cloud layer. Note that this estimate does not include the 2010–2011 northern storm, and that the ±15% comes directly from the 1.1 K variability in Fig. 9. For comparison, de Pater et al. (2001) find that the disk-averaged relative humidity of ammonia in Jupiter's atmosphere is of the order of 10% at pressures less than 0.55 bars.

Saturn's atmosphere also has local and regional features with RH < 0 in the cloud layer. These regions are shown in green–blue in Fig. 13. It is clear that the northern storm contains some rich dynamics that cause ammonia depletion below the cloud base. We discuss the northern storm in more detail Section 5.2. The subtropical bands at ±9° have a lot of structure, with alternating

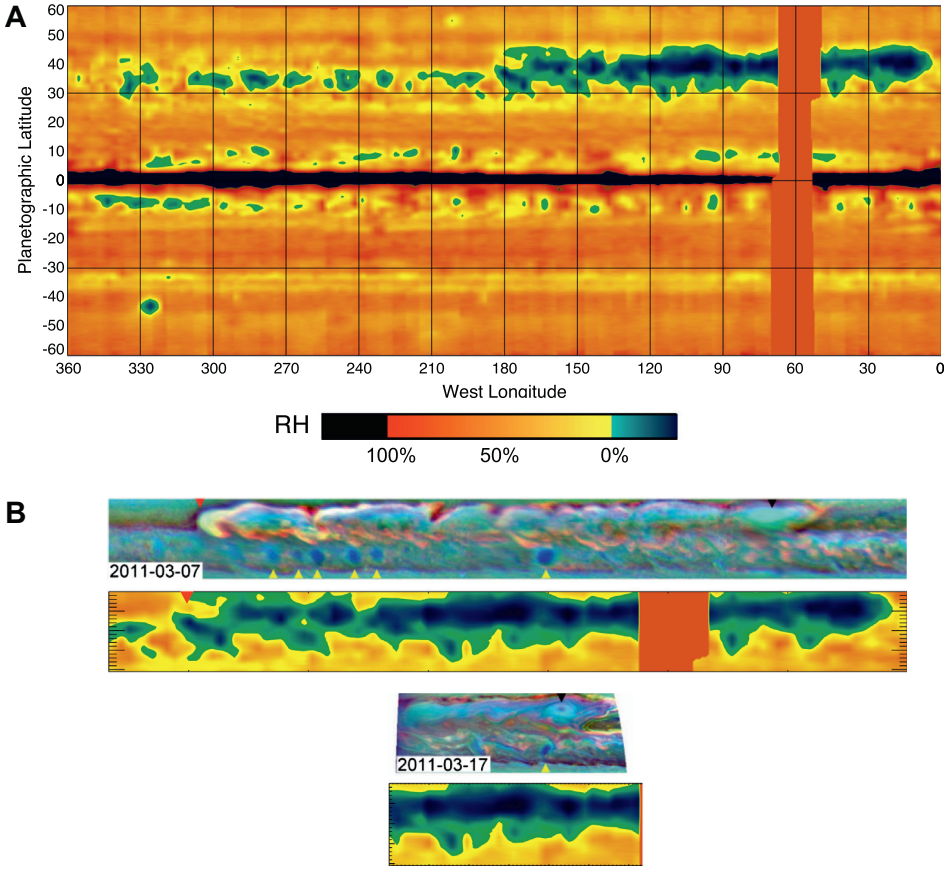

Fig. 13. (a) Map of ammonia RH in the cloud layer from March 20, 2011. Black regions would indicate supersaturation of ammonia in the cloud layer (we do not see any). Here, the black regions are due to the cold rings blocking the emission from the atmosphere. Green to blue regions are regions that require ammonia depletion below the ammonia cloud layer (i.e. RH < 0 in the cloud layer). The northern storm is blue, indicating low ammonia concentrations in the storm that extend to layers beneath the clouds. There are many local regions in the subtropical bands, as well as a storm in the southern hemisphere near 325°W, −43°, that require ammonia depletion below the clouds. (b) Two Cassini ISS images of the northern storm from Fig. 4 of Sayanagi et al. (2013), with the corresponding parts of the 2.2-cm maps show beneath each of them. These are the closest dates we have to the 2.2-cm map date. Cloud heights are distinguished by the three color filters – red (CB2 – 750 nm), green (MT2 – 727 nm), and blue (MT3 – 889 nm). (For interpretation of the references to color in this figure legend, the reader is referred to the web version of this article.)

regions of high and low ammonia RH. In every map, there are local regions in the two subtropical bands that require ammonia depletion below the cloud base. As seen by the red–orange color in the figure, the band from −15° to −30° is more humid than other latitudes. The narrow bands at −33° and −37° are drier than their surrounding latitudes. South of these bands, there is a storm near 325°W, −45° that requires ammonia depletion below the clouds.

For comparison, we look at ammonia abundances reported by Fletcher et al. (2011a). Their values were derived from Cassini–VIMS 4.6–5.1 μm spectra taken in April 2006. In Fig. 14i of their paper, the ammonia mole fraction is given as a function of latitude for their sensitivity range of 1–4 bars. There is a drastic difference between the equator and just off the equator in both hemispheres, with high ammonia abundance centered on the equator and extending to about ±5° planetocentric (±6° planetographic), and relatively low abundance at ±10° planetocentric (±12° planetographic). Our Fig. 9 is qualitatively consistent with these results—there is high ammonia at the equator (low 2.2-cm brightness temperature) and low ammonia in the subtropical bands. However, our figure suggests that there would be larger dips in the ammonia abundance in the subtropical bands than is shown in Fletcher et al. (2011a). Their Fig. 14i shows NH_3 mole fractions of 450 ppm at the equator, 110 ppm at ±8–10°, and

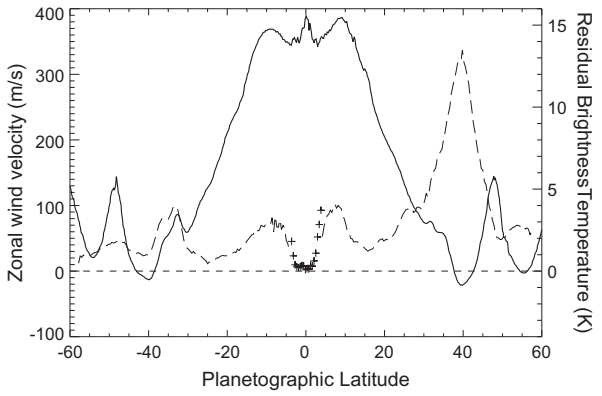

Fig. 14. Saturn zonal wind velocity (solid line) and mean residual temperature for the March 2011 map averaged over the storm longitudes (dashed line) as a function of planetographic latitude. From −4° to +4° the single December 2009 RPC scan is used (+ signs), as in Fig. 5. The zonal velocity profile used in this figure is from Cassini ISS data (García-Melendo et al., 2011).

150–200 ppm at higher latitudes. Relative to our 3× solar reference state and not correcting for the removal of ammonia due to the NH_4SH cloud, these correspond to $DF_{5bar} = 1.3$ at the equator, 0.31 at ±8–10°, and 0.42–0.56 at high latitudes. Our data require $DF_{5bar} = 1$ at the equator, 0.45–0.55 at ±8–10° and 0.8–0.9 at higher latitudes (also not correcting for the NH_4SH cloud). Thus Fletcher et al. observe less ammonia in the subtropics and high latitudes and more ammonia at the equator than we do. They also see an increase in the ammonia abundance in the southern hemisphere between −20° and −30° which is consistent with the dip in brightness temperature that we observe there (Fig. 9). Given the differences in measurement techniques and altitudes covered, our results tend to agree with those of Fletcher et al. (2011a).

What dynamical mechanisms could cause a latitudinal thermal emission profile like the one we see in Fig. 9? We consider three possibilities. The first is that the brightness temperature variations are due to real latitudinal temperature variations, with the ammonia mixing ratio independent of latitude up to cloud base and saturated above. However, Fletcher et al. (2007) derived latitudinal temperature gradients on Saturn based on Cassini/CIRS observations, and the temperature contours near the equator are nearly flat, at least below the 0.5-bar level (their Fig. 2). In contrast, we observe brightness temperature fluctuations on the order of 10 K between the bands at ±9° and the equator. Fletcher et al. (2007) do observe a temperature dip in the equatorial region above the 0.4 bar level, with colder temperatures at the equator than in the subtropics by about 5 K in the 0.2–0.4 bar region. This would be consistent with the brightness temperature pattern that we observe, but at altitudes above the 0.4-bar pressure level the density of ammonia gas is so small that we are not sensitive to these upper levels. The CIRS observations only provide temperatures above the 1 bar level so we cannot compare with the levels probed at 2.2 cm.

In the cloud region, the ammonia concentration falls off according to the saturation vapor pressure (the Clausius–Clapeyron relation). When the atmospheric temperature decreases in this region, holding the RH constant at saturation, the ammonia concentration decreases and the weighting function moves to deeper (and warmer) levels, offsetting the decrease in temperature. Thus brightness temperature variations are buffered in the cloud layer, and we would not expect to see a large change in brightness temperature due to a change in atmospheric temperature. This is the same effect that we discussed in Section 2. To confirm this, we used our radiative transfer model to test the sensitivity of the 2.2-cm brightness temperature to the model reference temperature at the 1-bar level. As we vary the reference temperature, the atmosphere remains saturated above the cloud base and the entire temperature profile shifts by approximately the same value as at the 1-bar level, including at the weighting function peak. In order to get brightness temperature variations on the order of 10 K, the 1-bar temperature needs to be varied by 50 K. The CIRS observations seem to rule out such large temperature swings from latitude to latitude, so we consider other options.

The second possibility is that upwelling in the equatorial region and downwelling on either side in each hemisphere produces an ammonia vapor distribution that is compatible with our observations. We postulate that air upwells at the equator, advecting ammonia-rich air from below, as suggested by previous authors to explain equatorial winds, composition, and clouds observed by Cassini (i.e. Yamakazi et al., 2005; Fletcher et al., 2011a). The ammonia precipitates out in the updrafts, and the dry air moves poleward, descending at latitudes out to ±9° in each hemisphere. This is the Hadley cell model. The rings of air moving poleward have to lose angular momentum to avoid spinning up while their distance to the rotation axis is decreasing. In other words, there has to be an eddy momentum flux (EMF) divergence within ±9° of the equator. On Earth, the region of EMF divergence extends to ±30°, which is the poleward edge of the Hadley cell. The subtropics, which occupy the bands from 10° to 30° in each hemisphere, are marked by net downwelling and generally low relative humidity. They are "dry," like the bands near ±9° on Saturn. On Earth the tropospheric jet streams are located in the bands from 30° to 40° in each hemisphere, and the eddies, which arise from instability of the jet streams, are responsible for the EMF divergence at lower latitudes.

There are differences between the Hadley circulation on Earth and that on Saturn. First, in the published data there is only a hint of a zonal wind maximum, i.e., a jet stream, at ±10° on Saturn (García-Melendo et al., 2011), as shown in Fig. 14. At the equator there is a zonal wind maximum, which has no terrestrial analog. Poleward of ±10° there is EMF convergence, which pumps the equatorially superrotating jets on both Saturn and Jupiter (e.g. Ingersoll et al., 1981; Salyk et al., 2006; Del Genio et al., 2007). The Hadley cell model requires that the convergence become divergence within ±9° of the equator. This seems to work for Jupiter, which has zonal wind maxima at ±6–7° (planetocentric) and EMF divergence between ±5° (planetocentric), i.e., $\overline{u'v'}$ increasing with latitude from −5° to +5° (see Fig. 5 of Salyk et al., 2006). Whether it works for Saturn is uncertain, because trackable cloud features are scarce close to the equator and it has been impossible to measure the EMF there.

Lack of a solid surface to add angular momentum on the return flow is another difference between Earth and Saturn. On Earth, the low latitude easterlies gain westerly angular momentum from the surface as the air moves toward the equator. It is not clear that this would happen on a fluid planet. The return flow could be at any depth, and we do not know if rings of fluid exchange angular momentum there or not. Right now, the pieces of evidence for the Hadley cell model on Saturn are the high ammonia abundance at the equator, the low ammonia abundance and hint of zonal velocity maxima near ±9°, and the observed EMF divergence in the band at Jupiter's equator.

Fletcher et al. (2011a) present evidence that two stacked meridional circulation cells, rotating in opposite directions, exist in Saturn's troposphere. From analysis of Cassini VIMS data, they find that deep PH_3 and AsH_3 show local maxima on either side of the equator, whereas the PH_3 scale height, the upper cloud opacity, and the NH_3 show local maxima at the equator. Stacked cells seem to explain the contradictory evidence of upwelling and downwelling both on and off the equator. As Fletcher et al. point out, the stacked cell hypothesis was originally invoked at Jupiter (Ingersoll et al., 2000; Gierasch et al., 2000; Showman and de Pater, 2005), where upper cloud opacity and NH_3 indicated upwelling in the zones, but lightning and other evidence of moist convection indicated upwelling in the belts. Other authors also explore the possibility of meridionally overturning cells in Saturn's atmosphere (i.e. Del Genio et al., 2009). Since the present paper mainly concerns NH_3, we do not attempt to synthesize all the Saturn data at this time.

5.2. 2010–2011 Northern storm

The third possibility is that there is some process in giant planet atmospheres that causes the "drying out" following convective events. The northern storm in the March 2011 map is very dry with respect to ammonia vapor (Fig. 13). What is it about the storm that produces such low ammonia RH? The head of the storm is at 40°, 180°W (Sayanagi et al., 2013), and is indicated by the red triangle at the top of the figure in Fig. 13b. The green to blue trail to the west of the head is the tail of the storm, which wrapped all the way around the planet until it collided with the head in February 2011 (Fischer et al., 2011). By March 20, 2011, when this 2.2-cm data was collected, the storm had been in existence for almost

4 months. The storm was a copious producer of lightning, which was detected at radio frequencies (Fischer et al., 2011) and in visible light (Dyudina et al., in preparation). Fig. 13 shows that, although the storm is very dry everywhere (RH $\leqslant$ 0, Fig. 13a), there is also quite a bit of brightness temperature structure within the storm, which may be compatible with the Sánchez-Lavega et al. (2012) description of the three branches of the storm and the wave-like patterns within the storm tail.

Fig. 13b shows images taken by the Cassini imaging science subsystem (ISS) on March 7 and March 17, 2011 (Sayanagi et al., 2013), with the corresponding pieces of the RADAR maps below them (from March 20, 2011). The top panel of Fig. 13b spans 0–200°W longitude, and the bottom panel spans 60–130°W longitude. Both panels show 24.5–45° planetographic latitude (20.5–40° planetocentric). Red, green and blue color channels correspond to Cassini ISS camera's CB2 (750 nm), MT2 (727 nm), and MT3 (889 nm) filters, respectively, and they convey the cloud top heights. The altitude of the features generally increases in the order of red–green–blue (Sayanagi et al., 2013). There are no images closer in time to the March 20, 2011 radiometer image in Fig. 13a, for several reasons. Most important, the two instruments point along different axes of the spacecraft and cannot take data simultaneously. Also, the 2.2-cm map is taken near closest approach, when the field of view of the wide-angle camera is 15–20° latitude, which is a small fraction of the planet. Finally, the observations were scheduled months in advance, long before the advent of the storm. Thus the detailed features in Fig. 13a are not necessarily the same features that appear in the ISS images in Fig. 13b. Some features, however, seem to be captured by the RADAR map, for example the anticyclonic vortex appears as a circular region of low RH (dark blue) near 15°W. For an example of the changes that take place over an 11-h period, see Fischer et al. (2011).

Fig. 14 shows the zonal wind velocity (solid line) as a function of latitude with the March 2011 residual temperature averaged over the longitudes of the storm (dashed line) overlaid on it. The + - signs between −4° and 4° depict the December 2009 RPC scan brightness residuals used in Fig. 9. Storm alley in the southern hemisphere lies in the westward jet between −40° and −45°. The northern storm is also located in a westward jet, but in the opposite hemisphere. The head of the storm is centered in the middle of the westward jet near 41° (35° planetocentric, Fischer et al., 2011). Some of the depletion of ammonia vapor by the northern storm gets pushed slightly to the north of the westward jet, which is consistent with work by Fletcher et al. (2011b) and Sánchez-Lavega et al. (2012), who observe two eastward branches to the north and south of the storm, with ammonia vapor depletion in the southern branch (Fletcher et al., 2011b). This pattern may be analogous to the storms in the southern hemisphere which are to the south of the westward jet (Porco et al., 2005). We suspect that the mechanism for "drying out" the small storms in the southern hemisphere and the 2010–2011 northern storm are the same. Ammonia depletion is consistent with the ISS (imaging science subsystem) team's interpretation of their observations of the southern storms at near-IR wavelengths. To measure clouds at various altitudes, they use three filters, like in Fig. 13b, where the absorption by methane gas is strong, weak, and negligible, respectively (Porco et al., 2005; Dyudina et al., 2007). From their observations they infer that on the first day the storms are active convective regions of optically thick, high clouds. On the third or fourth day they become stable circular clouds with optically thin, high haze above dark regions with no deep clouds – they become holes in the clouds. If the clouds are made of ammonia ice, then a hole in the clouds is consistent with depletion of ammonia vapor.

The VIMS (visible and infrared imaging spectrometer) team uses 352-bandpass spectra ranging from 0.35 to 5.1 μm, although the instrument has other ranges and resolutions. The dark regions seen in the near-IR are dark at all wavelengths, and Baines et al. (2009) interpret them as carbon-impregnated water frost rather than absence of deep clouds, the latter being the ISS interpretation. The carbon could come from dissociation of methane by lightning, since these are lightning clouds (Dyudina et al., 2007; Fischer et al., 2011).

Both the ISS description and the VIMS description seem to explain the dark color of the convective clouds after the third day. The low RH of ammonia inferred from the 2.2-cm observations favors a hole in the clouds if the cloud particles are ammonia ice. The 2010–2011 northern storm, whose head resembles the high, thick convective clouds in ISS images, and whose tail is depleted in ammonia in the 2.2-cm maps, also supports the hole-in-the-cloud interpretation. Of course, the tail could be depleted in ammonia clouds and ammonia vapor but still have carbon-impregnated water ice clouds. The VIMS spectra of the head and tail of the northern storm will help resolve these different interpretations.

Convective storms seem to evolve into ammonia-poor regions, both in the southern hemisphere hot spots and in the northern storm. Also, the remnant of the northern storm is bright at 5 μm, which signals "an unusual dearth of deep clouds" (Baines, private communication, 2012). This agrees with the ISS interpretation of the southern hemisphere dark spots – that deep clouds are absent. So the question arises, why should convection "dry out" the atmosphere – removing gaseous ammonia and deep clouds? The answer may be in the nature of convection in hydrogen–helium atmospheres, in particular in the effect of mass loading by molecules of NH_3, H_2S, and H_2O, which have higher molecular mass than the ambient atmosphere. The parcels that have lost their load of the more massive molecules will have the most buoyancy, and they might rise the highest. These parcels would look "dry" when viewed from the top of the atmosphere. Mass loading might also explain the intermittency of convection on Saturn, but the details have yet to be worked out.

There are several models of moist convection in giant planet atmospheres. Some are axially symmetric (Yair et al., 1995a,b), and some are three dimensional (Hueso and Sánchez-Lavega, 2004), with the possibility of wind shear and precipitation on one side of the central updraft. These models start with an unstable initial state and follow the convective plume as it develops over a period of several hours or 1 day. Other models incorporate cumulus parameterizations into giant planet general circulation models (Del Genio and McGrattan, 1990; Palotai and Dowling, 2008). Sánchez-Lavega et al. (2012) studied a mass source in a shear flow patterned after the westward jet at 40° planetographic that produces a GWS (Great White Spot) long tail. To the best of our knowledge, none of these models capture the 20–30 year cycle of planet-encircling storms or the ammonia depletion following convective events.

6. Conclusions

J13 used the 2.2-cm brightness temperature observations of Saturn presented in conjunction with radiative transfer calculations to produce residual brightness temperature maps for five dates between 2005 and 2011. In this work we analyzed the maps by making adjustments to the vertical ammonia distribution using the JAMRT program. We find that ammonia vapor must be depleted below the cloud base in some regions in order to obtain temperatures in agreement with observations. The observed brightness temperatures are consistent with a deep abundance of 3–4× solar ammonia ($3.6–4.8 \times 10^{-4}$ volume mixing ratio) with varying depletion factors relative to the standard model, which is saturated above cloud base. The depletion must extend to 2 bars or deeper for brightness temperatures >160 K. To obtain these

results, we assume that Saturn's latitudinal temperature profile is constant in our sensitivity range of 0.5–2 bars. The highest brightness temperatures we see are in the 2010–2011 northern storm (165.7 K) and in the subtropical latitudes of the October 2009 map (167 K). The most striking feature, evident in Fig. 9, is the difference in the 2.2-cm brightness temperature right at the equator versus that just off the equator. This implies that there are some interesting atmospheric dynamics at play in the equatorial region.

We presented three options to explain the brightness temperature pattern observed at 2.2-cm. One is that it represents real temperature variations, i.e., temperature variations from place to place at constant levels in the atmosphere. In principle, brightness temperature variations can be due to both physical temperature and absorber concentrations; however, the buffering effect makes the former option unlikely in our case. The second option is that large-scale upwelling and downwelling, like the Earth's Hadley circulation, creates dry zones like the subtropics of Earth. However this option does not explain the drying that follows the small-scale convective events in the southern hemisphere. The third option, which we do not explore in any depth, is that the drying is an intrinsic property of convection in giant planet atmospheres, and that it applies not just to the small southern lightning storms but also to the northern storm of 2010–2011. The subtropical dry bands are not copious producers of lightning and moist convection, so the third option might not apply there. It may that that the meridional circulation explanation applies to the subtropics, and the deep convection explanation applies to the lightning storms.

Modeling of atmospheric circulations on giant planets has proven difficult, and the lack of observational data in the deep atmosphere below the clouds is a limitation. It is important to try to reconcile the atmospheric motions with latitudinal distributions of tropospheric gases such as NH_3 and PH_3. This paper provides some insight into the distribution of ammonia vapor, with the hope that more work can be done with these observations to reconcile them with the energy and momentum balances of Saturn's atmosphere.

Acknowledgments

This research was conducted at the California Institute of Technology under contract with the National Aeronautics and Space Administration (NASA). It is partly based upon work supported by NASA under Grant No. 10-CDAP10-0051 issued through the Cassini Data Analysis and Participating Scientist (CDAPS) Program. A. Laraia was partially funded by a National Science Foundation (NSF) Graduate Research Fellowship Program (GRFP) fellowship. We acknowledge Sushil Atreya, Lena Adams, and Virgil Adumantroi for their invaluable contributions to the Juno atmospheric microwave radiative transfer (JAMRT) program. We would also like to acknowledge Kevin Baines for useful discussions on comparing RADAR and VIMS data.

References

Allison, M., 1990. Planetary waves in Jupiter's equatorial atmosphere. Icarus 83, 282–307.

Arregi, J., Rojas, J.F., Sánchez-Lavega, A., Morgado, A., 2006. Phase dispersion relation of the 5-μm hot spot wave from a long-term study of Jupiter in the visible. J. Geophys. Res. 111 (E09010), 1–10.

Atreya, S.K., 2010. Atmospheric moons Galileo would have loved. In: Galileo's Medicean Moons – Their Impact on 400 years of Discovery. Cambridge University Press, pp. 130–140 (Chapter 16).

Baines, K.H. et al., 2009. Storm clouds on Saturn: Lightning-induced chemistry and associated materials consistent with Cassini/VIMS spectra. Planet. Space Sci. 57, 1650–1658.

Briggs, F.H., Sackett, P.D., 1989. Radio observations of Saturn as a probe of its atmosphere and cloud structure. Icarus 80, 77–103.

de Pater, I., Massie, S.T., 1985. Models of the millimeter–centimeter spectra of the giant planets. Icarus 62, 143–171.

de Pater, I., Dunn, D., Romani, P., Zahnle, K., 2001. Reconciling Galileo probe data and ground-based radio observations of ammonia on Jupiter. Icarus 149, 66–78.

Del Genio, A.D., McGrattan, K.B., 1990. Moist convection and the vertical structure and water abundance of Jupiter's atmosphere. Icarus 84, 29–53.

Del Genio, A.D., Barbara, J.M., Ferrier, J., Ingersoll, A.P., West, R.A., Vasavada, A.R., Spitale, J., Porco, C.C., 2007. Saturn eddy momentum fluxes and convection: First estimates from Cassini images. Icarus 189, 479–492.

Del Genio, A.D. et al., 2009. Saturn atmospheric structure and dynamics. In: Saturn from Cassini–Huygens. Springer, pp. 113–159 (Chapter 6).

Dyudina, U.A., Ingersoll, A.P., Ewald, S.P., Porco, C.C., Fischer, G., Kurth, W., Desch, M., Del Genio, A., Barbara, J., Ferrier, J., 2007. Lightning storms on Saturn observed by Cassini ISS and RPWS during 2004–2006. Icarus 190, 545–555.

Elachi, C. et al., 2004. RADAR: The Cassini Titan radar mapper. Space Sci. Rev. 115, 71–110.

Fischer, G., Desch, M.D., Zarka, P., Kaiser, M.L., Gurnett, D.A., Kurth, W.S., Macher, W., Rucker, H.O., Lecacheux, A., Farrell, Cecconi, B., 2006. Saturn lightning recorded by Cassini/RPWS in 2004. Icarus 183, 135–152.

Fischer, G., Kurth, W.S., Dyudina, U.A., Kaiser, M.L., Zarka, P., Lecacheux, A., Ingersoll, A.P., Gurnett, D.A., 2007. Analysis of a giant lightning storm on Saturn. Icarus 190, 528–544.

Fischer, G. et al., 2011. A giant thunderstorm on Saturn. Nature 475, 75–77.

Fletcher, L.N., Irwin, P.G.J., Teanby, N.A., Orton, G.S., Parrish, P.D., de Kok, R., Howett, C., Calcutt, S.B., Bowles, N., Taylor, F.W., 2007. Characterising Saturn's vertical temperature structure using Cassini/CIRS. Icarus 189, 457–478.

Fletcher, L.N., Baines, K.H., Momary, T.W., Showman, A.P., Irwin, P.G.J., Orton, G.S., Roos- Serote, M., Merlet, C., 2011a. Saturn's tropospheric composition and clouds from Cassini/VIMS 4.6–5.1 μm nightside spectroscopy. Icarus 214, 510–533.

Fletcher, L.N. et al., 2011b. Thermal structure and dynamics of Saturn's northern springtime disturbance. Science 332, 1413–1417. http://dx.doi.org/10.1126/science.1204774.

Fletcher, L.N. et al., 2012. Sub-millimetre spectroscopy of Saturn's trace gases from Herschel/SPIRE. Astron. Astrophys. 539, A44. http://dx.doi.org/10.1051/0004-6361/201118415.

García-Melendo, E., Pérez-Hoyos, S., Sánchez-Lavega, A., Hueso, R., 2011. Saturn's zonal wind profile in 2004–2009 from Cassini ISS images and its long-term variability. Icarus 215, 62–74.

Gierasch, P.J. et al., 2000. Observation of moist convection in Jupiter's atmosphere. Nature 403, 628–630.

Grevesse, N., Asplund, M., Sauval, A.J., 2005. The new solar chemical composition. EAS Publ. Ser. 17, 21–30. http://dx.doi.org/10.1051/eas:2005095.

Grossman, A.W., Muhleman, D.O., Berge, G.L., 1989. High resolution microwave observations of Saturn. Science 245, 1211–1215.

Hueso, R., Sánchez-Lavega, A., 2004. A three-dimensional model of moist convection for the giant planets. II: Saturn's water and ammonia moist convective storms. Icarus 172, 255–271.

Ingersoll, A., Beebe, R., Mitchell, J., Garneau, G., Yagi, G., Muller, J., 1981. Interaction of eddies and mean zonal flow on Jupiter as inferred from Voyager 1 and 2 images. J. Geophys. Res. 86, 8733–8743.

Ingersoll, A.P., Gierasch, P.J., Banfield, D., Vasavada, A.R.Galileo Imaging Team, 2000. Moist convection as an energy source for the large-scale motions in Jupiter's atmosphere. Nature 403, 630–632.

Janssen, M.A., Hofstadter, M.D., Gulkis, S., Ingersoll, A.P., Allison, M.D., Bolton, S.J., Kamp, L.W., 2005. Microwave remote sensing of Jupiter's atmosphere from an orbiting spacecraft. Icarus 173, 447–453.

Janssen, M.A., Lorenz, R.D., West, R., Paganelli, F., Lopes, R.M., Kirk, R.L., Elachi, C., Wall, S.D., Johnson, W.T.K., Anderson, Y., Boehmer, R.A., Callahan, P., Gim, Y., Hamilton, G.A., Kelleher, K.D., Roth, L., Stiles, B., Le Gall, A.the Cassini Radar Team, 2009. Titan's surface at 2.2-cm wavelength imaged by the Cassini RADAR radiometer: Calibration and first results. Icarus 200, 222–239.

Janssen, M.A., Ingersoll, A.P., Allison, M.D., Gulkis, S., Laraia, A.L., Baines, K., Edgington, S., Anderson, Y., Kelleher, K., Oyafuso, F., 2013. Saturn's thermal emission at 2.2-cm wavelength as imaged by the Cassini RADAR radiometer. Icarus, this issue.

Kaiser, M.L., Connerney, J.E.P., Desch, M.D., 1983. Atmospheric storm explanation of saturnian electrostatic discharges. Nature 303, 50–53.

Lindal, G.F., Sweetnam, D.N., Eshleman, V.R., 1985. The atmosphere of Saturn: An analysis of the Voyager radio occultation measurements. Astron. J. 90, 1136–1146.

Palotai, C., Dowling, T.E., 2008. Addition of water and ammonia cloud microphysics to the EPIC model. Icarus 194, 303–326.

Porco, C.C. et al., 2005. Cassini imaging science: Initial results on Saturn's atmosphere. Science 307, 1243–1247.

Salyk, C., Ingersoll, A.P., Lorre, J., Vasavada, A., Del Genio, A.D., 2006. Interaction between eddies and mean flow in Jupiter's atmosphere: Analysis of Cassini imaging data. Icarus 185, 430–442.

Sánchez-Lavega, A., Rojas, J.F., Sada, P.V., 2000. Saturn's zonal winds at cloud level. Icarus 147, 405–420.

Sánchez-Lavega, A. et al., 2011. Deep winds beneath Saturn's upper clouds from a seasonal long-lived planetary-scale storm. Nature 475, 71–74.

Sánchez-Lavega, A., del Río-Gaztelurrutia, T., Delcroix, M., Legarreta, J.J., Gómez-Forrellad, J.M., Hueso, R., García-Melendo, E., Pérez-Hoyos, S., Barrado-Navascués, D., Lillo, J.International Outer Planet Watch Team IOPW-PVOL, 2012. Ground-based observations of the long-term evolution and death of Saturn's 2010 Great White Spot. Icarus 220, 561–576.

Sayanagi, K., Dyudina, U.A., Ewald, S.P., Fischer, G., Ingersoll, A.P., Kurth, W.S., Muro, G.D., Porco, C.C., West, R.A., 2013. Dynamics of Saturn's great storm of 2010–2011 from Cassini ISS and RPWS. Icarus 223, 460–478.

Showman, A.P., de Pater, I., 2005. Dynamical implications of Jupiter's tropospheric ammonia abundance. Icarus 174, 192–204.

West, R.A., Baines, K.H., Karkoschka, E., Sánchez-Lavega, A., 2009. Clouds and aerosols in Saturn's atmosphere. In: Saturn from Cassini–Huygens. Springer, pp. 161–179 (Chapter 7).

Yair, Y., Levin, Z., Tzivion, S., 1995a. Microphysical processes and dynamics of a jovian thundercloud. Icarus 114, 278–299.

Yair, Y., Levin, Z., Tzivion, S., 1995b. Lightning generation in a jovian thundercloud: Results from an axisymmetric numerical cloud model. Icarus 115, 421–434.

Yamakazi, Y.H., Read, P.L., Skeet, D.R., 2005. Hadley circulations and Kelvin wave-driven equatorial jets in the atmospheres of Jupiter and Saturn. Planet. Space Sci. 53, 508–525.

Chapter 3

Superrotation in terrestrial atmospheres

[0]This article has been submitted to the Journal of Atmospheric Sciences.

JOURNAL OF THE ATMOSPHERIC SCIENCES

Superrotation in Terrestrial Atmospheres

ANNE L. LARAIA

California Institute of Technology, Pasadena, California

TAPIO SCHNEIDER*

ETH Zurich, Zurich, Switzerland, and California Institute of Technology, Pasadena, California

ABSTRACT

Atmospheric superrotation with prograde equatorial winds and an equatorial angular momentum maximum is ubiquitous in planetary atmospheres. It is clear that eddy fluxes of angular momentum toward the equator are necessary to generate it. But under what conditions superrotation arises has remained unclear. This paper presents simulations and a scaling theory that establish conditions under which superrotation occurs in terrestrial atmospheres. Whether superrotation arises depends on the relative importance of factors that favor or disfavor superrotation. Convection preferentially generates Rossby waves near the equator, where the Rossby number is $O(1)$. Since the Rossby waves transport angular momentum toward their source regions, this favors superrotation. Meridional temperature gradients preferentially lead to baroclinic instability and wave generation away from the equator. Eddy transport of angular momentum toward the baroclinic source region implies transport out of low latitudes, which disfavors superrotation. Simulations with an idealized GCM show that superrotation tends to arise when the equatorial convective generation of wave activity and its associated eddy angular momentum flux convergence exceed the baroclinic eddy angular momentum flux divergence. Convective and baroclinic wave activity generation are related through scaling arguments to mean flow properties such as planetary rotation rates and meridional temperature gradients. The scaling arguments show, for example, that superrotation is favored when the off-equatorial baroclinicity and planetary rotation rates are low, as they are, for example, on Venus. Similarly, superrotation is favored when the convective heating strengthens, which may account for the superrotation seen in extreme global-warming simulations.

1. Introduction

Atmospheric superrotation refers to a local angular momentum maximum in the fluid interior. Because angular momentum must decrease toward the poles for the flow to be inertially stable, atmospheric superrotation usually means equatorial superrotation, that is, a local angular momentum maximum at the equator (Held 1999). Such atmospheric superrotation may be the norm rather than the exception. Venus and Titan have superrotating atmospheres (Schubert 1983; Gierasch et al. 1997; Kostiuk et al. 2001). Jupiter's and Saturn's atmospheres also superrotate (Porco et al. 2003; Sánchez-Lavega et al. 2007), but because they do not have a solid surface, they superrotate relative to the rotation of their cores and magnetic fields. For an atmosphere to superrotate, it needs to have angular momentum fluxes into the region of superrotation (Hide 1969). Inviscid axisymmetric circulations cannot accomplish this upgradient angular momentum transport; eddies must be involved (Held and Hou 1980; Schneider 2006). In general, in sufficiently rapidly rotating atmospheres, eddy angular momentum fluxes converge into the regions in which wave activity is generated, and they diverge where wave activity is dissipated (Held 1975; Andrews and Mcintyre 1976; Edmon et al. 1980). Thus, preferential wave activity generation near the equator is a prerequisite for superrotation. This must not be overcompensated by wave activity dissipation near the equator, for example, associated with baroclinic eddies that are generated in midlatitudes and dissipate in lower latitudes, as they do on Earth (Saravanan 1993).

Various mechanisms are available for preferential wave activity generation near the equator. A stationary heat source near the equator, for example, leads to the generation of stationary Rossby waves, which can dissipate away from the equator and so transport angular momentum toward the equator. This leads to superrotation when the heat source is strong enough (Suarez and Duffy 1992; Saravanan 1993; Kraucunas and Hartmann 2005; Arnold et al. 2012). The stationary-wave mechanism is responsible for superrotation in simulations of tidally locked planets, in which stellar heating is radially symmetric around an equatorial focal point (Joshi et al. 1997; Merlis and Schneider 2010; Pierrehumbert 2011). For a planet with-

*Corresponding author address: Tapio Schneider, ETH Zurich, Sonneggstr. 5, 8092 Zurich, Switzerland
E-mail: tapio@ethz.ch

out deviations from axisymmetry in boundary conditions, it is less obvious why waves should be preferentially generated near the equator. Wang and Mitchell (2014) and Pinto and Mitchell (2014) find that a Rossby-Kelvin instability produces angular momentum flux convergence at the equator that is responsible for the generation of superrotation in statically stable atmospheres. In convecting atmospheres, the variation of the Rossby number with latitude provides an alternative mechanism: Near the equator, where the Rossby number can be $O(1)$, horizontal and temporal temperature variations are small when the Froude number is small. Therefore, fluctuations in convective heating must be balanced by vertical motion and hence by horizontal divergence at the level of the convective outflows in the upper troposphere (Charney 1963; Sobel et al. 2001). The horizontal divergence then can generate large-scale rotational flow and thereby Rossby waves, either by vortex stretching or vorticity advection (Sardeshmukh and Hoskins 1988). In contrast, in higher latitudes, where the Rossby number is small, convective heating fluctuations can, for example, be balanced by transient temperature fluctuations, which may relax radiatively, without generating large-scale waves that dissipate in other latitude bands. The net result is preferential generation of Rossby waves near the equator by convective heating fluctuations. If some of these convectively generated Rossby waves dissipate at higher latitudes—for example, through interaction with the mean-flow shear—they will transport angular momentum toward the equator and thus can generate superrotation (Schneider and Liu 2009; Liu and Schneider 2010).

However, angular momentum flux convergence associated with preferential wave activity generation at the equator may be counterbalanced or overcompensated by angular momentum flux divergence associated with dissipation of wave activity that was generated at higher latitudes, e.g., by baroclinic instability (Saravanan 1993). This is the case in Earth's troposphere in the annual mean, and it may be the case on Uranus and Neptune, which are subrotating (Liu and Schneider 2010). Only when the baroclinically unstable region is moved into low latitudes by artificially increasing radiative heating gradients near the equator and reducing them in higher latitudes can baroclinic instability promote the onset of superrotation (Williams 2003).

Here we focus on equatorial superrotation on terrestrial planets, that is, planets with solid surfaces with a distribution of radiative heating rates resembling Earth's. We explore a wide parameter regime that encompasses subrotating (Earth-like) and superrotating atmospheres. Our goal is to elucidate the mechanisms that generate and maintain tropospheric superrotation in convecting atmospheres and quantify the conditions under which superrotation generally arises.[1] We quantify the relative importance of the angular momentum fluxes associated with equatorial convectively generated waves and off-equatorial baroclinic eddies. We use simulations with an idealized GCM to demonstrate that whether superrotation occurs in terrestrial atmospheres depends on the competition between the two, and we use scaling arguments to estimate their relative importance in terms of mean flow quantities and external parameters.

2. Idealized GCM and simulations

The idealized GCM used for these simulations is based on the dynamical core of the Geophysical Fluid Dynamics Laboratory's Flexible Modeling System. It performs a time integration of the primitive equations of motion on a sphere with Earth's radius, using the spectral transform method in the horizontal and using 30 σ-levels in the vertical. Here, $\sigma = p/p_s$ is a dimensionless vertical coordinate, where p is the pressure and p_s the surface pressure; it ranges from 1 at the surface to 0 at the top of the atmosphere. All simulations were performed at T85 horizontal resolution.

Neither seasonal nor diurnal cycles of insolation are included in this model, and there is no topography. The GCM treats the atmosphere as an ideal gas, without an hydrologic cycle. The effects of moisture are generally ignored, but they are implicit in a convection parameterization, which relaxes atmospheric temperatures to a profile with lapse rate equal to a fraction $\gamma \leq 1$ of the dry-adiabatic lapse rate $\Gamma_d = g/c_p \approx 9.8$ K km^{-1}. Whenever an atmospheric column is less stable than the specified convective lapse rate $\gamma\Gamma_d$, a dry convection scheme relaxes temperatures to a profile with the convective lapse rate $\gamma\Gamma_d$, while conserving the column-integrated enthalpy (Schneider and Walker 2006). That is, the convection scheme assumes that the kinetic energy of the convection is locally dissipated on the convective (subgrid) scale, so that the enthalpy on the large (grid) scale is conserved. The rescaling factor γ mimics the effect of latent heat release in moist convection, with smaller γ corresponding to more latent heat release.

A Newtonian relaxation scheme represents radiative forcing by relaxing temperatures toward radiative-equilibrium temperatures T_e. Unlike the usual statically stable equilibrium temperature fields used in many idealized dry GCMs, these radiative-equilibrium temperatures are statically unstable in the lower and middle troposphere. The radiative-equilibrium surface temperature in the model is a function of latitude and is given by

$$T_s^e(\phi) = \tilde{T}_s^e + \Delta_h \cos^2\phi. \tag{1}$$

[1] Superrotation can also occur in the stratosphere, for example, during the westerly phase of the quasi-biennial oscillation. The mechanisms responsible for that are different from those in the troposphere, which is our focus here.

The radiative-equilibrium surface temperature at the pole is fixed at $\tilde{T}_s^e = 260$ K in all simulations. Radiative-equilibrium temperatures in the atmosphere above the surface are those of a semi-gray atmosphere with a water-vapor-like absorber. Their meridional gradient smoothly decays to zero at the top of the atmosphere, where the radiative-equilibrium temperature is a constant 200 K. See Schneider (2004) for more details on the Newtonian relaxation scheme, and Schneider and Walker (2006) for a more detailed model description. The only difference between our model and that described in Schneider and Walker (2006) is that we represent subgrid-scale dissipation by an exponential cutoff filter (Smith et al. 2002), with a damping timescale of 4 minutes on the smallest resolved scale, and a cutoff wavenumber of 21 below which subgrid-scale dissipation is zero. Weaker subgrid-scale damping would have sufficed for many simulations but led to substantial noise in some superrotating simulations, especially the ones with weak meridional temperature gradients and more stable convective lapse rates. Thus, we use the stronger damping for all simulations to be consistent. We also found the magnitude of the superrotating windspeed to be quite sensitive to the damping timescale.

We performed 60 simulations by varying three model parameters: The pole-equator temperature contrast in radiative equilibrium Δ_h, the planetary rotation rate Ω, and the rescaling parameter γ in the convective lapse rate $\gamma\Gamma_d$. Table 1 shows the different parameter values used to create a range of different climate scenarios. We chose to vary these parameters because based on previous work (e.g., Del Genio et al. 1993; Del Genio and Zhou 1996; Liu and Schneider 2011; Mitchell and Vallis 2010; Potter et al. 2014; Pinto and Mitchell 2014), they seemed to be pertinent to the generation of superrotation. Because rescaling the planetary rotation rate in a hydrostatic model like ours is dynamically equivalent to rescaling both the planetary radius and diabatic heating rates (e.g., Kuang et al. 2005; Garner et al. 2007), we did not consider separate variations of the planetary radius. However, variations of diabatic timescales would be interesting to explore systematically in a future study (cf. Yamamoto and Takahashi 2006; Pinto and Mitchell 2014).

Parameter	Values
Ω	[2, 1, 2^{-1}, 2^{-2}, 2^{-3}] Ω_e
Δ_h	[30, 60, 120, 240] K
γ	[0.5, 0.7, 0.9]

TABLE 1. Parameters varied in the 60 simulations: Planetary rotation rate Ω (as a multiple of Earth's rotation rate Ω_e), pole-equator temperature contrast in radiative equilibrium Δ_h, and rescaling parameter γ of the convective lapse rate $\Gamma = \gamma\Gamma_d$.

All simulations were integrated for at least 1500 days, and the model output is averaged over the last 400 days of each simulation.

3. Results

a. Circulation variations

Our goal is to determine why some simulations superrotate and some do not. Figure 1 displays two superrotating and two subrotating simulations. The left column shows the eddy angular momentum flux divergence (colors) and zonal wind (black contours), and the right column shows the mass-flux streamfunction, with solid lines for counterclockwise rotation and dotted lines for clockwise rotation. The top row shows an Earth-like reference simulation, with Earth's rotation rate $\Omega = \Omega_e$, a convective lapse rate of $\Gamma \approx 6.9$ K km^{-1} ($\gamma = 0.7$), and pole-equator radiative-equilibrium temperature contrast of $\Delta_h = 120$ K. Like on Earth, there are two westerly jets located in the upper troposphere in midlatitudes, with weak easterlies at the equator and poles. In the right column, we can see the Hadley circulation in the tropics and the Ferrel cells in midlatitudes.

The simulation in the second row has the same Earth-like parameter values for convective lapse rate and pole-equator temperature contrast but a planetary rotation rate $\Omega = \Omega_e/8$. The westerly jets are situated farther poleward, and the surface easterlies at the equator are very weak. The equatorial upper troposphere is strongly superrotating, with strong eddy angular momentum flux convergence in the superrotating region. The Hadley cells have expanded poleward as well (Walker and Schneider 2006).

The simulation in the third row is one with Earth's parameter values except for a smaller, more stable convective lapse rate $\Gamma \approx 4.9$ K km^{-1} ($\gamma = 0.5$). The Hadley cells weaken (note the difference in contour interval among the different simulations), because the reduced baroclinicity implies reduced eddy angular momentum flux divergence in the subtropics (Walker and Schneider 2006). Additionally, the zonal jets extend farther equatorward than in the reference simulation in the top row.

The simulation in the bottom row differs from the simulation above it only in the reduced pole-equator radiative-equilibrium temperature contrast of $\Delta_h = 30$ K. Decreasing the baroclinicity of the atmosphere produces a superrotating atmosphere, with a much weaker meridional circulation.

All other parameters held constant, a decrease in the planetary rotation rate generally leads to an increase in the average equatorial windspeed (Fig. 2). There are deviations from this behavior that occur at the lowest rotation rates, when the midlatitude westerly jets migrate toward the poles, as was already seen in simulations by Del Genio and Zhou (1996).

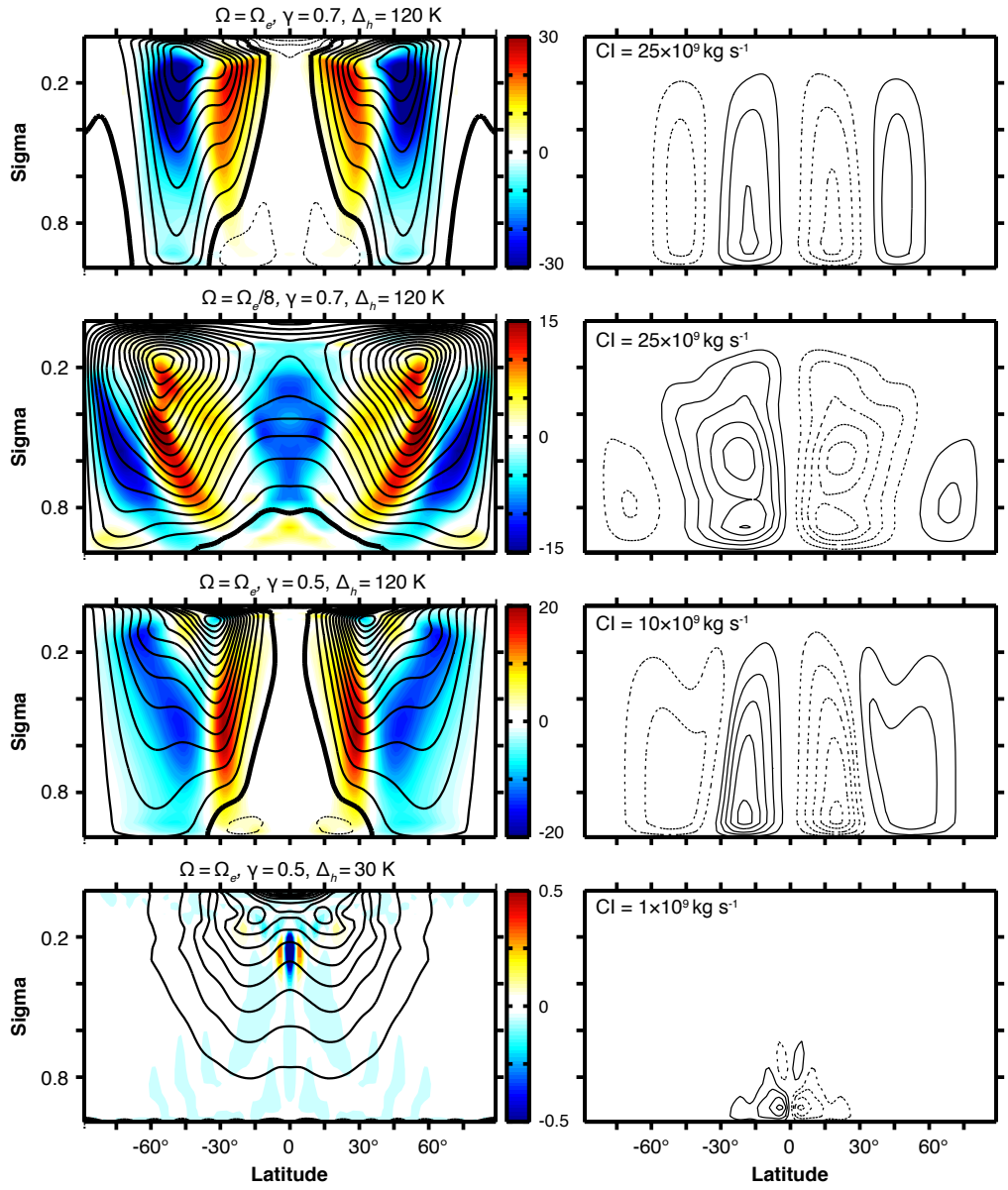

FIG. 1. Left column: Contours of zonal-mean zonal wind (black) and eddy angular momentum flux divergence (colors) in the latitude-sigma plane. The heavy black line is the zero wind contour. The contour interval is 5 m s^{-1} for the zonal wind, and the eddy angular momentum flux divergence is given in units of 10^{-6} m s^{-2}. Right column: Eulerian mean mass flux streamfunction, with contour intervals in the figure panels. Four simulations are shown, with their parameter values indicated in the left column.

For faster planetary rotation rates, the equatorial winds become more westerly with decreasing meridional temperature gradient, Δ_h (compare third and bottom rows in Fig. 1). This is in line with the notion that larger meridional temperature gradients produce stronger baroclinic instability in midlatitudes, leading to off-equatorial wave generation and angular momentum flux divergence near the equator. For slower rotation rates, however, the opposite is true. In these cases, the atmospheres are superrotating at every value of Δ_h we explored, and the superrotation becomes more pronounced for larger Δ_h. So, for a subrotating atmosphere, reducing the meridional tempera-

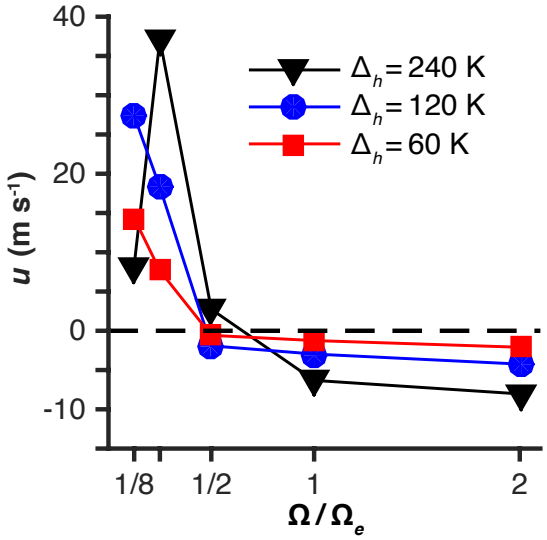

FIG. 2. Upper-tropospheric zonal wind at the equator versus Ω/Ω_e with fixed values of Δ_h and γ. For all three curves, $\gamma = 0.7$.

ture gradient can eventually lead to superrotation. On the other hand, decreasing the meridional temperature gradient when the atmosphere is strongly superrotating (e.g., for a slowly rotating planet) can weaken the superrotation.

b. Relation to wave activity sources

Why do some simulations superrotate while others do not? Quantifying the amount of equatorial eddy angular momentum flux divergence and convergence owing to convective and baroclinic sources provides insight. As stated above, there must be a wave activity source at the equator that produces eddy angular momentum fluxes directed into the equatorial region in order to generate and sustain the angular momentum maximum there. Making the weak temperature gradient approximation near the equator, we write the vorticity equation neglecting the baroclinic term, the twisting-tilting term, and friction:

$$\frac{\partial \zeta_a}{\partial t} + \mathbf{v}_\Psi \cdot \nabla_h \zeta_a \approx -\zeta_a (\nabla_h \cdot \mathbf{v}_\chi) - (\mathbf{v}_\chi \cdot \nabla_h \zeta_a) = R. \quad (2)$$

Here, ζ_a is the absolute vorticity, $\mathbf{v}_\chi + \mathbf{v}_\Psi = \mathbf{v}$ is the horizontal velocity decomposed into its rotational (Ψ) and divergent (χ) components, and ∇_h denotes the horizontal components of the del operator. Following Sardeshmukh and Hoskins (1988) and Schneider and Liu (2009), we define the Rossby wave source as the fluctuating part of the right-hand side of this equation, $R' = R - \bar{R}$, with the overbar denoting a zonal mean and primes deviations therefrom.

The vorticity equation implies the approximate eddy enstrophy equation

$$\frac{1}{2}\frac{\partial \overline{\zeta'^2}}{\partial t} + \overline{v'_\Psi \zeta'} \partial_y \bar{\zeta}_a \approx \overline{R'\zeta'}, \quad (3)$$

where v_Ψ is the rotational component of the meridional velocity v. Advection of eddy vorticity by the eddies themselves (the triple correlation term) is neglected. In a statistically steady state and under the assumption that $\bar{\zeta}_a \neq 0$, the wave activity balance at the equator can then be written as (Andrews and Mcintyre 1976; Andrews and McIntyre 1978; Edmon et al. 1980; Schneider and Liu 2009)

$$G = \frac{\overline{R'\zeta'}}{\partial_y \bar{\zeta}_a} = \overline{v'_\Psi \zeta'} = -\frac{1}{\cos\phi}\partial_y(\overline{u'_\Psi v'_\Psi}\cos^2\phi). \quad (4)$$

The first equality defines G, the generation of wave activity $\overline{\zeta'^2}/(2\partial_y \bar{\zeta}_a)$. Where G is positive, wave activity is generated, and the eddy flux of angular momentum associated with the rotational flow converges; where G is negative, wave activity is dissipated, and the eddy flux of angular momentum associated with the rotational flow diverges. Because the bulk of the eddy flux of angular momentum is associated with the rotational (geostrophic) flow, convergence/divergence of the eddy angular momentum flux $\overline{u'_\Psi v'_\Psi}\cos\phi$ associated with the rotational flow is essentially synonymous with convergence/divergence of the overall eddy angular momentum flux $\overline{u'v'}\cos\phi$.

We will use

$$\langle G_e^+ \rangle = \frac{1}{\Delta\phi}\int_{-5^\circ}^{+5^\circ} \frac{1}{\Delta\sigma}\int_{\sigma_t+\Delta\sigma}^{\sigma_t} G^+ d\sigma\, d\phi, \quad (5)$$

the average of only the positive values G^+ of G in the equatorial upper troposphere, as a measure of the wave activity generation in the equatorial region, and hence as a measure of equatorially generated eddy angular momentum flux convergence, $-(\cos^{-1}\phi)\,\partial_y(\overline{u'v'}\cos^2\phi)_e$. Here the subscript e represents an average over the equatorial region between -5° and $+5^\circ$. Angle brackets $\langle\cdot\rangle$ represent an average over a fixed depth in the upper troposphere, taken from the equatorial tropopause (defined using a critical lapse rate of 2K/km) at the level $\sigma_t = p_t/p_s$ to the level lying $\Delta\sigma = \Delta p/p_s = 0.3$ below it. There is one subrotating simulation ($\Omega = 2\Omega_e, \Delta_h = 120$ K, $\gamma = 0.7$) with negative values of $\langle G_e \rangle$ in the averaging region, such that $\langle G_e^+ \rangle$ is zero. We have omitted this simulation from the figures that follow, because they show logarithms of $\langle G_e \rangle$, which is not a real number for this simulation.

Angular momentum divergence due to wave breaking of midlatitude baroclinic eddies can partially or fully compensate the angular momentum convergence in the equatorial region associated with equatorial wave activity generation $\langle G_e^+ \rangle$. We want to quantify the angular momentum flux divergence $M = (\cos^{-1}\phi)\,\partial_y(\overline{u'v'\cos^2\phi})_x$ (subscript

x for extratropical quantities) these baroclinic eddies generate when they dissipate in the tropics. We use an upper-tropospheric average of the eddy angular momentum flux divergence M in the first "lobe" of divergence nearest to the equator,

$$\langle M_d \rangle = \frac{1}{\Delta\phi} \int_{\phi_2}^{\phi_1} \frac{1}{\Delta\sigma} \int_{\sigma_t+\Delta\sigma}^{\sigma_t} M d\sigma \, d\phi. \tag{6}$$

After vertically averaging over the fixed depth in the upper troposphere, we determine the latitudes bounding the first lobe of divergence for each simulation by starting at the equator and finding the latitude ϕ_1 where $\langle M \rangle$ becomes positive, indicating divergence, then continuing poleward up to the latitude ϕ_2 where $\langle M \rangle$ changes sign to become negative. This average over the divergence lobe closest to the equator is denoted by the subscript d. Divergence in this region is produced when midlatitude baroclinic eddies dissipate there, for example, through filamentation and roll-up in their critical layers (Stewartson 1977; Randel and Held 1991), or through interaction with the mean-flow shear (Farrell 1987; Lindzen 1988; Huang and Robinson 1998; O'Gorman and Schneider 2007; Ait-Chaalal and Schneider 2015). Thus, $\langle M_d \rangle$ provides us with a measure of wave activity dissipation associated with baroclinic waves equatorward of their midlatitude generation regions. However, the measure is imperfect in that some angular momentum flux divergence associated with midlatitude eddies in this region may be compensated by locally generated angular momentum flux convergence, or it may be augmented by divergence associated with equatorial waves.

Figure 3 displays all 59 simulations as a function of $\langle G_e^+ \rangle$ and $\langle M_d \rangle$. The black line is the one-to-one line. The different symbols indicate the planetary rotation rate for each simulation, and the colors of the symbols indicate the magnitude of the equatorial upper-tropospheric zonal wind. Positive values (red) indicate superrotation and negative values (blue) subrotation.

The simulations that lie to the right of the one-to-one line (i.e., with $\langle G_e^+ \rangle > \langle M_d \rangle$) are generally superrotating, and those on the left (i.e., with $\langle G_e^+ \rangle < \langle M_d \rangle$) are generally subrotating, with a couple of exceptions. That is, the ratio of the two parameters $\langle G_e^+ \rangle$ and $\langle M_d \rangle$ captures fairly well whether a given atmosphere is superrotating or not. It is clear that the planetary rotation rate plays a large role in controlling $\langle G_e^+ \rangle$: the slower rotation rates generally lie on the right side (superrotation), and the faster ones on the left (subrotation).

There are two strongly superrotating simulations that lie on the left side of the line, and for which the scalings do not work well in the following figures. These simulations both have $\Delta_h = 30$K and $\gamma = 0.5$. They are the kind of simulations for which we needed to increase the subgrid-scale damping to decrease the noisiness of the simulations (section 2). We found that both the calculation of $\langle G_e^+ \rangle$ and the

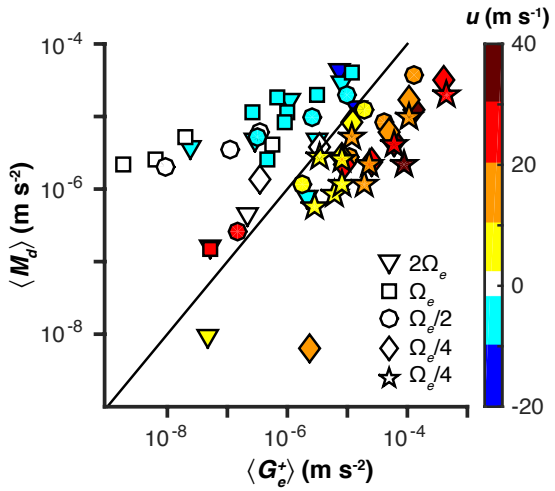

FIG. 3. All simulations shown as a function of $\langle G_e^+ \rangle$ and $\langle M_d \rangle$. In this and subsequent figures, the marker color shows the mean zonal wind averaged within 5 degrees of the equator in the upper troposphere (in the same way that $\langle G_e^+ \rangle$ is averaged). Positive values (red) indicate superrotation and negative values (blue) indicate subrotation. The different symbols indicate the planetary rotation rates shown in the legend. The solid black line is the 1:1 line.

equatorial windspeed in these simulations with such low baroclinicity are very sensitive to the subgrid-scale damping. For example, both simulations were more weakly superrotating in the upper troposphere with weaker damping. That subgrid-scale damping becomes dynamically important and leads to numerical sensitivities may explain why these simulations are inconsistent with the theory.

4. Scaling theory

To understand more completely under which conditions superrotation arises, we develop a scaling theory for the wave activity generation $\langle G_e^+ \rangle$ near the equator and for the off-equatorial eddy angular momentum flux divergence $\langle M_d \rangle$.

a. Equatorial wave activity generation

To determine how $\langle G_e^+ \rangle$ scales with mean-flow parameters, we need scalings for R', ζ', and $\partial_y \bar{\zeta}_a$. Because the Rossby wave source is $R' = R - \bar{R}$ by definition, with $R = \nabla_h \cdot (\zeta_a \mathbf{v}_\chi)$ according to Eq. (2), one can expand

$$\begin{aligned} R' &\approx \nabla_h \cdot \left(\zeta' \bar{\mathbf{v}}_\chi + \bar{\zeta}_a \mathbf{v}'_\chi \right) \\ &\approx \left(\bar{\mathbf{v}}_\chi \cdot \nabla_h \right) \zeta' + \zeta' \left(\nabla_h \cdot \bar{\mathbf{v}}_\chi \right) + \left(\mathbf{v}'_\chi \cdot \nabla_h \right) \bar{\zeta}_a + \bar{\zeta}_a \left(\nabla_h \cdot \mathbf{v}'_\chi \right), \end{aligned} \tag{7}$$

where we assumed that the nonlinear eddy-eddy interaction term $\zeta'\mathbf{v}'_\chi - \overline{\zeta'\mathbf{v}'_\chi}$ is negligible. A priori, the terms on the right-hand side of (7) are all of similar magnitude. We develop a scaling for the last term, the stretching of mean absolute vorticity by divergence fluctuations, which has traditionally been a focus of equatorial wave generation theories. It scales like the mean absolute vorticity $\bar{\zeta}_a$ multiplied by a scaling for the divergence of the fluctuating horizontal flow $\nabla_h \cdot \mathbf{v}'_\chi$. For the mean absolute vorticity, we assume $\bar{\zeta}_a \sim \beta_e L_{\beta_e}$, and for its gradient $\partial_y \bar{\zeta}_a \sim \beta_e$, where $\beta_e = \partial f/\partial y \approx 2\Omega/a$ is the derivative of the Coriolis parameter f near the equator, and L_{β_e} is a length scale for the rotational flow. The latter we will take to be the equatorial Rossby radius

$$L_{\beta_e} \sim \left(\frac{H_e N_e}{\beta_e}\right)^{1/2}, \tag{8}$$

where H_e is the equatorial tropopause height and N_e is the equatorial buoyancy frequency. For the divergence of the fluctuating horizontal flow, we can derive a scaling from the continuity equation combined with the thermodynamic equation under the weak temperature gradient approximation (Sobel et al. 2001; Schneider and Liu 2009)

$$\nabla_h \cdot \mathbf{v}'_\chi \approx -\frac{\partial}{\partial z}\left(\frac{gQ'}{\theta_0 N_e^2}\right) \sim \frac{gQ'}{\theta_0 H_e N_e^2}. \tag{9}$$

This assumes divergence fluctuations are driven primarily by diabatic (i.e., convective) heating fluctuations Q' in the upper troposphere, and the height scale over which the vertical velocity $w \sim gQ'/(\theta_0 N_e^2)$ diverges is proportional to the tropopause height (e.g., $0.1H_e$). Alternative choices for this height scale are possible. For example, one might take it to be constant, or use the scale height $H = RT/g$. The difference between taking the height scale to be constant and using a fraction of H_e is quite small. However, using the scale height H does not fully capture the dependence of the height scale on the stratification in our simulations.

To relate the divergence fluctuations $\nabla_h \cdot \mathbf{v}'_\chi$ to mean-flow quantities, we need to express the diabatic heating fluctuations Q' on the right-hand side of (9) in terms of a mean-flow quantity. We take the diabatic heating fluctuations Q' to scale with the temporal- and zonal-mean convective heating $\bar{Q}$, obtained from the GCM's convection scheme. This captures the heating fluctuations well, except for some simulations with very weak convective heating, where it overestimates the diabatic heating fluctuations (Fig. 4). The resulting scaling (9) of the rms divergence fluctuations in the upper troposphere, averaged in the same way and in the same region as $\langle G_e^+ \rangle$ and using $Q' \sim \bar{Q}$, works well for most of the simulations, particularly the superrotating ones (Fig. 5). It overestimates the divergence for subrotating simulations with very weak equatorial divergence fluctuations.

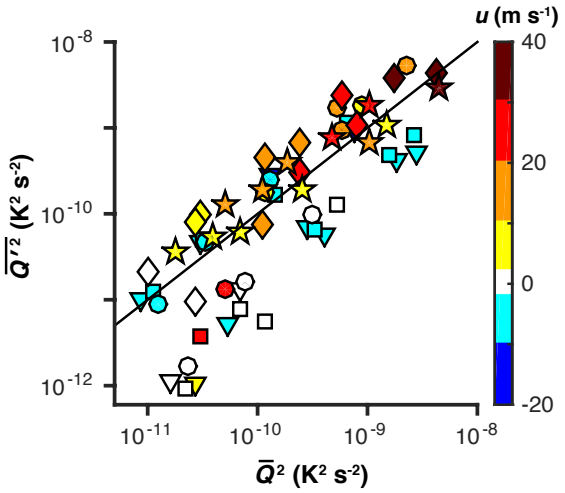

FIG. 4. Convective heating fluctuations versus mean convective heating.

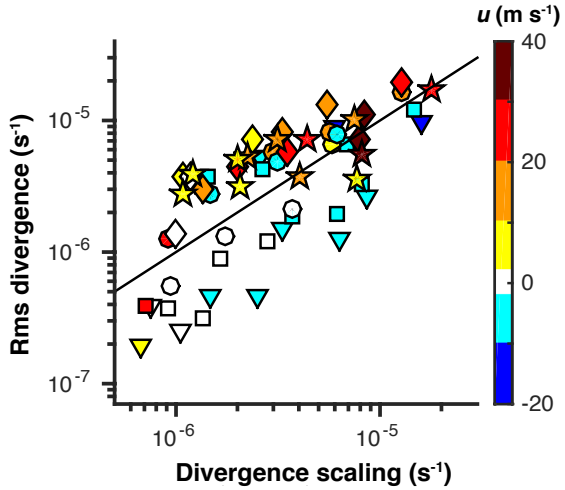

FIG. 5. Root-mean-square equatorial divergence fluctuations $\nabla_h \cdot \mathbf{v}'_\chi$ versus the divergence scaling (9), multiplied by a constant factor 21.9 obtained from a least-squares fit. The solid line is the least-squares fit through the data points.

To obtain a scaling for the wave activity generation, it remains to find a scaling for the enstrophy source $\overline{R'\zeta'}$, given the scaling for the Rossby wave source R'. We found that vorticity fluctuations ζ' scale with the Rossby wave source $R' \sim \bar{\zeta}_a(\nabla_h \cdot \mathbf{v}')$ divided by the inverse time scale

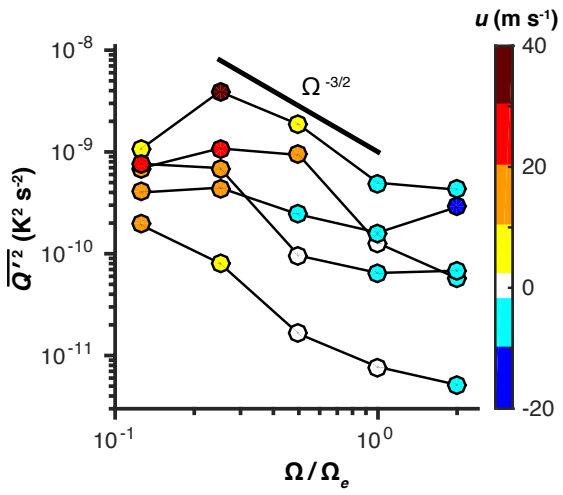

FIG. 6. Variance of convective heating fluctuations Q' versus planetary rotation rate Ω for five series of simulations holding Δ_h and γ constant and varying the rotation rate (each series is connected by a black line).

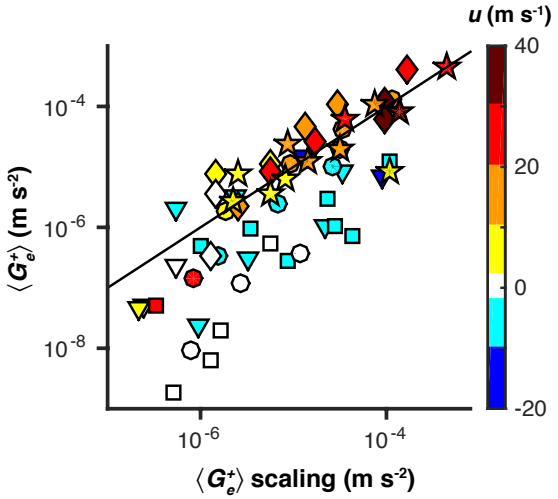

FIG. 7. Equatorial wave activity source $\langle G_e^+ \rangle$ versus the scaling (10), multiplied by a constant factor 89.3 obtained from a least-squares fit. The solid line is the least-squares fit through the data points.

given by the mean vorticity, $\bar{\zeta}_a \sim \beta_e L_{\beta_e}$. When combining the scalings for R' and ζ', one obtains $\zeta' \sim \nabla_h \cdot \mathbf{v}' \sim g\bar{Q}/(\theta_0 H_e N_e^2)$. That is, vorticity fluctuations scale with divergence fluctuations, as might be expected in regimes where the Rossby number is $O(1)$. This implies that the other terms in Eq. (7) scale similarly to the stretching term on which we focused. The similarity of divergence and vorticity fluctuations also seems to imply that ζ' is not dependent on the planetary rotation rate; however, this is not the case. The planetary rotation rate enters the ζ' scaling through the heating rate Q', which decreases with increasing rotation rate, empirically like $Q' \sim \Omega^{-3/4}$ between $\Omega = \Omega_e$ and $\Omega_e/4$ (Fig. 6) in these simulations. For the highest and lowest rotation rates, the dependence of Q' on rotation rate becomes weaker. In general, Fig. 6 shows that simulations with lower planetary rotation rates have stronger mean equatorial heating rates and convective heating rate fluctuations—as is to be expected given that lower planetary rotation rates necessitate weaker temperature gradients and hence stronger mean meridional circulations to transport heat near the equator (Held and Hou 1980). Correspondingly, divergence and vorticity fluctuations generally strengthen as the rotation rate decreases.

Putting this all together we have a scaling for the equatorial wave activity source $\langle G_e^+ \rangle$:

$$\begin{aligned} \langle G_e^+ \rangle &\sim L_{\beta_e} (\nabla_h \cdot \mathbf{v}')^2 \\ &\sim \frac{g^2 \bar{Q}^2}{\theta_0^2 H_e^{3/2} N_e^{7/2} \beta_e^{1/2}}. \end{aligned} \tag{10}$$

Figure 7 shows $\langle G_e^+ \rangle$ versus the scaling (10), with the right-hand side multiplied by a factor 89.3, obtained from a least-squares fit. This factor is quite large because we have suppressed an explicit small factor multiplying the tropopause height H_e in the height scale (e.g., $0.1H_e$) of vertical velocity divergence in Eq. (9), which would enter the scaling (10) as an inverse square (e.g., as 0.1^{-2}). Generally, the scaling captures the variations of the wave activity source over $\sim$3 orders of magnitude quite well. The most significant departures from a one-to-one relationship occur for subrotating simulations with weak pole-to-equator temperature gradients, for which the scaling overestimates $\langle G_e^+ \rangle$, in similar ways as the divergence scaling (9) overestimates actual divergence fluctuations (cf. Fig. 5).

b. Baroclinic angular momentum flux divergence

The baroclinic angular momentum fluxes originating in the extratropics strengthen with increasing baroclinicity, for example, increasing pole-to-equator temperature contrasts or decreasing static stability. Schneider and Walker

(2008) showed that in simulations of dry atmospheres similar to ours, the eddy angular momentum flux divergence scales with the mean available potential energy (MAPE) per unit mass in the troposphere and inversely with the width $L_{\rm bc}$ of the baroclinic zone over which MAPE is calculated:

$$\langle M_d \rangle \sim \frac{\rm MAPE}{L_{\rm bc}}. \tag{11}$$

Here, MAPE per unit mass is approximately

$$\rm MAPE \approx \frac{g^2}{24 N_x^2} \left(\frac{\Delta\theta}{\theta_0} \right)^2, \tag{12}$$

where $\Delta\theta$ is the meridional potential temperature contrast across a baroclinic zone, θ_0 is a reference value of near-surface potential temperature, and N_x is the extratropical buoyancy frequency (Schneider 1981; Schneider and Walker 2008). For simplicity we have omitted the dependence of MAPE on the supercriticality S_c, which was discussed by Schneider and Walker (2008). Including it changes the scaling only marginally for the simulations we consider here. The width of the baroclinic zone only varies by a factor of two in our simulations, because the width of this zone is limited by the size of the planet for simulations with low planetary rotation rate like the ones studied here. Hence, here we use a constant length scale $L_{\rm bc} = \pi a/4$, but for faster rotation rates it would need to be reduced, for example, like the Rossby radius, $L_{\rm bc} \sim L_R \sim \Omega^{-1}$. Combining these estimates and omitting nondimensional factors gives

$$\langle M_d \rangle \sim \frac{g^2}{L_{\rm bc} N_x^2} \left(\frac{\Delta\theta}{\theta_0} \right)^2. \tag{13}$$

This scaling captures the dependence of the baroclinic eddy angular momentum flux divergence in most simulations reasonably well, except in some very weakly baroclinic simulations, in which it overestimates $\langle M_d \rangle$ (Fig. 8). A least-squares fit suggests the right-hand side needs to be multiplied by 0.174 to give a good fit to the simulation results.

Combing the estimate for the equatorial wave activity generation (angular momentum flux convergence) with that for the baroclinic angular momentum flux divergence, we can introduce a nondimensional number

$$\begin{aligned} S_r &= \frac{\langle G_e^+ \rangle}{\langle M_d \rangle} \\ &\sim \alpha \frac{L_{\rm bc} N_x^2}{(H_e^3 N_e^3 \beta_e)^{1/2}} \left(\frac{\bar{Q}}{N_e \Delta\theta} \right)^2. \end{aligned} \tag{14}$$

The factor $\alpha \approx 500$ is the ratio of the nondimensional factors in the scalings for $\langle G_e^+ \rangle$ and $\langle M_d \rangle$. (Again, this factor α is large primarily because we suppressed an explicit small factor multiplying the tropopause height H_e in the in the height scale of vertical velocity divergence.) The

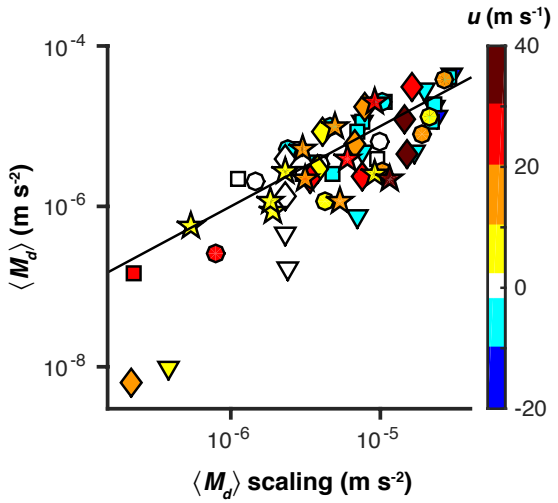

FIG. 8. Eddy angular momentum flux divergence $\langle M_d \rangle$ versus the scaling (13), multiplied by a constant factor 0.174 obtained from a least-squares fit. The solid line is the least-squares fit through the data points.

nondimensional quantity S_r quantifies an atmosphere's propensity for superrotation in terms of mean-flow quantities. When $S_r \gtrsim 1$, an atmosphere will usually superrotate, and when $S_r \lesssim 1$ it will usually subrotate. It tells us that atmospheric superrotation is favored for stronger convective heating at the equator ($\bar{Q}$), reduced meridional temperature gradients ($\Delta\theta$), lower planetary rotation rates ($\beta_e \sim \Omega$), and weaker equatorial (N_e) or stronger extratropical (N_x) static stability. Because the convective heating generally strengthens with decreasing rotation rate, the dependence of S_r on Ω is stronger than that occurring explicitly through the $\beta_e^{-1/2}$ term.

5. Discussion

a. Mechanisms and origin of parameter dependences

Although idealized, the simulations performed here have the basic ingredients to produce superrotation in terrestrial atmospheres. The most important quantities controlling whether superrotation occurs or not in our simulations are the planetary rotation rate and the meridional temperature gradient, with, for example, the static stability in the tropics and extratropics playing secondary roles.

The dependence of S_r on rotation rate comes primarily from the equatorial wave activity generation $\langle G_e^+ \rangle$. The extratropical $\langle M_d \rangle$ will depend on rotation rate for faster rotation rates ($\langle M_d \rangle \sim \Omega$) because the width of the baroclinic zone $L_{\rm bc}$ depends on rotation rate like the Rossby radius, $L_R \sim \Omega^{-1}$. For the simulations discussed here,

however, the planetary scale limits this rotation rate dependence. The equatorial $\langle G_e^+ \rangle \sim L_{\beta_e} (\nabla_h \cdot \mathbf{v}')^2$ decreases with rotation rate for two primary reasons: The mean-square divergence $(\nabla_h \cdot \mathbf{v}'_\chi)^2 \sim \bar{Q}^2$ depends on rotation rate because the squared diabatic heating rate does, roughly like $\sim \Omega^{-3/2}$ in our simulations. Additionally, the equatorial Rossby radius depends on rotation rate, $L_{\beta_e} \sim \Omega^{-1/2}$.

Thus, for faster rotation rates, the baroclinic eddy angular momentum flux divergence increases with rotation rate because eddies get smaller and the angular momentum fluxes become more concentrated in narrower baroclinic zones. Increases in meridional temperature contrasts because of reduced efficiency of poleward energy transport counteract some of this increase in baroclinic eddy angular momentum flux divergence (Schneider and Walker 2008). By contrast, the equatorial wave activity generation decreases with rotation rate both because the equatorial Rossby radius increases and the convective heating fluctuations and divergence fluctuations weaken. For our simulations, the equatorial wave activity generation effect dominates and leads to $S_r \sim \Omega^{-2}$, that is, a strongly increasing propensity for superrotation with decreasing rotation rate. (For faster rotation rates, this amplifies to $S_r \sim \Omega^{-3}$ when additionally the shrinking width of the baroclinic zone is taken into account.) This may account for the fact that slowly rotating terrestrial atmospheres (e.g., Venus') tend to exhibit superrotation.

The dependence of S_r on the meridional temperature contrast $\Delta\theta$ enters explicitly only through the scaling for $\langle M_d \rangle$, which depends on MAPE $\sim (\Delta\theta)^2$, yielding $S_r \sim (\Delta\theta)^{-2}$. Thus, when meridional temperature gradients are weak, there is less angular momentum flux divergence near the equator by midlatitude baroclinic eddies, and the propensity for superrotation increases. It is worthwhile noting that when $\Delta\theta$ is decreased in our simulations, the polar temperature remains constant and the equatorial and globally-averaged temperature decrease, decreasing the equatorial tropopause height H_e (Thuburn and Craig 2000; Schneider 2004) and adding to the propensity for superrotation. The meridional temperature contrast and the rotation rate may also both affect the static stability in the extratropics and near the equator, which in themselves have opposing effects on $S_r \sim N_x^2 N_e^{-7/2}$.

To look at the equatorial wave structure more closely, Fig. 9 shows the correlation coefficient between equatorial divergence fluctuations at a reference point and horizontal streamfunction fluctuations at 300 hPa for a superrotating simulation with slow planetary rotation ($\Omega = \Omega_e/8$, $\Delta_h = 120$ K, $\gamma = 0.7$; see second row of Fig. 1). The reference point is indicated by a black dot at the equator at 180° longitude. The correlation coefficients between divergence fluctuations at the equator and, on the one hand, horizontal streamfunction fluctuations (colors) and, on the other hand, wind fluctuations (arrows), indicate a Rossby (rotational) wave structure (Matsuno 1966).

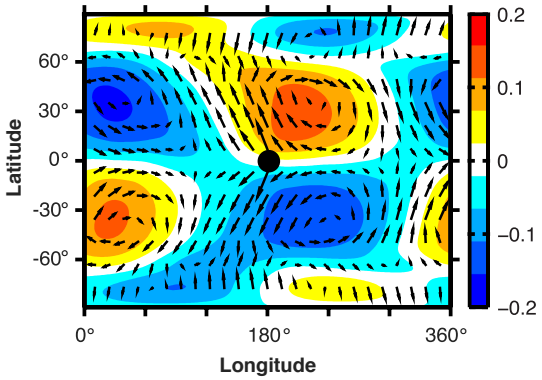

FIG. 9. Correlation coefficient (colors) between divergence fluctuations at a reference point on the equator (black dot) and horizontal streamfunction fluctuations at 300 hPa, for the superrotating simulation with $\Omega = \Omega_e/8$, $\Delta_h = 120$ K, and $\gamma = 0.7$ (see second row of Fig. 1). Arrows represent correlation coefficients between wind fluctuations and divergence fluctuations at the equator. An arrow pointing right corresponds to a positive correlation for u' and zero correlation for v'; an arrow pointing upward corresponds to a positive correlation of for v' and zero for u'. The lengths of the arrows indicate the magnitude of the correlations.

The Rossby wave has zonal velocities symmetric about the equator and meridional velocities antisymmetric about the equator. The equatorial Rossby radius, which determines the decay of meridional velocity correlations away from the equator, appears to extend over much of a hemisphere, consistent with the low rotation rate in this simulation ($\Omega = \Omega_e/8$). The correlations between wind fluctuations and divergence fluctuations at the equator (arrows) indicate angular momentum transport toward the equator. They also show that no more than the usual tilt of phase lines with latitude is needed to generate the angular momentum transport; it is not necessary to see outright meridional propagation of wave packets for angular momentum transport to occur. This overall picture is consistent with our theoretical considerations, which assign primary importance to equatorial Rossby waves and their equatorward angular momentum transport in the generation of superrotation.

Figure 10 shows the eddy angular momentum flux cospectra (black contours for positive and blue contours for negative fluxes) versus latitude at the level $\sigma = 0.3$ for a subrotating and a superrotating simulation (corresponding to the first and second rows of Fig. 1). The thick black line is the mean zonal wind at the same level. The subrotating simulation shows similar features to what we see on Earth (Randel and Held 1991): baroclinic eddies generated in midlatitudes have phase speeds of $O(10\ \mathrm{m\ s^{-1}})$ and dissipate near their critical latitudes, which produces convergence of eddy angular momentum fluxes in midlatitudes and divergence primarily on the equatorward flanks

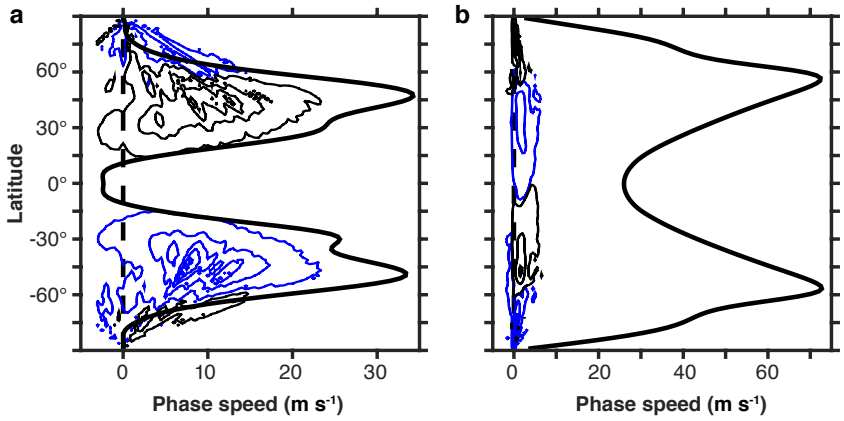

FIG. 10. Eddy angular momentum flux cospectra versus latitude at $\sigma = 0.3$ for (a) a subrotating simulation ($\Omega = \Omega_e$, $\Delta_h = 120$ K, $\gamma = 0.7$, see first row of Fig. 1) and (b) the same superrotating simulation as in Fig. 9 ($\Omega = \Omega_e/8$, $\Delta_h = 120$ K, $\gamma = 0.7$, see second row of Fig. 1). Black and blue contours correspond to positive and negative angular momentum fluxes, respectively, and the thick black line shows the mean zonal wind at the same level.

of the jets. For the superrotating simulation, we see something different: Eddies have phase speeds of $O(1\ \mathrm{m\ s^{-1}})$ (i.e., they are more strongly westward relative to the mean flow); their associated angular momentum fluxes converge near the equator. The eddies do not seem to dissipate near their critical latitudes but instead produce angular momentum flux convergence near the equator through interaction with the mean-flow shear, consistent with the tilted phase lines seen in Fig. 9 (e.g., Farrell 1987; Lindzen 1988; Huang and Robinson 1998; O'Gorman and Schneider 2007; Ait-Chaalal and Schneider 2015).

b. Relation to prior work

Our scaling theory and simulation results are consistent with previous simulations of superrotating terrestrial atmospheres. The scaling theory provides a unifying framework within which the generation of superrotation, for example, in slowly rotating (e.g., Del Genio et al. 1993; Del Genio and Zhou 1996; Walker and Schneider 2006) or strongly convective (e.g., Schneider and Liu 2009; Caballero and Huber 2010; Liu and Schneider 2011) atmospheres can be interpreted as arising from a common set of principles. It provides a quantitative criterion to determine when superrotation occurs, which is more generally applicable than previous criteria.

For example, Mitchell and Vallis (2010) and Potter et al. (2014) argued that terrestrial atmospheres transition from subrotation to superrotation when the thermal Rossby number

$$\mathrm{Ro}_T = \frac{R_a \Delta_h}{(2\Omega a)^2} \tag{15}$$

exceeds 1 (gas constant of air R_a, pole-equator temperature contrast in radiative equilibrium Δ_h, and planetary radius a). The mechanism for generation of superrotation at large thermal Rossby numbers is posited to be the development of a global-scale baroclinic disturbance (Mitchell and Vallis 2010), possibly involving Kelvin waves (Potter et al. 2014). Among other differences between our models, the main distinction is that we use one in which the radiative equilibrium is statically unstable and that employs a convection scheme to provide vertical heat transport. Mitchell and Vallis (2010) and Potter et al. (2014), by contrast, use a model with a statically stable radiative equilibrium. However, given that our arguments merely require the presence of divergence fluctuations to generate Rossby waves, irrespective of how the divergence fluctuations are created, this distinction between the models may not be essential: even the model with a statically stable radiative equilibrium has preferential tropospheric heating and a divergent circulation in low latitudes, which likely fluctuates, with divergence fluctuations that may scale with the mean diabatic heating rate and that can generate Rossby waves, in essentially the same way we described.

To compare how well the thermal Rossby number Ro_T captures when superrotation occurs, Fig. 11a shows the equatorial wind speed in the upper troposphere versus Ro_T for all of our simulations. The symbols indicate the planetary rotation rate (as in Fig. 3), and the colors indicate

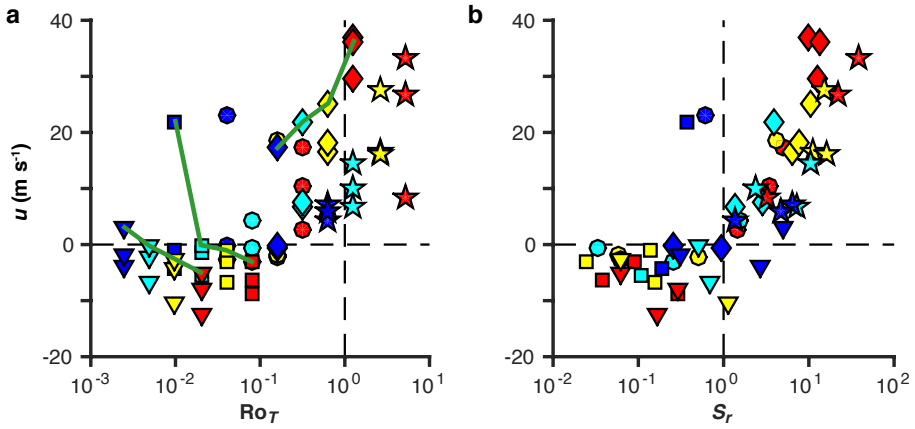

FIG. 11. Equatorial zonal wind in the upper troposphere versus (a) the thermal Rossby number $\mathrm{Ro}_T = R_a \Delta_h / (2a\Omega)^2$ and (b) $S_r = \langle G_e^+ \rangle / \langle M_d \rangle$. Symbols are as in Fig. 3. Colors represent the value of Δ_h (blue = 30 K, cyan = 60 K, yellow = 120 K, red = 240 K). Simulations that lie above the horizontal dashed line ($u = 0$) are superrotating. The vertical dashed lines indicates where $\mathrm{Ro}_T = 1$ or $S_r = 1$.

the value of Δ_h, with blue representing low values and red high values. Simulations with high Ro_T do tend to be superrotating, but there is no clear threshold for superrotation. The same holds when we use the same diagnostic for superrotation (vertical mean of zonal wind) as in Mitchell and Vallis (2010) and Potter et al. (2014). Additionally, there are numerous simulations that have low Ro_T, yet are superrotating.

Simulations in three series are connected with thick green lines in Fig. 11a. These simulations have the same value of γ and Ω, and the dots along each green line show what happens as Δ_h is varied alone. For the simulations that are subrotating, decreasing the pole-equator temperature contrast (and so decreasing Ro_T by definition) can lead to superrotation, as shown by two of the connected series of simulations in Fig. 11a and as seen in Fig. 1 (compare rows 3 and 4). This behavior is in line with the theory presented in this paper, that decreasing baroclinicity in midlatitudes while holding other parameters constant will increase S_r and eventually lead to superrotation. However, it runs counter to the notion that the thermal Rossby number alone would generally predict when superrotation occurs. For strongly superrotating simulations, decreasing Δ_h has the opposite effect: it weakens the superrotation, as shown by the connected simulations near the top right of Fig. 11. This is more in line with the notion that the thermal Rossby number predicts when superrotation occurs.

The nondimensional number S_r developed here diagnoses more generally whether or not an atmosphere will be super- or subrotating. It shows a clearer threshold for superrotation at $S_r = 1$, with only the two very weakly baroclinic simulations discussed in section 3b deviating from the expected behavior (Fig. 11b). However, S_r does not provide any information on how strong or weak any superrotation will be. For example, as mentioned previously and as shown in Fig. 11, increasing S_r beyond $S_r \sim 1$ by decreasing Δ_h actually weakens the superrotation. Scaling arguments relating the strength of superrotating jets to their widths and to the static stability in the equatorial region were provided and tested in Liu and Schneider (2010) and Liu and Schneider (2011).

c. *Limitations and possible extensions*

Our simulations and scaling theory ignored several factors that are known to affect whether superrotation occurs. For example, we ignored the seasonal cycle. Yet the seasonal cycle decelerates the zonal wind in the equatorial upper troposphere in the annual mean, because a Hadley circulation whose ascending branch is displaced off the equator is associated with equatorial easterlies (e.g., Lindzen and Hou 1988; Lee 1999; Kraucunas and Hartmann 2005; Mitchell et al. 2014). This disfavors superrotation for planets with nonzero obliquities. Additionally, the convective wave activity generation G in the presence of a seasonal cycle would be maximal off the equator for part of the year, decreasing the numerator of S_r and likewise disfavoring superrotation. A more general scaling theory should take into account the seasonal cycle, as well as the vertical advection of angular momentum, which becomes important seasonally (Shell and Held 2004; Kraucunas and Hartmann 2005).

We also focused on transient sources of equatorial Rossby waves at the expense of stationary sources, which in several previous studies have been shown to be able to generate superrotation if they are strong enough (e.g., Suarez and Duffy 1992; Saravanan 1993; Joshi et al. 1997; Kraucunas and Hartmann 2005; Merlis and Schneider 2010; Arnold et al. 2012; Pierrehumbert 2011). Our scaling theory can be extended to take stationary equatorial wave activity generation into account, by considering how the stationary divergence perturbation and equatorial wave activity generation scale with parameters controlling the strength of the stationary wave source. In particular, it is to be expected that the importance of equatorial wave activity generation owing to stationary heat sources increases in importance relative to baroclinic eddy angular momentum flux divergence as the planetary rotation rate decreases for the same reasons the importance of transient equatorial wave activity generation increases. Thus, we expect that stationary heat sources (e.g., stellar heating focused on a substellar point on tidally locked planets) more easily lead to equatorial superrotation on slowly rotating planets.

6. Conclusions

We have presented simulations and a scaling theory that establish conditions under which superrotation occurs in terrestrial atmospheres. By varying the planetary rotation rate, the pole-equator temperature contrast in radiative equilibrium, and a scaling parameter for the convective lapse rate, we generated a wide range of atmospheric flows, some superrotating and some subrotating.

The theory presented here is based on a simple idea going back to Saravanan (1993) about two competing sources for eddy angular momentum flux convergence at the equator. The first is a source at the equator: Rossby waves generated by convective heating fluctuations. As these waves dissipate away from the equator, they converge angular momentum into the equatorial region, increasing the propensity for superrotation. The other source is baroclinic instability in midlatitudes, which generates Rossby waves in midlatitudes that dissipate farther equatorward, thus extracting momentum from lower latitudes. This mechanism decreases the propensity for superrotation. Quantifying the magnitude of the two mechanisms, introducing their nondimensional ratio S_r, and developing a scaling for it in terms of mean-flow quantities leads to our theory and sheds light on the conditions under which superrotation occurs. Our simulation results and scaling theory show that:

1. Superrotation occurs when the eddy angular momentum flux convergence associated with equatorial wave activity generation exceeds eddy angular momentum flux divergence near the equator produced by midlatitude baroclinic eddies (i.e., $S_r \gtrsim 1$).
2. Superrotation is favored for low planetary rotation rates and/or strong diabatic heating.
3. Superrotation is favored when midlatitude baroclinicity is weak.

Our simulations confirm that superrotation is preferred for slowly rotating planets like Venus and Titan, a result that was obtained by Del Genio et al. (1993) and Del Genio and Zhou (1996) in a similar set of simulations. The scaling arguments presented here help us understand why slowly rotating planets exhibit superrotation. In our simulations, equatorial convective heating fluctuations strengthen with decreasing rotation rate, generating waves that transport momentum upgradient toward the equator, leading to superrotation. Such convective heating fluctuations may play a role on Venus, in the shallow convective layers observed in the upper troposphere (Markiewicz et al. 2007). The equatorial wave activity generation strengthens as the planetary rotation rate decreases primarily because the diabatic heating rate strengthens. Thus, similar arguments may also apply for other mechanisms that increase the diabatic heating or more generally, divergence fluctuations at the equator. For example, stationary or nearly stationary heat sources that generate equatorial Rossby waves have been suggested to play a role on Venus near the subsolar point (Gierasch et al. 1997).

Strengthening equatorial convective heating fluctuations may also explain why some Earth climate models exhibit a transition to superrotation under extreme global warming (e.g., Caballero and Huber 2010). In this scenario, convective heating at the equator strengthens due to greenhouse gas forcing, and meridional temperature gradients decrease because of polar amplification of the warming. Both factors favor superrotation.

Acknowledgments. Some of the scaling results in this paper were presented at the 18th Conference on Atmospheric and Oceanic Fluid Dynamics in 2011. The research was supported by the U.S. National Science Foundation through Grant AGS-1049201 and a Graduate Research Fellowship.

References

Ait-Chaalal, F., and T. Schneider, 2015: Why eddy momentum fluxes are concentrated in the upper troposphere. *J. Atmos. Sci.*, **72**, 1585–1604.

Andrews, D. G., and M. E. Mcintyre, 1976: Planetary waves in horizontal and vertical shear: the generalized Eliassen-Palm relation and the mean zonal acceleration. *J. Atmos. Sci.*, **33**, 2031–2048.

Andrews, D. G., and M. E. McIntyre, 1978: An exact theory of nonlinear waves on a Lagrangian-mean flow. *J. Fluid Mech.*, **89**, 609–646.

Arnold, N. P., E. Tziperman, and B. Farrell, 2012: Abrupt transition to strong superrotation driven by equatorial wave resonance in an idealized GCM. *J. Atmos. Sci.*, **69**, 626–640.

Caballero, R., and M. Huber, 2010: Spontaneous transition to superrotation in warm climates simulated by CAM3. *Geophys. Res. Lett.*, **37**, doi:10.1029/2010GL043468.

Charney, J. G., 1963: A note on large-scale motions in the tropics. *J. Atmos. Sci.*, **20**, 607–609.

Del Genio, A. D., and W. Zhou, 1996: Simulations of superrotation on slowly rotating planets: Sensitivity to rotation and initial condition. *Icarus*, **120**, 332–343.

Del Genio, A. D., W. Zhou, and T. P. Eichler, 1993: Equatorial superrotation in a slowly rotating GCM: Implications for Titan and Venus. *Icarus*, **101**, 1–17.

Edmon, H. J., Jr., B. J. Hoskins, and M. E. McIntyre, 1980: Eliassen-Palm cross sections for the troposphere. *J. Atmos. Sci.*, **37**, 2600–2616.

Farrell, B., 1987: Developing disturbances in shear. *J. Atmos. Sci.*, **44**, 2191–2199.

Garner, S. T., D. M. W. Frierson, I. M. Held, O. Pauluis, and G. K. Vallis, 2007: Resolving convection in a global hypohydrostatic model. *J. Atmos. Sci.*, **64**, 2061–2075.

Gierasch, P., and Coauthors, 1997: The general circulation of the Venus atmosphere: An assessment. *Venus II: Geology, Geophysics, Atmosphere, and Solar Wind Environment*, S. W. Bougher, D. M. Hunten, and R. J. Phillips, Eds., The University of Arizona Press, 459–500.

Held, I. M., 1975: Momentum transport by quasi-geostrophic eddies. *J. Atmos. Sci.*, **32**, 1494–1497.

Held, I. M., 1999: Equatorial superrotation in Earth-like atmospheric models, Bernhard Haurwitz Memorial Lecture, American Meteorological Society. Available at www.gfdl.noaa.gov/˜ih.

Held, I. M., and A. Y. Hou, 1980: Nonlinear axially symmetric circulations in a nearly inviscid atmosphere. *J. Atmos. Sci.*, **37**, 515–533.

Hide, R., 1969: Dynamics of the atmospheres of the major planets with an appendix on the viscous boundary layer at the rigid bounding surface of an electrically-conducting rotating fluid in the presence of a magnetic field. *J. Atmos. Sci.*, **26**, 841–853.

Huang, H.-P., and W. A. Robinson, 1998: Two-dimensional turbulence and persistent zonal jets in a global barotropic model. *J. Atmos. Sci.*, **55**, 611–632.

Joshi, M., R. Haberle, and R. Reynolds, 1997: Simulations of the atmospheres of synchronously rotating terrestrial planets orbiting M dwarfs: conditions for atmospheric collapse and the implications for habitability. *Icarus*, **129**, 450–465.

Kostiuk, T., K. E. Fast, T. A. Livengood, T. Hewagama, J. J. Goldstein, F. Espenak, and D. Buhl, 2001: Direct measurement of winds on Titan. *Geophys. Res. Lett.*, **28**, 2361–2364.

Kraucunas, I., and D. L. Hartmann, 2005: Equatorial superrotation and the factors controlling the zonal-mean zonal winds in the tropical upper troposphere. *J. Atmos. Sci.*, **62**, 371–389.

Kuang, Z., P. N. Blossey, and C. S. Bretherton, 2005: A new approach for 3D cloud-resolving simulations of large-scale atmospheric circulation. *Geophys. Res. Lett.*, **32**, L02 809, doi:10.1029/2004GL021024.

Lee, S., 1999: Why are the climatological zonal winds easterly in the equatorial upper troposphere? *J. Atmos. Sci.*, **56**, 1353–1363.

Lindzen, R. S., 1988: Instability of plane parallel shear flow (toward a mechanistic picture of how it works). *Pure Appl. Geophys.*, **126**, 103–121.

Lindzen, R. S., and A. Y. Hou, 1988: Hadley circulations for zonally averaged heating centered off the equator. *J. Atmos. Sci.*, **45**, 2416–2427.

Liu, J., and T. Schneider, 2010: Mechanisms of jet formation on the giant planets. *J. Atmos. Sci.*, **67**, 3652–3672, doi:10.1175/2010JAS3492.1.

Liu, J., and T. Schneider, 2011: Convective generation of equatorial superrotation in planetary atmospheres. *J. Atmos. Sci.*, **68**, 2742–2756, doi:10.1175/JAS-D-10-05013.1.

Markiewicz, W. J., and Coauthors, 2007: Morphology and dynamics of the upper cloud layer of Venus. *Nature*, **450**, 633–636.

Matsuno, T., 1966: Quasi-geostrophic motions in the equatorial area. *J. Meteor. Soc. Japan*, **44**, 25–42.

Merlis, T. M., and T. Schneider, 2010: Atmospheric dynamics of Earth-like tidally locked aquaplanets. *J. Adv. Mod. Earth Sys.*, **2**, 13, doi:10.3894/JAMES.2010.2.13.

Mitchell, J. L., and G. K. Vallis, 2010: The transition to superrotation in terrestrial atmospheres. *J. Geophys. Res.*, **115**, E12 008, doi:10.1029/2010JE003587.

Mitchell, J. L., G. K. Vallis, and S. F. Potter, 2014: Effects of the seasonal cycle on superrotation in planetary atmospheres. *Astrophys. J.*, **787**, 23, doi:10.1088/0004-637X/787/1/23.

O'Gorman, P. A., and T. Schneider, 2007: Recovery of atmospheric flow statistics in a general circulation model without nonlinear eddy–eddy interactions. *Geophys. Res. Lett.*, **34**, L22 801.

Pierrehumbert, R. T., 2011: A palette of climates for Gliese 581g. *Astrophys. J. Lett.*, **726**, L8.

Pinto, J. R. D., and J. L. Mitchell, 2014: Atmospheric superrotation in an idealized GCM: Parameter dependence of the eddy response. *Icarus*, **238**, 93–109.

Porco, C. C., and Coauthors, 2003: Cassini imaging of Jupiter's atmosphere, satellites, and rings. *Science*, **299**, 1541–1547.

Potter, S. F., G. K. Vallis, and J. L. Mitchell, 2014: Spontaneous superrotation and the role of Kelvin waves in an idealized dry GCM. *J. Atmos. Sci.*, **71**, 596–614.

Randel, W. J., and I. M. Held, 1991: Phase speed spectra of transient eddy fluxes and critical layer absorption. *J. Atmos. Sci.*, **48**, 688–697.

Sánchez-Lavega, A., R. Hueso, and S. Pérez-Hoyos, 2007: The three-dimensional structure of Saturn's equatorial jet at cloud level. *Icarus*, **187**, 510–519.

Saravanan, R., 1993: Equatorial superrotation and maintenance of the general circulation in two-level models. *J. Atmos. Sci.*, **50**, 1211–1227.

Sardeshmukh, P. D., and B. J. Hoskins, 1988: The generation of global rotational flow by steady idealized tropical divergence. *J. Atmos. Sci.*, **7**, 1228–1251.

Schneider, E. K., 1981: On the amplitudes reached by baroclinically unstable disturbances. *J. Atmos. Sci.*, **38**, 2142–2149.

Schneider, T., 2004: The tropopause and the thermal stratification in the extratropics of a dry atmosphere. *J. Atmos. Sci.*, **61**, 1317–1340, doi:10.1175/1520-0469(2004)061⟨1317:TTATTS⟩2.0.CO;2.

Schneider, T., 2006: The General Circulation of the Atmosphere. *Annual Review of Earth and Planetary Sciences*, **34**, 655–688, doi: 10.1146/annurev.earth.34.031405.125144.

Schneider, T., and J. Liu, 2009: Formation of jets and equatorial superrotation on Jupiter. *J. Atmos. Sci.*, **66**, 579–601, doi:10.1175/2008JAS2798.1.

Schneider, T., and C. C. Walker, 2006: Self-organization of atmospheric macroturbulence into critical states of weak nonlinear eddy–eddy interactions. *J. Atmos. Sci.*, **63**, 1569–1586, doi:10.1175/JAS3699.1.

Schneider, T., and C. C. Walker, 2008: Scaling laws and regime transitions of macroturbulence in dry atmospheres. *J. Atmos. Sci.*, **65**, 2153–2173, doi:10.1175/2007JAS2616.1.

Schubert, G., 1983: General circulation and the dynamical state of the Venus atmosphere. *Venus*, **1**, 681–765.

Shell, K. M., and I. M. Held, 2004: Abrupt transition to strong superrotation in an axisymmetric model of the upper troposphere. *J. Atmos. Sci.*, **61 (23)**, 2928–2935.

Smith, K., G. Boccaletti, C. Henning, I. Marinov, C. Tam, I. Held, and G. Vallis, 2002: Turbulent diffusion in the geostrophic inverse cascade. *J. Fluid Mech.*, **469**, 13–48.

Sobel, A. H., J. Nilsson, and L. M. Polvani, 2001: The weak temperature gradient approximation and balanced tropical moisture waves. *J. Atmos. Sci.*, **58**, 3650–3665.

Stewartson, K., 1977: The evolution of the critical layer of a Rossby wave. *Geophys. Astrophys. Fluid Dyn.*, **9**, 185–200.

Suarez, M. J., and D. G. Duffy, 1992: Terrestrial superrotation: A bifurcation of the general circulation. *J. Atmos. Sci.*, **49**, 1541–1554.

Thuburn, J., and G. C. Craig, 2000: Stratospheric influence on tropopause height: The radiative constraint. *J. Atmos. Sci.*, **57**, 17–28.

Walker, C. C., and T. Schneider, 2006: Eddy influences on hadley circulations: Simulations with an idealized gcm. *J. Atmos. Sci.*, **63**, 3333–3350, doi:10.1175/JAS3821.1.

Wang, P., and J. L. Mitchell, 2014: Planetary ageostrophic instability leads to superrotation. *Geophys. Res. Lett.*, **41 (12)**, 4118–4126.

Williams, G. P., 2003: Barotropic instability and equatorial superrotation. *J. Atmos. Sci.*, **60 (17)**, 2136–2152.

Yamamoto, M., and M. Takahashi, 2006: Superrotation maintained by meridional circulation and waves in a Venus-like AGCM. *J. Atmos. Sci.*, **63**, 3296–3314, doi:10.1175/JAS3859.1.

Chapter 4

Symmetry breaking of precipitation patterns in a zonally symmetric idealized monsoon

4.1 Introduction

Monsoonal circulations, such as the African, Asian and North American monsoons in the northern hemisphere (NH) summer, and the Australian and South American monsoons in the southern hemisphere (SH) summer, are important climatological features of the summertime circulation, bringing precipitation to regions that suffer from arid conditions during the winter months. For this reason, the socioeconomic impacts of the monsoon rainfall are quite large, especially since many of the regions affected are densely populated. While all monsoons are linked to the seasonal migration of convergence zones over subtropical continents and share similar large scale features, they differ in important ways that depend on their location, regional topography and continental configuration. Land-sea contrast has been deemed not essential for the generation of monsoons (e.g., Bordoni and Schneider 2008), but the spatial distribution of land certainly affects the spatial and temporal distribution of precipitation. Hence a fundamental and quantitative understanding of these systems requires consideration of regional differences in, for example, continental configuration.

Monsoons are characterized by alternating wet and dry seasons and seasonally reversing winds. Because of this they have been described as planetary-scale sea breezes (Webster and Fasullo 2003), where pressure gradients arising from differential heating of land and ocean drive the monsoonal overturning circulation. In the work of Bordoni and Schneider (2008), the low thermal inertia of the land surface compared with that of the ocean, and not differential heating, is argued to be important for the development of monsoons. Monsoon transitions occur in their model even in the absence of any surface inhomogeneity when the zonal momentum budget in the upper branch of the winter Hadley cell transitions from a regime in which eddy momentum fluxes play a dominant role to a regime in which they are less dominant, allowing the circulation to approach the angular momentum-conserving limit. The transition between the two different regimes is made rapid by eddy-mean flow feedbacks that can act on seasonal time scales only if the lower-level temperatures can adjust rapidly, hence only if the thermal inertia of the lower boundary is sufficiently small. These arguments, which hold for a statistically zonally and hemispherically symmetric climate, might also be relevant for the seasonal onset of the Indian monsoon, in which land in the longitudinal sector over which the monsoon develops is primarily confined to the NH. Our experimental design is modeled after the Indian monsoon sector, and our goal is to understand how adding a zonally symmetric continent in the NH affects the resulting monsoonal circulation.

For decades, axisymmetric models have been used to study tropical overturning circulations, such as Hadley and monsoonal circulations, in steady state (e.g., Held and Hou 1980; Lindzen and Hou 1988; Plumb and Hou 1992; Privé and Plumb 2007a). Held and Hou (1980) explained the existence of the annual-mean Hadley circulation using angular momentum conservation. Lindzen and Hou (1988) expanded upon Held and Hou (1980) by exploring the response to an off-equatorial peak in the forcing, and were able to replicate a "winter" cell, seen in observations. Plumb and Hou

(1992) studied the response of the atmospheric circulation to a localized subtropical temperature perturbation, which is more relevant to monsoonal circulations. They showed that the onset of a cross-equatorial monsoonal circulation only occurs for a supercritical forcing, and they argued that this threshold behavior could be relevant for the rapid seasonal monsoon onset. Privé and Plumb (2007a) used an axisymmetric model to develop a theory for the location of the poleward extent of the monsoon, and found that the poleward limit coincides with the maximum of the sub-cloud moist static energy (MSE), which is in agreement with the quasi-equilibrium view of monsoons (Emanuel 1995). These axisymmetric studies are fundamental papers in the tropical dynamics literature, because they attempt to understand the global circulation using concepts of angular momentum and energy conservation. Although highly idealized, and therefore arguably not very realistic, these models have provided theoretical insight into the basic workings of the monsoon, as well as the Hadley cell.

The simulations presented in this work are performed with a three-dimensional idealized general circulation model (GCM) that includes a seasonal cycle. Unlike axisymmetric models, this model resolves large-scale eddies, which in the extratropics effect energy and momentum transport. The extratropical eddies have been shown to play an important role in the annually-averaged tropical Hadley cell (Walker and Schneider 2006; Schneider 2006) and in the seasonal transition of the monsoonal circulation (Bordoni and Schneider 2008). Three-dimensional models of intermediate complexity have been used before to study the mechanisms that drive monsoons. For example, Chou et al. (2001) found that "ventilation" (negative advection of MSE from the ocean over the continent) plays a large role in setting the poleward extent of the monsoonal precipitation over a zonally-asymmetric continent. Privé and Plumb (2007b) found that lower-level eddies associated with the monsoonal flow redistribute the MSE such that the maximum is closer to the equator than in the axisymmetric models. These studies are in agreement with the theory that the circulation boundary

is co-located with the maximum sub-cloud MSE. Alternatively, Shaw (2014) found that the NH winter cell circulation boundary is located at the latitude of maximum planetary-scale "waviness" in reanalysis data. She verified this with an aquaplanet GCM with stationary subtropical forcing.

Recent work has focused on determining what sets the position of the intertropical convergence zone, or ITCZ, in the annual mean (e.g., Frierson et al. 2013; Donohoe et al. 2013; Bischoff and Schneider 2014). The term ITCZ is historically used to identify the main rain band in the tropics, which is associated with the ascending branch of the Hadley circulation. Here we define monsoons as seasonal excursions of the ITCZ, or the convergence zones of the Hadley circulation, over subtropical continents. Thus we use the terms monsoonal rainfall and summer ITCZ synonymously. Unlike previous work which focused on patterns of sea surface temperatures (SSTs) and boundary layer dynamics (e.g., Young 1987; Lindzen and Nigam 1987; Back and Bretherton 2009; Sobel 2007), recent work uses a large-scale energetic framework to link the position of the ITCZ to the atmospheric energy transport. The link resides in the approximation that the ITCZ is located where the column-integrated atmospheric energy transport, $\langle \overline{vh} \rangle$, changes sign (e.g., Kang et al. 2008; Bischoff and Schneider 2014). In this work we utilize the quantitative estimate presented by Bischoff and Schneider (2014) to determine the ITCZ position.

In addition to the spatial distribution of precipitation, there are also open questions regarding the temporal distribution of precipitation during monsoon onset and retreat. For example, the annual cycle of the ITCZ in the Indian monsoon sector is asymmetric, with a rapid shift from the near-equatorial SH to the Indian subcontinent in the NH and a slower retreat (e.g., Lau and Yang 1996; Sperber et al. 2013). This asymmetry is nontrivial, and has been attributed to processes that provide memory to the climate system, such as surface hydrology (e.g., Xie and Saiki 1999). Our idealized simulations allow us to remove such complexities in order to isolate the

fundamental mechanisms governing the ITCZ progression. Even with an idealized model we find an asymmetric progression of the ITCZ when we add a hemispheric asymmetry in surface heat capacity.

We address two main questions in this work. (1) What determines the poleward extent of the monsoonal precipitation in summer? and (2) How does continental configuration affect the temporal progression of the monsoonal rainfall? The next section describes both the idealized GCM and the simulations we performed. The underlying theory is described in Section 4.3. GCM results are described in Section 4.4. We discuss the mechanisms that set the poleward boundary of the monsoonal precipitation in Section 4.5. The timing of monsoon onset/retreat is analyzed in Section 4.6. Finally, discussion and conclusions are given in Sections 4.7 and 4.8, respectively.

4.2 Idealized GCM

4.2.1 GCM description

The idealized GCM used for these simulations is based on the Geophysical Fluid Dynamics Laboratory (GFDL) dynamical core, which solves the primitive equations of motion on a sphere with the Earth's radius. It resolves well the tropical and extra-tropical circulations, as well as their interaction with each other and with the hydrological cycle. This model has been extensively used to study many aspects of the tropical and extratropical general circulation of the atmosphere and their response to climate change (e.g., O'Gorman and Schneider 2008; Schneider et al. 2010). The GCM is very similar to that of Frierson et al. (2006) and Frierson (2007) and is described in detail in O'Gorman and Schneider (2008). A brief overview is provided here.

In its simplest configuration, the lower boundary of the model is a slab ocean, with uniform mixed-layer depth d. The latitudinal profile of ocean energy transport

is prescribed as an ocean energy flux divergence $\nabla \cdot F_o$, which is zonally symmetric and constant in time (Fig. 4.2; Bordoni (2007)). The GCM does not take into account important climate feedbacks such as those from changes in albedo or clouds. Clouds are not included in this model. The surface albedo is spatially uniform and constant in time ($\alpha = 0.38$).

Radiative heating and cooling are represented by a two-stream radiative transfer scheme for a gray atmosphere, in which absorption and emission of solar and thermal radiation do not depend on wavelength. The prescribed longwave optical thickness is a function of height and latitude, with a maximum at the equator and minimum at the poles. Because the longwave optical thickness is prescribed and does not depend on the water vapor field, radiative water vapor and cloud feedbacks play no part in the responses described here.

The GCM has an active hydrological cycle and is forced by a seasonal cycle of insolation (but no diurnal cycle) with a 360-day year. The obliquity and solar constant are set to Earth-like values of 23.5° and 1360 W m^{-2}, respectively. Precipitation can form by large-scale condensation (when grid-scale motion leads to supersaturation) or in a simplified Betts-Miller convection scheme, and is assumed to fall out of the atmosphere immediately. Thus there is no liquid water or ice in the atmosphere. The convection scheme relaxes the temperature profiles of unstable atmospheric columns to a moist adiabat with a fixed relative humidity of 70% over a time scale of two hours (Frierson 2007).

4.2.2 Simulations

The simulations presented here are performed at T85 spectral resolution in the horizontal with 30 vertical levels. Simulations are integrated for at least 20 years and averaged over the last 10 years.

For this study we performed three simulations. First is the the “Asia” experiment,

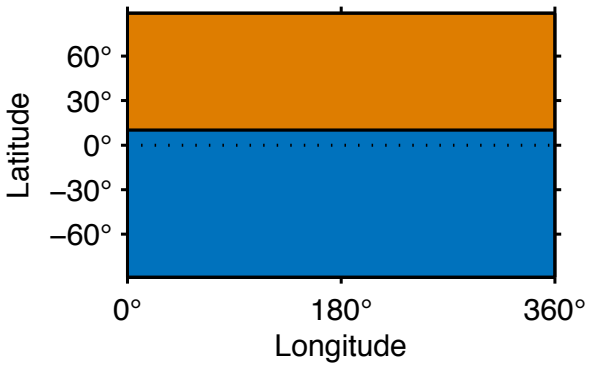

Figure 4.1: Distribution of mixed-layer depth d for the Asia simulation. $d = 0.2$m for the "continent" and $d = 20$m for the "ocean".

which has a fully-saturated continent north of 10°N, shown in Figure 4.1. By "fully saturated" we mean that both over the ocean and over land the surface provides an infinite reservoir of evaporation. Thus "land" and "ocean" are different only in their mixed-layer depth, which is set to $d = 0.2$m for the continent and $d = 20$m for the ocean. We also performed two different aquaplanet simulations: one that is all land ($d = 0.2$m), and one that is all ocean ($d = 20$m).

All three simulations have a prescribed ocean energy flux divergence, shown in Figure 4.2. The ocean energy flux divergence in the Asia simulation (top panel) is hemispherically asymmetric, with convergence in the SH subtropics and divergence at the equator, because of the land in the NH. This amounts to a southward energy transport across the equator. The ocean energy flux divergence for the aquaplanets (bottom panel) is hemispherically symmetric, converging in the subtropics of both hemispheres and diverging at the equator, with no net energy transport across the equator. So, in essence, in these simulations the only aspect of land-sea contrast we account for is the fact that ocean, unlike land, can store and transport energy.

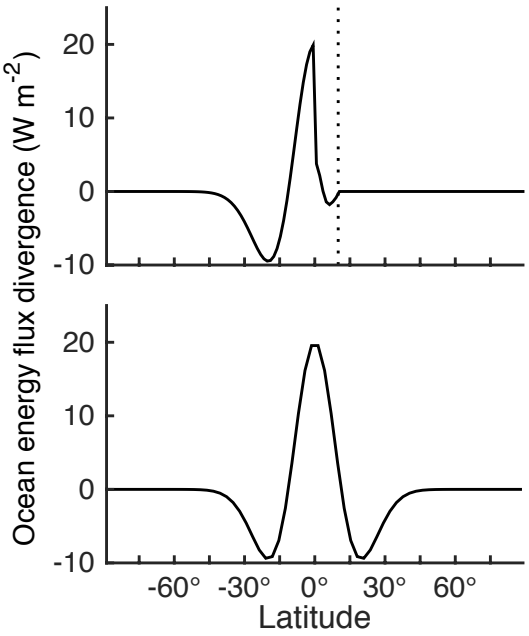

Figure 4.2: Latitudinal profile of the ocean energy flux divergence for the Asia (top) and aquaplanet (bottom) experiments. The dotted vertical line in the top panel experiment represents the boundary of the continent.

4.3 Theory

This section follows closely the moist static energy framework as summarized, for instance, by Neelin (2007) and Merlis et al. (2013). The time-dependent energy balance of the surface and atmosphere can be summed to yield:

$$\partial_y \left\langle \overline{vh} \right\rangle = \mathcal{S} - \mathcal{L} - \mathcal{O} - \mathcal{O}_s - \mathcal{A} \tag{4.1}$$

Here v is the meridional wind velocity, and $h = c_p T + gz + Lq$ is moist static energy, with the specific heat of air at constant pressure c_p, temperature T, gravitational acceleration g, geopotential height z, latent heat of vaporization L, and atmospheric specific humidity q. $\mathcal{S}$ is incoming shortwave radiation at the top of the atmosphere (TOA), and $\mathcal{L}$ is outgoing longwave radiation at the TOA. $\mathcal{A} = \left\langle \frac{\partial \mathcal{E}}{\partial t} \right\rangle$ is the atmospheric energy storage, where $\mathcal{E} = c_v T + gz + Lq$ is the total atmospheric energy.

$\langle\cdot\rangle$ denotes a mass-weighted vertical integral over the atmospheric column, and the overbar denotes a zonal and temporal mean.

Here $\mathcal{O} = \nabla \cdot F_o$ is the divergence of the meridional ocean energy flux F_o which is prescribed in our simulations (Fig. 4.2). The ocean energy storage is $\mathcal{O}_s = c_{po}\rho_o d\frac{\partial T_s}{\partial t}$, with water density ρ_o, water heat capacity c_{po}, mixed-layer depth d and surface temperature T_s. The surface energy budget is:

$$\mathcal{O}_s = \mathcal{S}^{net}_{SFC} - \mathcal{L}^{net}_{SFC} - LH - SH - \nabla \cdot F_o \tag{4.2}$$

Here, LH and SH are the surface latent and sensible heat fluxes, respectively. $\mathcal{O}_s$ is negligible over land because of its small heat capacity, but not negligible over ocean because it has a larger heat capacity and is therefore able to store energy. Note that in much of the literature $\mathcal{O} + \mathcal{O}_s$ is known as the ocean heat uptake. Here we keep these terms separate because the ocean energy flux divergence $\mathcal{O}$ does not vary on seasonal timescales in our simulations, but the storage $\mathcal{O}_s$ does.

Here we define the effective F^{net} as the radiative and storage terms that must be balanced by the horizontal atmospheric moist static energy flux divergence $\partial_y \langle\overline{vh}\rangle$ in the zonal mean:

$$F^{net} = \mathcal{S} - \mathcal{L} - \mathcal{O} - \mathcal{O}_s - \mathcal{A} \tag{4.3}$$

Note that in the conventional moist static energy framework (Neelin 2007), F^{net} is the net energy input to the atmospheric column, defined by the radiative and surface fluxes at the upper and lower boundary of the column. Here there is a slight difference in that we include the atmospheric storage term within F^{net}, and we represent the surface fluxes by the surface energy storage term $\mathcal{O}_s$.

Equations (4.1) and (4.3) tell us that the net energy input to the atmospheric column must be balanced by the divergence of moist static energy in the atmosphere. Thus the atmosphere responds to changes in energy input with changes in atmospheric

energy transport.

As done by Frierson and Hwang (2012), we integrate Eq. (4.1) in latitude to obtain $\left\langle \overline{vh} \right\rangle_0 = \frac{1}{2}\left(F^{net}_{\mathrm{SH}} - F^{net}_{\mathrm{NH}}\right)$. Here the subscripts SH and NH denote integrals from the equator to the pole in either hemisphere, and the subscript 0 indicates that the quantity is evaluated at the equator. Thus the cross-equatorial atmospheric energy flux $\left\langle \overline{vh} \right\rangle_0$ is proportional to the difference between the meridionally-integrated F^{net} in the two hemispheres.

In Bischoff and Schneider (2014) and Bischoff and Schneider (2015), a relationship for the displacement of the ITCZ off the equator is derived using the column-integrated atmospheric energy transport $\left\langle \overline{vh} \right\rangle$. This energy transport in the tropics is dominated by the upper branch of the Hadley circulation, and so the direction of the transport tends to be in the direction of the mass flux in the upper branch. The estimate for the ITCZ position is derived by assuming (1) that the ITCZ is located where $\left\langle \overline{vh} \right\rangle$ changes sign (i.e., at the "energy flux equator" hereafter referred to as the EFE) and (2) that $\left\langle \overline{vh} \right\rangle$ is linear between the equator and the EFE. This provides a first-order estimate of the ITCZ position:

$$\delta \approx -\frac{1}{a}\frac{\left\langle \overline{vh} \right\rangle_0}{\partial_y \left\langle \overline{vh} \right\rangle_0} = -\frac{1}{a}\frac{\left\langle \overline{vh} \right\rangle_0}{\mathcal{S}_0 - \mathcal{L}_0 - \mathcal{O}_0 - \mathcal{O}_{s0} - \mathcal{A}_0} \tag{4.4}$$

Here δ is the displacement of the ITCZ off the equator, and a is the planetary radius. Because we are considering seasonal cycles, the denominator explicitly accounts for the atmospheric and oceanic heat storage, which is not included in the steady-state simulations of Bischoff and Schneider (2014).

As shown in previous studies (e.g., Schneider et al. 2014; Adam et al. 2015), the ITCZ is not always co-located with the energy flux equator, which is the first assumption needed for Eq. (4.4) to hold. However, the ITCZ and EFE are correlated both in structure and magnitude in our simulations.

The second assumption relies on the MSE flux being linear between the equator and the EFE. This approximation holds either if the EFE is very close to the equator or if the MSE flux is in fact linear. Even though the EFEs are displaced far from the equator in our simulations, the fluxes are approximately linear in the tropics and so this approximation holds well (Fig. 4.5).

Thus this theory states that the EFE, and thus the ITCZ, position depends on both the cross-equatorial atmospheric energy flux $\langle \overline{vh} \rangle_0$ and the net energy input into the equatorial atmosphere $\mathcal{S}_0 - \mathcal{L}_0 - \mathcal{O}_0 - \mathcal{O}_{s0} - \mathcal{A}_0$. The denominator can be thought of as a sensitivity parameter: When it is large, the ITCZ is relatively less sensitive to changes in the cross-equatorial atmospheric energy flux, but when it is small, a slight change in the cross-equatorial atmospheric energy flux can produce large excursions in the ITCZ position. A change in either term by itself can produce a change in the ITCZ position, and a change in both terms might not necessarily change the ITCZ position. This theory was tested on idealized global and tropical warming simulations in Bischoff and Schneider (2014) and Bischoff and Schneider (2015). Here, we extend it to consider seasonal cycles.

4.4 GCM Results

The top panel of Figure 4.3 shows the distribution of precipitation in the Asia experiment for JJA (June, July and August) and DJF (December, January and February) seasonal averages, and in the annual mean. In NH summer, there are two major precipitation maxima, one over the continent around 23° and one just south of the continent at 9°. In SH summer, there is one large precipitation maximum located at −12°. The ITCZ in NH summer (over land) is located further poleward than in the SH summer (over ocean), but more rain falls in the SH summer. In the annual mean, the local maximum precipitation is located about 1° north of the equator, but the

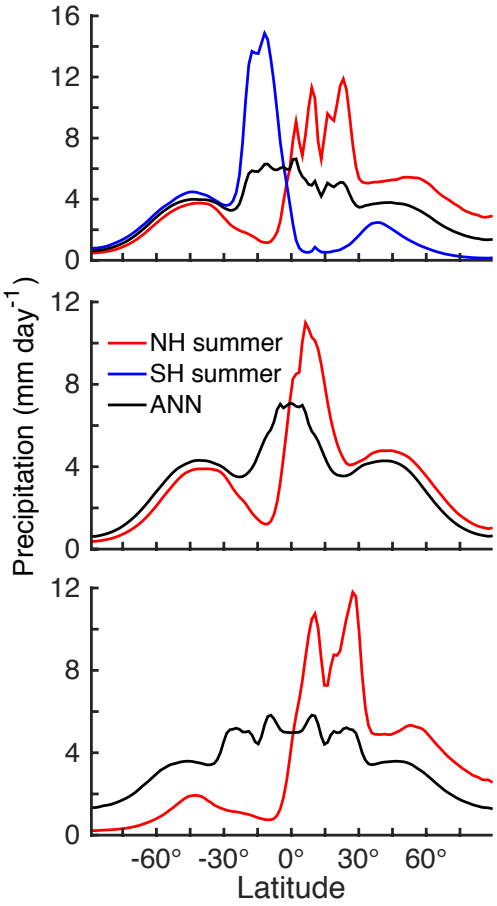

Figure 4.3: Latitudinal distribution of precipitation in mm day^{-1} for the Asia (top panel), "all ocean" aquaplanet (middle panel) and "all land" aquaplanet (bottom panel). Precipitation is shown for NH summer (red), SH summer (blue), and the annual mean (black). In the aquaplanet simulations, only one solstice season is shown (NH summer), because the two hemispheres are completely symmetric.

bulk of the precipitation falls south of the equator. Thus, we take the ITCZ to lie just south of the equator at $-5°$ in the annual mean, more in line with the center of the precipitation distribution.

The bottom two panels show the annual-mean and summer precipitation for the two aquaplanet simulations. In the "all ocean" aquaplanet, the average summer ITCZ position is 6° from the equator, while in the "all land" aquaplanet the precipitation maximum is located 27° from the equator during summer. There is also another precipitation maximum located at 10° in the "all land" aquaplanet. These two maxima

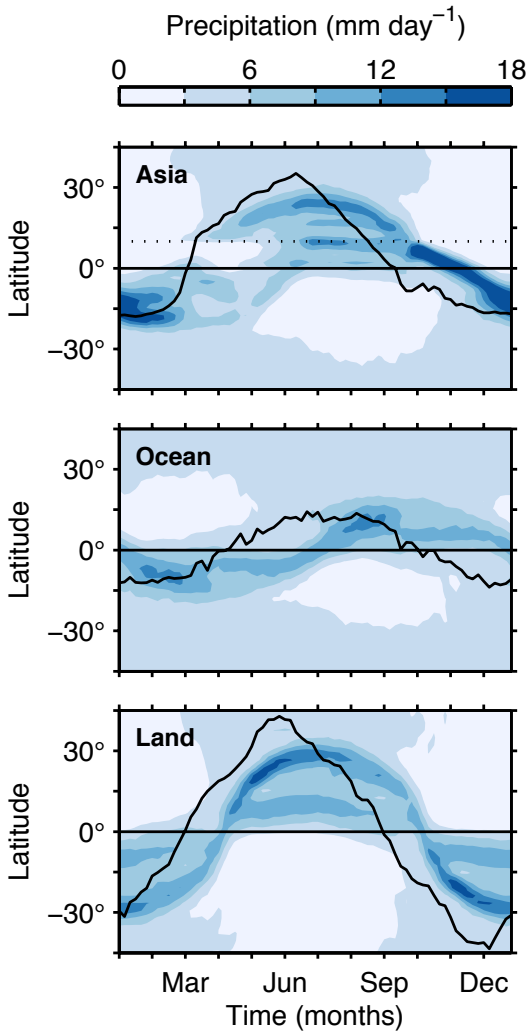

Figure 4.4: Seasonal cycle of precipitation for the three simulations: Asia (top), ocean aquaplanet (middle) and land aquaplanet (bottom). The black curve is the EFE. The dotted line in the top panel represents the continent boundary.

are associated with the same monsoonal circulation cell.

Figure 4.4 shows the seasonal cycle of precipitation (colors) and the EFE (black line) for the three simulations. One striking feature of precipitation in the Asia experiment is the rapid jump in the ITCZ from the SH to the NH during NH spring, coinciding with a brief period of double ITCZs. Although this transition is abrupt, the retreat of the ITCZ is slower, much like what is observed in the real South Asian Monsoon (cf. Fig. 4.16).

The ITCZ progression is relatively smooth for the aquaplanet simulations, with the ITCZ and EFE migrating much further poleward for smaller values of the mixed-layer depth d. For the "all land" simulation, the ITCZ reaches a maximum poleward extent of 29°, while in the "all ocean" simulation it only migrates a maximum of 12° from the equator.

Comparing the Asia and aquaplanet simulations reveals that the precipitation distribution for Asia is not just a superposition of the two aquaplanet simulations and that, in fact, the hemispheric asymmetry in surface heat capacity has important and nontrivial consequences on the tropical circulation and precipitation. The monsoonal rainfall over the SH ocean in the Asia experiment reaches −19°, which is 7° further poleward than that in the "all ocean" experiment. On the other hand, the ascending branch of the monsoonal circulation over the continent does not migrate as far poleward as it does in the "all land" aquaplanet (25° for Asia versus 29° for "all land"). These differences imply that there are some mechanisms arising from the hemispheric asymmetry that shift the ITCZ further poleward in the SH summer and equatorward in NH summer relative to the aquaplanet counterparts.

In the next two sections we strive to understand the hemispheric and temporal asymmetries in the Asia simulation, using the aquaplanet simulations for reference.

4.5 Poleward boundary of ITCZ

4.5.1 Hemispheric energy imbalance

We want to determine what sets the poleward extent of monsoonal precipitation both in the seasonal average and in the annual mean. To understand the differences between the aquaplanet and Asia experiments, we turn to the atmospheric energy budget Eq. (4.1). The Hadley circulation exists in the tropics in order to redistribute energy on a differentially-heated planet. When we introduce a hemispheric asymmetry

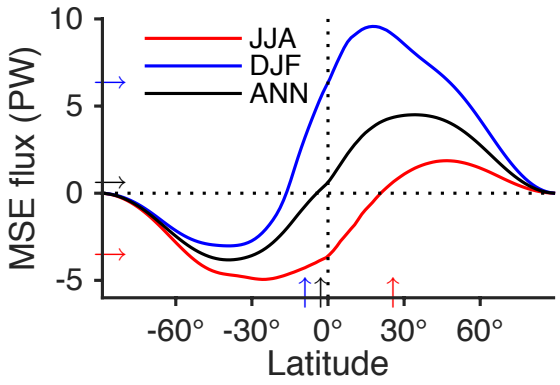

Figure 4.5: The vertically-integrated atmospheric energy flux $\langle \overline{vh} \rangle$ in JJA (red), DJF (blue) and the annual mean (black) for the Asia simulation. Arrows pointing horizontally indicate the value of the flux at the equator for each season. Arrows pointing vertically indicate the ITCZ location in each season.

in heat capacity, for example, it changes the distribution of energy (F^{net}) and thus the atmospheric energy transport by the Hadley circulation.

If there is no hemispheric asymmetry in the energy budget, a cross-equatorial energy transport might not be needed. For example, if the planet is heated symmetrically (i.e., perpetual equinox), the ITCZ would remain at the equator and there would be no mean cross-equatorial atmospheric energy flux. If the planet is hemispherically symmetric and there is a seasonal cycle, we expect the annual mean ITCZ to be right at the equator (e.g., the aquaplanet simulations). The excursions of the ITCZ off the equator occur in the solstice seasons, in response to the hemispheric asymmetry in solar insolation, and the atmosphere must transport energy across the equator. The transport by the Hadley cell has the same sign as the mass flux in the cell's upper branch, to the extent that the effective energy stratification, or gross moist stability, is positive. Since the aquaplanet is hemispherically and temporally symmetric, these seasonal effects cancel out in the annual mean.

For the Asia experiment, however, there is an interhemispheric asymmetry in heat capacity, which ultimately leads to the ITCZ (and EFE) being located in the SH in the annual mean. Figure 4.5 shows the meridional MSE fluxes $\langle \overline{vh} \rangle$ for the Asia

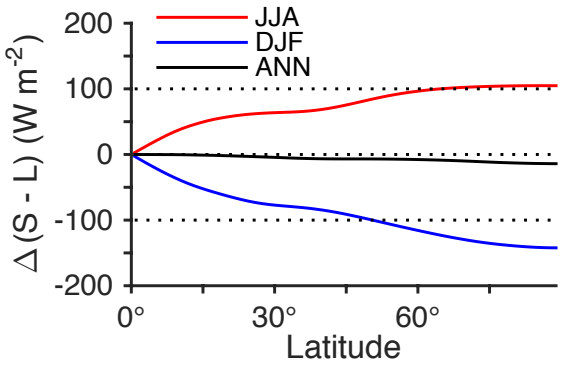

Figure 4.6: $\Delta(\mathcal{S}-\mathcal{L}) = (\mathcal{S}-\mathcal{L})_{NH} - (\mathcal{S}-\mathcal{L})_{SH}$ is the hemispheric asymmetry in TOA radiation as a function of latitude, shown for JJA (red), DJF (blue), and the annual mean (black). Negative values indicate that the NH receives less TOA radiation than the SH, and vice-versa.

experiment in JJA, DJF, and the annual mean. The black line shows that there is an annual-mean asymmetry in the energy budget, with the atmosphere transporting energy from the SH to the NH in the annual mean (i.e., $\langle\overline{vh}\rangle > 0$ at the equator). This leads to an ITCZ that is located in the SH, which is the warmer hemisphere. This relationship between the ITCZ and the cross-equatorial atmospheric energy transport has been demonstrated before in both models and observations (e.g., Frierson et al. 2013; Donohoe et al. 2013).

How does the hemispheric asymmetry in the energy budget arise in the Asia experiment the annual mean? It might not appear obvious given our model setup why the SH should be warmer than the NH. The solar forcing $\mathcal{S}$ is hemispherically symmetric, and the surface ($\mathcal{O}_s$) and atmospheric energy storage ($\mathcal{A}$) average to zero over the course of a year. Here we will consider the case with no prescribed ocean energy transport $\mathcal{O}$.[1] The asymmetry, then, must arise from the outgoing longwave radiation $\mathcal{L}$, which is, in the annual average, larger in the NH than in the SH latitude by latitude.

[1]For the Asia simulation a hemispherically-asymmetric ocean energy flux divergence $\mathcal{O}$ is prescribed that transports energy southward in the annual mean. This does shift the ITCZ towards the SH, relative to a simulation with $\mathcal{O} = 0$. However, even in the Asia simulation with $\mathcal{O} = 0$ the ITCZ resides in the SH.

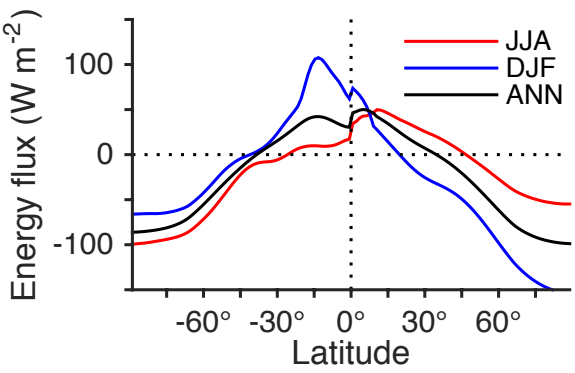

Figure 4.7: Average distribution of $F^{net} = \mathcal{S} - \mathcal{L} - \mathcal{O} - \mathcal{O}_s - \mathcal{A}$ with latitude in JJA (red), DJF (blue) and the annual mean (black) for the Asia simulation.

Figure 4.6 shows the difference between $\mathcal{S} - \mathcal{L}$ in the NH and the SH, $\Delta(\mathcal{S} - \mathcal{L}) = (\mathcal{S} - \mathcal{L})_{NH} - (\mathcal{S} - \mathcal{L})_{SH}$, for the solstice seasons and the annual mean. The black line shows that the NH receives slightly less TOA radiation than the SH in the annual mean, because $\mathcal{L}$ is slightly larger in the NH in the annual mean. This is because $\mathcal{L}$ is a function of temperature, and the continent reaches very hot temperatures in the NH summer and radiates much of that energy back to space. Note that, in our idealized model, there are not cloud or water vapor feedbacks that might compensate somewhat for this effect. The ocean, on the other hand, cannot fully equilibrate with the incoming radiation because of its larger heat capacity and hence has smaller temperature variations than the continent over the course of the seasonal cycle. This results in the annually-averaged F^{net} being slightly larger in the SH than in the NH, and thus $\left\langle \overline{vh} \right\rangle_0 = \frac{1}{2}\left(F^{net}_{SH} - F^{net}_{NH}\right) > 0$ (Fig. 4.5).

During the solstice seasons, these same arguments hold. The hemispheric energy imbalance is dominated by the shortwave flux $\mathcal{S}$, since the summer hemisphere is being heated much more by the sun than the winter hemisphere. This results in the EFE and ITCZ moving into the summer hemisphere. Because of the difference in $\mathcal{L}$ between DJF and JJA, the hemispheric imbalance in TOA radiation is larger in DJF than in JJA, as shown by comparing the red and blue lines in Fig. 4.6. This is

consistent with the fact that the cross-equatorial energy flux $\langle\overline{vh}\rangle_0$ is larger in DJF than in JJA (compare red and blue horizontal arrows in Fig. 4.5), even though F^{net} is not entirely determined by $\mathcal{S} - \mathcal{L}$, but also includes the effects of seasonal ocean energy storage $\mathcal{O}_s$. The full F^{net} is shown in Figure 4.7. The ocean energy storage acts to balance out the hemispheric asymmetry in both JJA and DJF, since the ocean stores heat in the summer and releases it back to the atmosphere during winter. The atmospheric energy storage $\mathcal{A}$ has a negligible effect when averaged over a season.

Hence we arrive at an interesting outcome: the cross-equatorial atmospheric energy flux is larger in DJF, but the ITCZ reaches its most poleward position in JJA. This result is at odds with previous work that suggests that the ITCZ position is linearly proportional to $-\langle\overline{vh}\rangle_0$ with a constant slope across a wide range of time scales and forcings (Donohoe et al. 2013). As discussed in the next section, this apparent contradiction is consistent with and explained by the theory presented in Section 4.3.

4.5.2 Quantitative estimates of the ITCZ position

While the arguments above allow for a qualitative understanding of the ITCZ annual mean position and seasonal migrations, more quantitative understanding can be achieved by using the theory of the ITCZ position recently developed by Bischoff and Schneider (2014) and summarized in Section 4.3.

While our simulations do not adhere strictly to the two assumptions used to derive Eq. (4.4), the EFE expansion provides a useful estimate for the ITCZ location. The EFE does capture the fact that the ITCZ migrates further poleward in JJA than in DJF, and that the ITCZ resides just south of the equator in the annual mean (cf. Fig. 4.5). Thus it remains useful to use this framework for studying the location of the monsoonal precipitation.

For the Asia simulation, in JJA, $\delta = 31^\circ$ and the ITCZ is located at 23°. For DJF, $\delta = -21^\circ$ and the ITCZ is located at -12°. In the annual mean, $\delta = -4^\circ$,

and the ITCZ is located around $-5°$. This estimate is not perfect, but it captures the most important feature of the seasonality in the Asia simulation: that the ITCZ migrates further poleward in the NH summer than in the SH summer. For the "all ocean" aquaplanet, $\delta = 10°$ in the summer and the ITCZ is located at 6°. For "all land" $\delta = 33°$ during summer and the ITCZ is located at 27°.

Since the cross-equatorial atmospheric energy flux is larger in the SH summer, but the ITCZ is positioned closer to the equator during this season, the denominator of δ, $F_0^{net} = \mathcal{S}_0 - \mathcal{L}_0 - \mathcal{O}_0 - \mathcal{O}_{s0} - \mathcal{A}_0$, must be larger in DJF than in JJA. This is indeed the case, as shown by Figure 4.7. This is an example of how the denominator in Eq. (4.4) acts as a "sensitivity factor," making it more or less easy to change the ITCZ position for a given change in $\langle \overline{vh} \rangle_0$ (cf. Section 4.3, Bischoff and Schneider 2014). In DJF, the net energy input into the equatorial atmosphere is almost twice as large as it is in JJA, so it only allows the ITCZ to move approximately half as far as in JJA for every unit increase in the cross-equatorial energy flux.

Thus it is clear that in order to understand the seasonal position of the ITCZ, we need to understand both the cross-equatorial energy transport $\langle \overline{vh} \rangle_0$ and its divergence $\partial_y \langle \overline{vh} \rangle_0 = \mathcal{S}_0 - \mathcal{L}_0 - \mathcal{O}_0 - \mathcal{O}_{s0} - \mathcal{A}_0$. $\langle \overline{vh} \rangle_0$ can be understood from the hemispheric asymmetry in F^{net}, whereas understanding the energy flux divergence requires more careful consideration of the atmospheric and surface energy budgets.

This analysis provokes the question: Why is F_0^{net} so much larger in DJF than in JJA? This will be discussed in detail in Section 4.6.2, where we look more closely at the seasonal cycle of the cross-equatorial energy flux and its divergence.

4.6 Timing of Monsoon Onset/Retreat

4.6.1 Caveats

In this and the following sections, we use the atmospheric energy budget to investigate the timing of ITCZ shifts in NH and SH spring. There are a few caveats to this approach. First, there is a conspicuous lag between the EFE and the ITCZ, such that the EFE crosses the equator 30-120 days before the ITCZ does (depending on the mixed-layer depth). The theory in Bischoff and Schneider (2014) assumes that the two are co-located. This lag may be a model artifact, for it has been observed in the CMIP3 models as well, but does not appear to be present in observations (Donohoe et al. 2013; Chamales et al. 2015). However, because of the lag it is less obvious how the arguments that explain the EFE position can be extended to account for the ITCZ position in these simulations. More specifically, since there is a lag, there are times when the ITCZ and the EFE are on opposite sides of the equator (cf. Fig. 4.4). This means that the mass transport and the energy transport are in opposite directions across the equator, which is reconciled by an adjustment of the gross moist stability (GMS). This needs to be investigated further, but is beyond this scope of this research. Despite these caveats, the seasonal cycle of the EFE well correlates with the seasonal cycle of the ITCZ position, despite the time lag between the two. Hence, in the rest of this section we will use the EFE as a proxy for the ITCZ.

Second, the theory assumes that eddy energy fluxes $\langle\overline{v'h'}\rangle$ are negligible at the EFE location, so that the EFE is the zero of the mean energy flux. This is not true at all times in our simulations. In fact, the eddy component of the flux is important in the tropics, and sets the position of the EFE at some times. Surprisingly, the latitude at which the eddy energy flux changes sign coincides with the ITCZ at most times, while the latitude at which the mean energy flux changes sign is not always correlated with the ITCZ. This goes against the widely-held notion that

the mean energy transport goes to zero at the boundary of the mean meridional circulation. The mean energy flux does not always change sign at the ascending branch, although that latitude is usually a point of minimum transport. We suspect that these inconsistencies in our simulations arise from the vertical structure of the circulation, in which ascent occurs along slanted streamlines in non-negligible portions of the Hadley cell ascending branch, but more time must be dedicated to examining the cause of this discrepancy.

Although the ITCZ crosses the equator early in NH spring, this transition is not associated with the monsoon onset. In fact, a "double ITCZ" appears at this time, with precipitation over the NH continent and over the SH tropical ocean. If we consider the monsoon to be a deep, cross-equatorial circulation with ascending branch in the summer hemisphere subtropics and descending branch in the opposite hemisphere, in agreement with many studies, the monsoon onset only occurs in June. The early NH spring transition is instead associated with the development of a local, linear and narrow cell over the continent, as described in Section 4.6.4.1. The SH spring is characterized by a gradual and smoothly-shifting ITCZ.

The fact that there is a NH ITCZ/EFE transition that does not coincide with monsoon onset means the energy budget framework will be less useful for looking at NH monsoon onset. The occurrence of this secondary transition is a limitation of our model setup, and will be discussed below. Nonetheless, the early transition of the ITCZ from the southern to the northern hemisphere (and the onset of the double ITCZ) is still an interesting feature in our simulation, and we want to understand what controls its timing. In the following, "monsoon onset" will therefore refer to the onset of a deep and cross-equatorial winter cell in June while "NH EFE/ITCZ transition" refers to the rapid shift in the EFE from the SH to the NH in March. The next section will discuss the ITCZ shifts and Section 4.6.5 will discuss the NH monsoon onset.

4.6.2 Energy budget and ITCZ shifts

Figure 4.4 shows the energy flux equator $\langle \overline{vh} \rangle = 0$ (black line in each panel), or EFE, as a function of time for the three experiments. For Asia, the EFE exhibits the same rapid onset and slow retreat pattern as the ITCZ, albeit shifted by ≈ 30 days.

We want to understand what makes the NH and SH EFE transition so different in boreal and austral spring, with a rapid transition from the SH to the NH in March and a more gradual shift back to the SH in September. Using Eq. (4.4), the two quantities that define the EFE position are the cross-equatorial atmospheric energy flux $\langle \overline{vh} \rangle_0$ and the net energy input to the equatorial atmosphere $\partial_y \langle \overline{vh} \rangle_0 \approx \mathcal{S}_0 - \mathcal{L}_0 - \mathcal{O}_0 - \mathcal{O}_{s0}$. Changes in either one of these terms over the course of the seasonal cycle could produce asymmetries in the timing of the EFE progression. Note that here we have neglected $\mathcal{A}_0$ because it is much smaller than the other terms, however it is included in all calculations.

The seasonal cycle of these two terms is plotted in Fig. 4.8 for all three experiments. The "transition period," when the EFE shifts from one hemisphere to the other, is shaded for each simulation. This is taken as the period beginning 10 days before and ending 10 days after the EFE crosses the equator. Blue arrows indicate the time of monsoon onset, defined as the development of a deep, cross-equatorial circulation, and red arrows indicate the beginning of the brief double-ITCZ period during NH spring.

The cross-equatorial atmospheric energy flux $\langle \overline{vh} \rangle_0$ exhibits an asymmetry in its temporal structure between the two transition periods, although not as dramatic as the EFE, with $\langle \overline{vh} \rangle_0$ changing more rapidly in the SH-NH transition and more slowly in the NH-SH transition (top left panel, compare slopes of the lines near the shaded region). The asymmetry comes from a combination of temporal asymmetries in the surface and atmospheric energy storage terms. In general the hemispheric asymmetry in F^{net}, ΔF^{net}, is dominated by $\Delta(\mathcal{S} - \mathcal{L})$, which is temporally symmetric

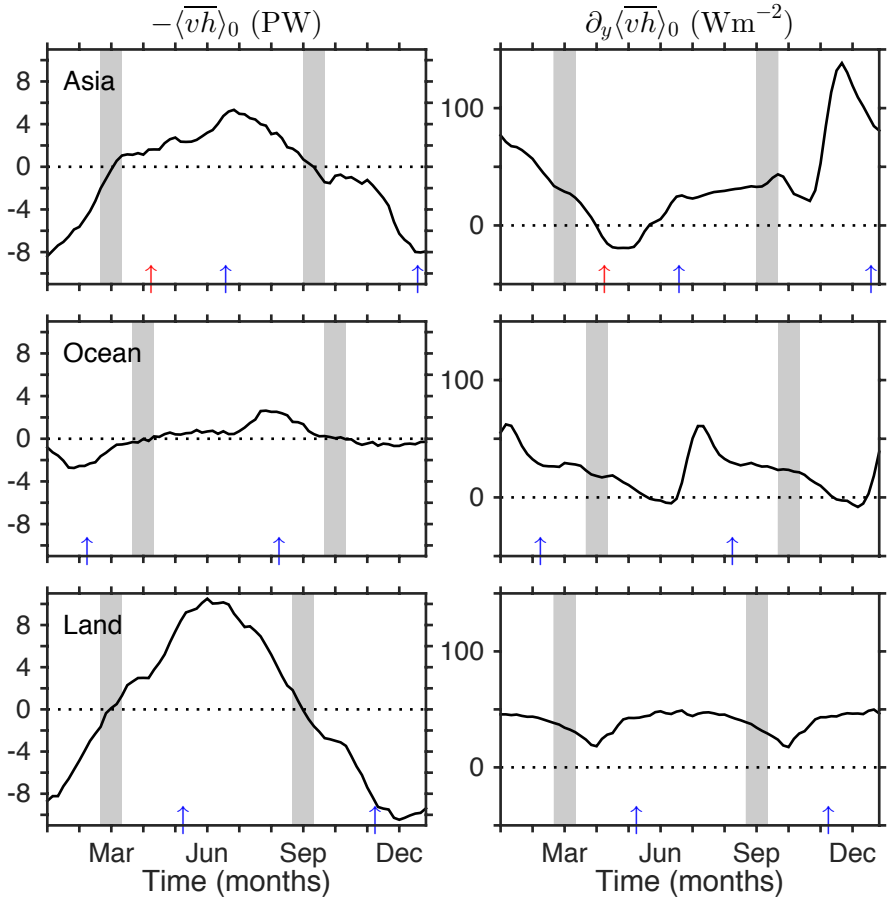

Figure 4.8: Seasonal cycle of the atmospheric energy flux at the equator (left) and its divergence (right). Three simulations are shown: The Asia simulation (top row), the 20-m aquaplanet (middle row) and the 0.2-m aquaplanet (bottom row). The two terms plotted are the numerator and denominator of δ in Eq. (4.4), respectively. Shading represents the transition time, during which the EFE crosses the equator. Blue arrows indicate monsoon onset, as defined by the development of a deep, cross-equatorial circulation. The red arrows in the top panel indicate the beginning of the brief double-ITCZ period during NH spring for the Asia simulation.

and changes more rapidly than $\langle\overline{vh}\rangle_0$. Here the Δ refers to the difference between the SH and NH. In the NH spring the storage terms have a small effect on $\langle\overline{vh}\rangle_0$, allowing the hemispheric asymmetry to change rapidly like $\Delta(\mathcal{S}-\mathcal{L})$. In SH spring they have a larger effect, causing $\langle\overline{vh}\rangle_0$ to change less rapidly. At least for the Asia simulation (and possibly the ocean simulation as well), the monsoon onset (blue arrows) seems to occur immediately following a rapid increase in $\langle\overline{vh}\rangle_0$.

The divergence of this flux, or the net energy input to the equatorial atmosphere, has approximately the same value in the transition periods, but has a more temporally asymmetric structure than $\langle\overline{vh}\rangle_0$ (top right panel). This term changes sign when it starts raining over the NH continent, at the onset of the double ITCZ (red arrow). At the point when $\partial_y\langle\overline{vh}\rangle_0 = 0$, the linear approximation breaks down and higher order terms in the Taylor expansion are needed and the precipitation distribution shows a propensity for a double ITCZ structure (Bischoff and Schneider 2015). Before and after this period the linear approximation holds and the divergence is small, allowing the EFE to shift relatively quickly and relatively far, farther than it does in SH summer. After the SH spring EFE transition, on the other hand, $\partial_y\langle\overline{vh}\rangle_0$ rapidly increases, making it difficult to move the EFE, and causing the ITCZ to shift more slowly around the time of monsoon onset.

In the "all ocean" and "all land" aquaplanet simulations, $\partial_y\langle\overline{vh}\rangle_0$ is temporally symmetric, and the EFE transitions occur when the net energy input is decreasing toward its minimum value (bottom two rows of Fig. 4.8). Like for the Asia simulation, F^{net} decreases to zero for the 20-m aquaplanet simulation after the EFE crosses the equator but right before the ITCZ crosses the equator.

It is the ratio of the cross-equatorial energy flux $\langle\overline{vh}\rangle_0$ and the net energy input to the equatorial atmosphere $\partial_y\langle\overline{vh}\rangle_0$ that defines the EFE position (4.4). Thus Figure 4.8 shows that, for land, the EFE position can be explained almost entirely by the cross-equatorial energy flux (Fig. 4.8 left column), since the net energy input to

the equatorial atmosphere (Fig. 4.8 right column) remains fairly constant throughout the seasonal cycle. On the other hand, for configurations with ocean at the equator, the cross-equatorial energy flux cannot tell the whole story, because the net energy input to the equatorial atmosphere varies substantially throughout the seasonal cycle. For example, $\left\langle \overline{vh} \right\rangle_0$ reaches a maximum of 11 PW for "land" and 3 PW for "ocean" over the seasonal cycle. This would imply that the maximum poleward ITCZ position for the "land" aquaplanet (29°) would be roughly a factor of 4 larger than that of the "ocean" aquaplanet. However, the ITCZ over ocean migrates further, with 12° being its maximum poleward extent, than this linear relationship would suggest, simply because $\partial_y \left\langle \overline{vh} \right\rangle_0$ varies more widely for the "ocean" aquaplanet. Thus the fact that the ITCZ progresses rapidly in NH spring and more slowly in SH spring in the Asia simulation is due to a combination of $\left\langle \overline{vh} \right\rangle_0$ and $\partial_y \left\langle \overline{vh} \right\rangle_0$.

Mechanistically, we want to understand what causes the temporal asymmetry in the net energy input to the equatorial atmosphere for the Asia experiment, allowing the timing of the EFE progression to vary throughout the seasonal cycle. The most notable variations in $\partial_y \left\langle \overline{vh} \right\rangle_0$ that cause variations in the EFE progression are (1) both the fact that it is decreasing and the fact that it goes all the way to zero in NH spring, and (2) the sharp increase that occurs at the end of NH fall and beginning of NH winter. The net energy input to the equatorial atmosphere can be decomposed via Eq. (4.1) into $\partial_y \left\langle \overline{vh} \right\rangle_0 = F_0^{net} \approx \mathcal{S}_0 - \mathcal{L}_0 - \mathcal{O}_0 - \mathcal{O}_{s0}$. This decomposition is shown for the Asia simulation in the top two panels of Figure 4.9. During the NH spring double-ITCZ period, the storage term O_{s0} (black line in middle panel) becomes large enough to completely compensate the top-of-atmosphere energy input $\mathcal{S}_0 - \mathcal{L}_0 - \mathcal{O}_0$. In other words, the shortwave, longwave, and oceanic heat fluxes at the equator are completely taken up via ocean energy storage at that time. Thus there is actually no net energy input into the equatorial atmosphere, and the energy budget does not require an energy flux divergence at the equator. In fact, for a brief period when F_0^{net}

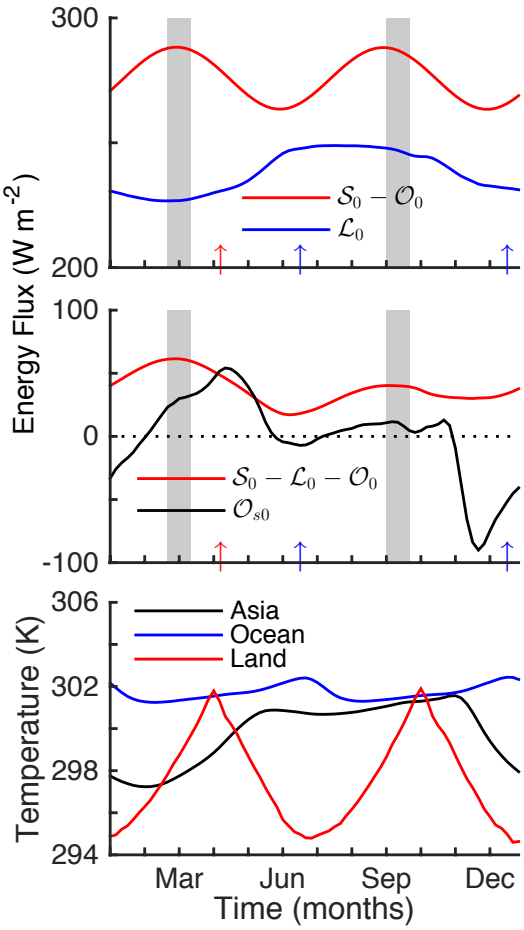

Figure 4.9: Seasonal cycle of the terms comprising the net energy input to the equatorial atmosphere. (top) $\mathcal{S}_0 - \mathcal{O}_0$ and $\mathcal{L}_0$ for the Asia simulation, (middle) $\mathcal{S}_0 - \mathcal{O}_0 - \mathcal{L}_0$ and the ocean energy storage $\mathcal{O}_{s0}$ for the Asia simulation, and (bottom) equatorial surface temperature for all three simulations. Shading and arrows are the same as in Figure 4.8.

is negative, energy must be transported towards the equator.

The middle panel of Figure 4.9 shows that the ocean energy storage $\mathcal{O}_{s0}$ is significantly asymmetric in time. $\mathcal{O}_s = c_{po}\rho_o d\frac{\partial T_s}{\partial t}$ is a function of the mixed-layer depth d and the surface temperature T_s. If d is very small, like for the "all land" aquaplanet simulation, then the storage term will be negligible because surface temperature changes happen instantaneously. This is why the large fluctuations in the net energy input are not present in the land aquaplanet, and why F_0^{net} remains relatively constant throughout the seasonal cycle. If d is larger, like for the "all ocean" aqua-

planet, then $\mathcal{O}_s$ is associated with the seasonal cycle of surface temperature. Thus the same compensation between $\mathcal{S}_0 - \mathcal{L}_0 - \mathcal{O}_0$ and $\mathcal{O}_{s0}$ can occur for the ocean aquaplanet, causing F_0^{net} to go to zero for a brief period twice during the seasonal cycle.

The equatorial surface temperature is plotted in the bottom panel of Figure 4.9 for all three simulations. If we compare the Asia simulation with the ocean aquaplanet, we see that in JJA their equatorial surface temperatures look very similar, but in DJF the surface temperatures for Asia are much lower than that of the 20-m aquaplanet. In other words, for Asia the storage term becomes large and negative in SH spring because there is a large cooling of the equatorial ocean, which corresponds to a release of heat from the ocean to the atmosphere. The ocean takes up heat in NH spring when the equatorial surface warms back up.

The seasonal cycle of surface temperature sets both the storage term (if the surface heat capacity is sufficiently large) and also the OLR $\mathcal{L}$ in our model. $\mathcal{L}$ is closely tied to surface temperature because there are no cloud or water vapor feedbacks in this idealized model to allow re-absorption of that radiation within the atmosphere, and therefore it must be emitted back to space. Because T_{s0} has a single peak in the Asia simulation, $\mathcal{L}_0$ does too (top panel of Fig. 4.9). The structure of $\mathcal{O}_{s0}$, with ocean heat storage in NH spring and ocean heat release in SH spring, also corresponds to the pattern of surface temperature variations.

So the question becomes, why does the equatorial surface temperature have a single peak in the seasonal cycle of the Asia simulation, whereas the two aquaplanets have a double-peak structure? The equatorial SSTs in the Asia simulation can be compared with the "all ocean" aquaplanet because both of them have a 20-m mixed-layer depth at the equator. The pattern of T_s for Asia is similar to that in the "ocean" aquaplanet during NH summer and fall, but there is a significant cooling that occurs in NH winter that causes departures from the "ocean" case. In the following sections, we explain how dynamics plays a role in creating this temporal asymmetry in the

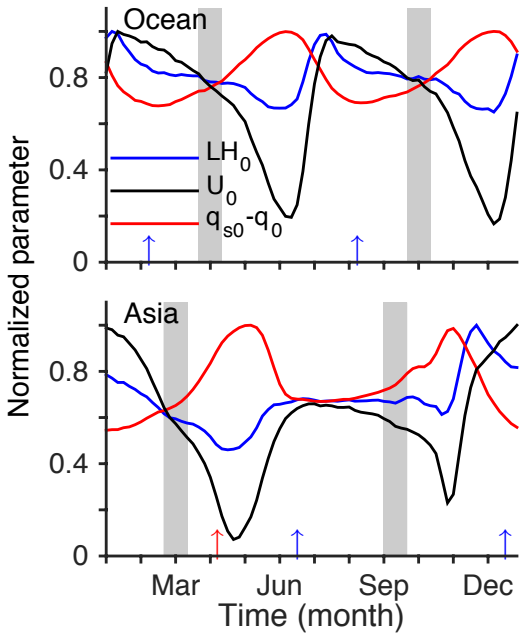

Figure 4.10: Seasonal cycle of the surface latent heat flux LH, surface wind speed U, and vertical moisture gradient $(q_s - q)$ at the equator for the all ocean aquaplanet (top) and the Asia simulation (bottom). Shading and arrows are the same as in Figure 4.8. All terms are normalized by their maximum value at the equator.

Asia simulation.

4.6.3 Surface temperature variations

At the equator, the largest variations in the surface energy storage $\mathcal{O}_s$ occur due to fluctuations in the surface latent heat flux LH_0; the other surface fluxes vary minimally compared with variations in LH_0. LH is defined by the bulk aerodynamic formula: $LH = L\rho C_D U\,(q_s(T_s) - q)$, with latent heat of vaporization L, air density ρ, aerodynamic transfer coefficient C_D, mean near-surface wind speed U, and specific humidity of the surface and near-surface air q_s and q, respectively.

For the "all ocean" aquaplanet simulation, the variations in the surface latent heat flux follow the pattern of the magnitude of the near-surface wind speed U_0. Changes in $(q_s - q)_0$ are important as well, since they oppose the surface wind. This relationship is shown in the top panel of Figure 4.10. Even though $(q_s - q)_0$ is maximized when U_0

is at a minimum, LH_0 qualitatively follows the pattern of U_0. The equatorial surface wind speed maximizes in mid-summer just after the ITCZ crosses the equator, when the circulation becomes cross-equatorial. This is also around the time when LH_0 maximizes, cooling the surface and warming the atmosphere. LH_0 maximizes slightly earlier than the surface wind speed because of the coupling between the surface wind and the moisture gradient.

LH_0 in the Asia experiment also qualitatively follows U_0. Because there is a significant temporal asymmetry in the surface wind speed, there is also an asymmetry in LH_0. U_0 is about 60% weaker in NH spring/summer than in SH spring/summer. This leads to a much larger cooling of equatorial SSTs in SH spring than in NH spring and is the reason for the single peak structure in SST. There is also a slight difference in phasing between $(q_s - q)_0$ and U_0 between NH spring and SH spring, which causes LH_0 to be approximately constant during NH summer instead of reaching a maximum value in early summer. This phasing difference has a smaller effect than the surface wind on the equatorial cooling; if it did not occur, LH_0 would reach a smaller maximum value than in SH spring and the cooling that would result would be small compared with that in SH spring. Thus, the SST would still basically have one maximum.

Figure 4.10 does not provide information about the magnitude of the quantities plotted, so the values of LH_0 between the Asia and aquaplanet simulations cannot be compared. However, the magnitude of the latent heating that occurs in November in the Asia simulation is much larger than that in the aquaplanet simulation, which can be attributed to the stronger surface winds during SH spring in the Asia experiment than in the aquaplanet. This is why the surface temperature drops so much more in SH spring for the Asia experiment (e.g., bottom panel of Fig. 4.9).

Thus we have found that a seasonal asymmetry in the surface winds produces an asymmetry in the latent heat flux which, in turn, gives an asymmetry in the surface

temperature. In the next section, the role of the dynamics in creating this asymmetry is described.

4.6.4 Role of Dynamics

4.6.4.1 NH spring ITCZ transition

Figure 4.11 shows the seasonal averages of the meridional circulation (left column) and the MSE flux (right column) for the Asia simulation. During the NH spring EFE transition (first row), meridional temperature and moist static energy gradients are very small. This is because the temperature patterns in the NH and SH are out of phase. As shown in Figure 4.12, the SH ocean remains warm in NH spring due to its large heat capacity and at the same time the NH continent warms rapidly all the way to the pole due to its small heat capacity. Midlatitude baroclinic eddies are weak as well (Fig. 4.14), and so the meridional circulation is very weak during this time, consistent with the fact that $F_0^{net} = \partial_y \left\langle \overline{vh} \right\rangle_0 \approx 0$. The equatorial ocean experiences warming (i.e., $\mathcal{O}_{s0} > 0$) in response to solar forcing since the surface latent heat flux is small, as described in the previous section.

During the time when $F_0^{net} < 0$, the atmospheric circulation must converge energy, meaning that energy must be transported from a region of positive F^{net} towards the equator. Over the continent $F_0^{net} >> 0$, so this implies a transport from the NH continent toward the equator. This is when a double-ITCZ-like situation develops during March/April (Bischoff and Schneider 2015). A weak local (i.e., not cross-equatorial) circulation develops over the continent in response to the heating there, transporting energy southward towards the equator. Other modeling studies have observed a similar local circulation that develops prior to monsoon onset (e.g., Xie and Saiki 1999). Because our land surface is "saturated" and therefore a source of moisture, this local circulation brings the first precipitation to the continent in NH

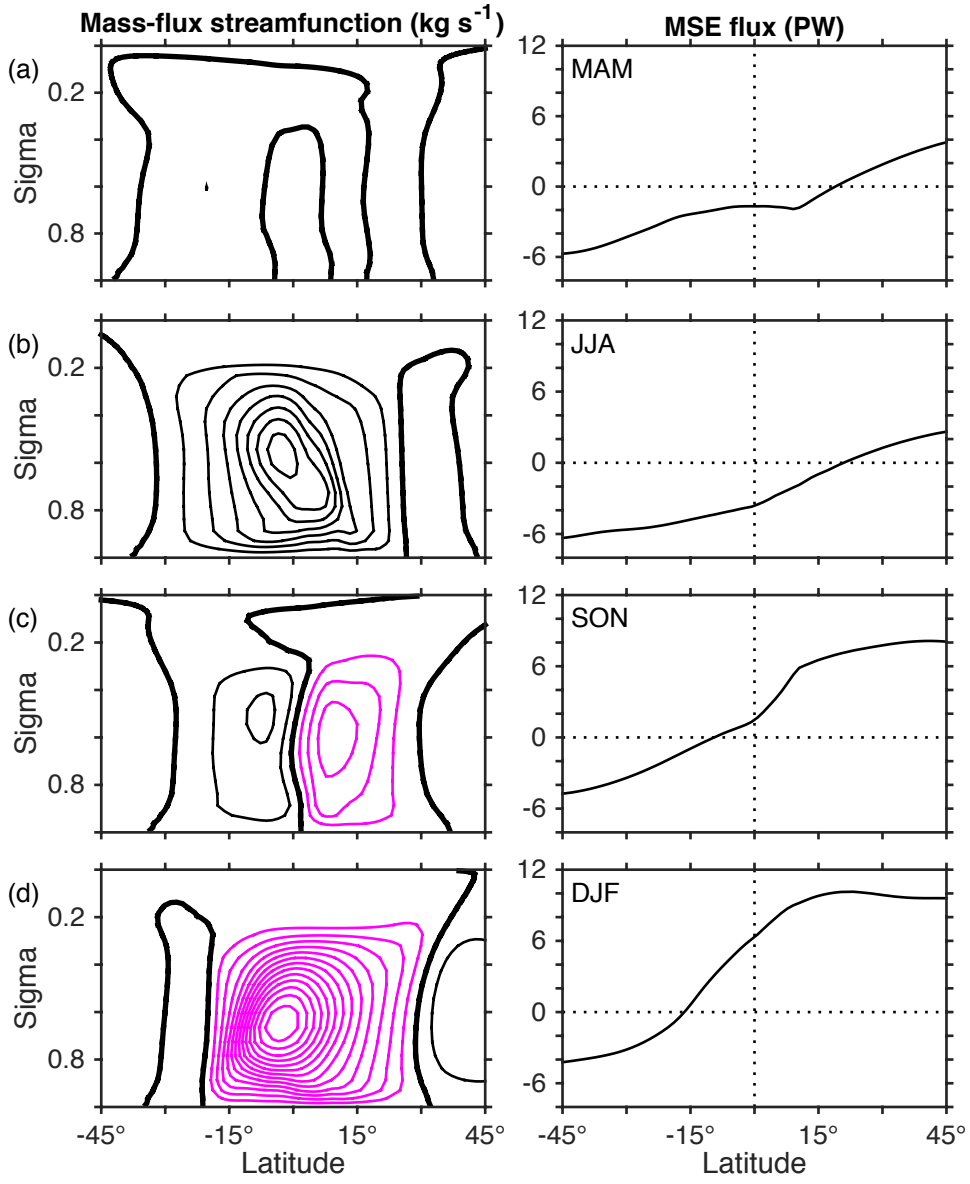

Figure 4.11: Seasonal averages of the mass-flux streamfunction (left column – contour interval 50×10^9 kg s^{-1}) and the vertically-integrated MSE flux $\langle \overline{vh} \rangle$ (right panel) for the equinox and solstice seasons in the Asia experiment: (a) MAM, (b) JJA, (c) SON, and (d) DJF. Black and magenta contours indicate counterclockwise and clockwise rotation, respectively. The heavy line in the left column indicates the zero of the streamfunction.

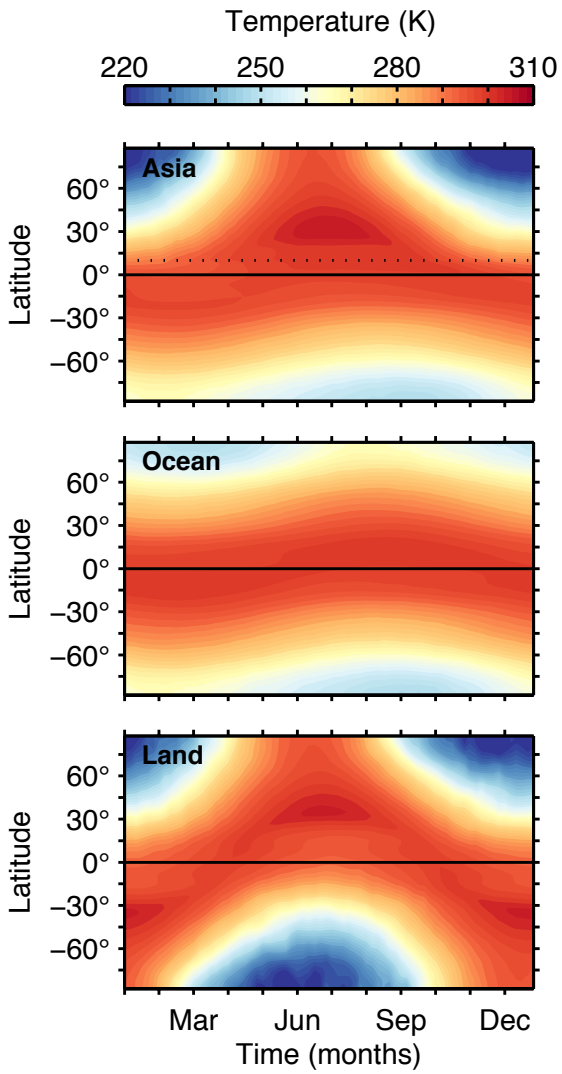

Figure 4.12: Seasonal cycle of surface air temperature for each simulation. Temperatures shown are those of the lowest model level.

spring (cf. Fig. 4.4). Figure 4.13 shows that most of the precipitation that falls in NH spring is due to evaporation rather than moisture convergence. Therefore, if surface hydrology were included in the model, there would be limited evaporation over the continent and we would expect this cell to be dry and without precipitation until sufficient moisture converges there.

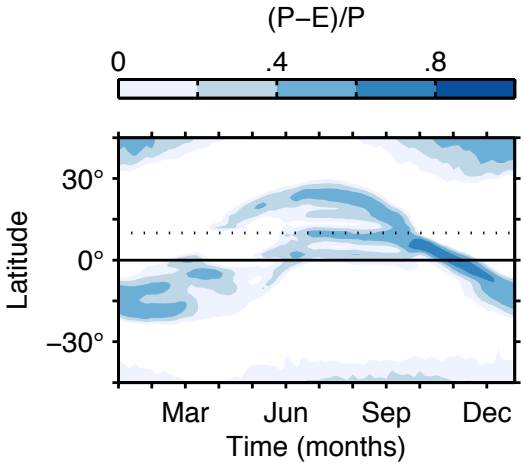

Figure 4.13: Fraction of precipitation owing to moisture flux convergence, $(P-E)/P$, for the Asia simulation. P and E are precipitation and evaporation, respectively.

4.6.4.2 SH spring ITCZ transition

The SH spring transition looks very different (third row of Fig. 4.11). During this time, the NH winter cell starts to strengthen rapidly. The continent cools off quickly, increasing the pole-equator temperature gradient and thus the baroclinic eddy activity in the NH extratropics. The strength of these eddies is linked to the strength of the Hadley circulation through the zonally-averaged zonal momentum budget $f(1-\mathrm{Ro})\bar{v} \approx \mathcal{S}$, with Coriolis parameter f, local Rossby number $\mathrm{Ro} = -\bar{\zeta}/f$, relative vorticity ζ and eddy momentum flux divergence $\mathcal{S} = \partial_y(\overline{u'v'}\cos\phi)$. Figure 4.14 shows the vertically-integrated eddy momentum flux divergence (EMFD) as a function of time and latitude for all three simulations. For Asia (top panel), the EMFD increases rapidly in SH spring over the continent and the circulation strengthens linearly with it until SH winter, which is when the cell becomes more constrained by the energy budget (Bordoni and Schneider 2008; Schneider and Bordoni 2008).

Also during this time, the atmospheric energy transport begins to increase rapidly (cf. Fig. 4.8). This implies that more energy is being transported from the SH to the NH as this cell strengthens and moves further into the SH.

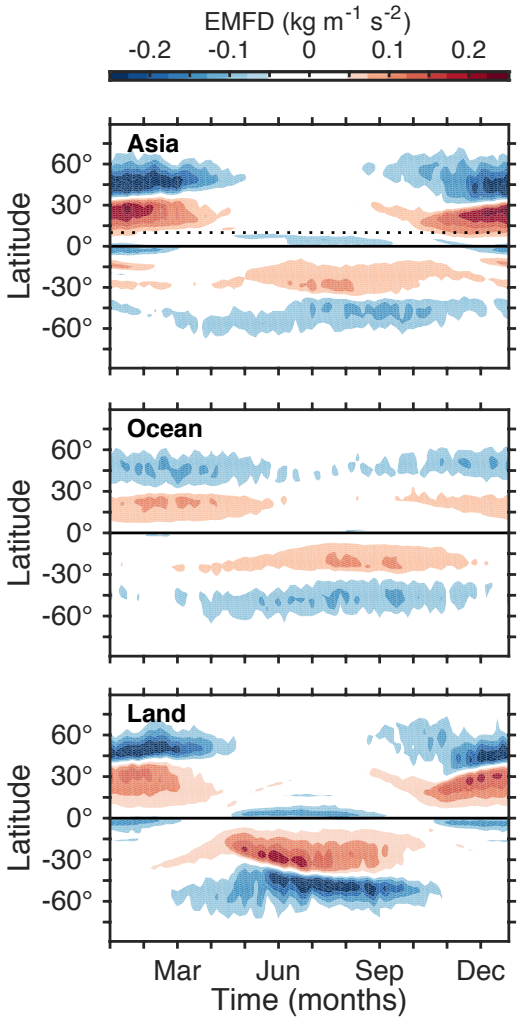

Figure 4.14: Vertically-integrated EMFD $\left\langle \partial_y(\overline{u'v'}\cos\phi)\right\rangle$ (kg m^{-1} s^{-2}) versus latitude and time for the three simulations.

The rapid strengthening of the circulation produces stronger surface winds and thus stronger surface heat fluxes from the ocean to the atmosphere. These fluxes cool the surface ocean and increase F^{net} in the equatorial region, making it relatively difficult to shift the EFE (and ITCZ) position. As a result, austral summer is characterized by a gradually-shifting monsoonal circulation that is about twice as strong as that in boreal summer (compare bottom row with second row), but migrates only 13° from the equator on average.

4.6.5 NH monsoon onset

Figure 4.15 shows the formation and evolution of a local cell at the continent edge at day 100 (i.e., in April). The development of this circulation is associated with a small and negative F^{net} in the tropics, indicating that energy needs to be transported towards the equator.

As the SH begins to cool and the pole-equator temperature gradient strengthens there, midlatitude baroclinic eddies drive a weak circulation in the SH subtropics. Thus around day 120 there are actually two separate cells that are rotating in the same sense, which can be seen in the second row of Figure 4.15. This southern cell is the source of the other band of precipitation that does not cross the equator until June (cf. Fig. 4.4).

These two circulations coexist and eventually merge during summer, forming one cross-equatorial monsoonal cell that transports energy southward. The merging of the two cells occurs as a negative absolute vorticity gradient develops in the upper troposphere over the continent around day 135 (right panel of Fig. 4.15). Such a rapid onset of a monsoonal circulation is similar to that described by Plumb and Hou (1992) and Emanuel (1995) for axisymmetric atmospheres, and can only occur when the low-level moist entropy gradients exceed a threshold value.

4.7 Discussion

4.7.1 Relation to other theories

In the literature, it has been suggested that the ITCZ position is linearly proportional to the cross-equatorial energy flux (e.g., Donohoe et al. 2013). In the Asia simulation, the magnitude of the cross-equatorial atmospheric energy flux is larger in DJF than in JJA (Fig. 4.5). Thus, under the assumption that $\delta \sim \left\langle \overline{vh} \right\rangle_0$, the ITCZ

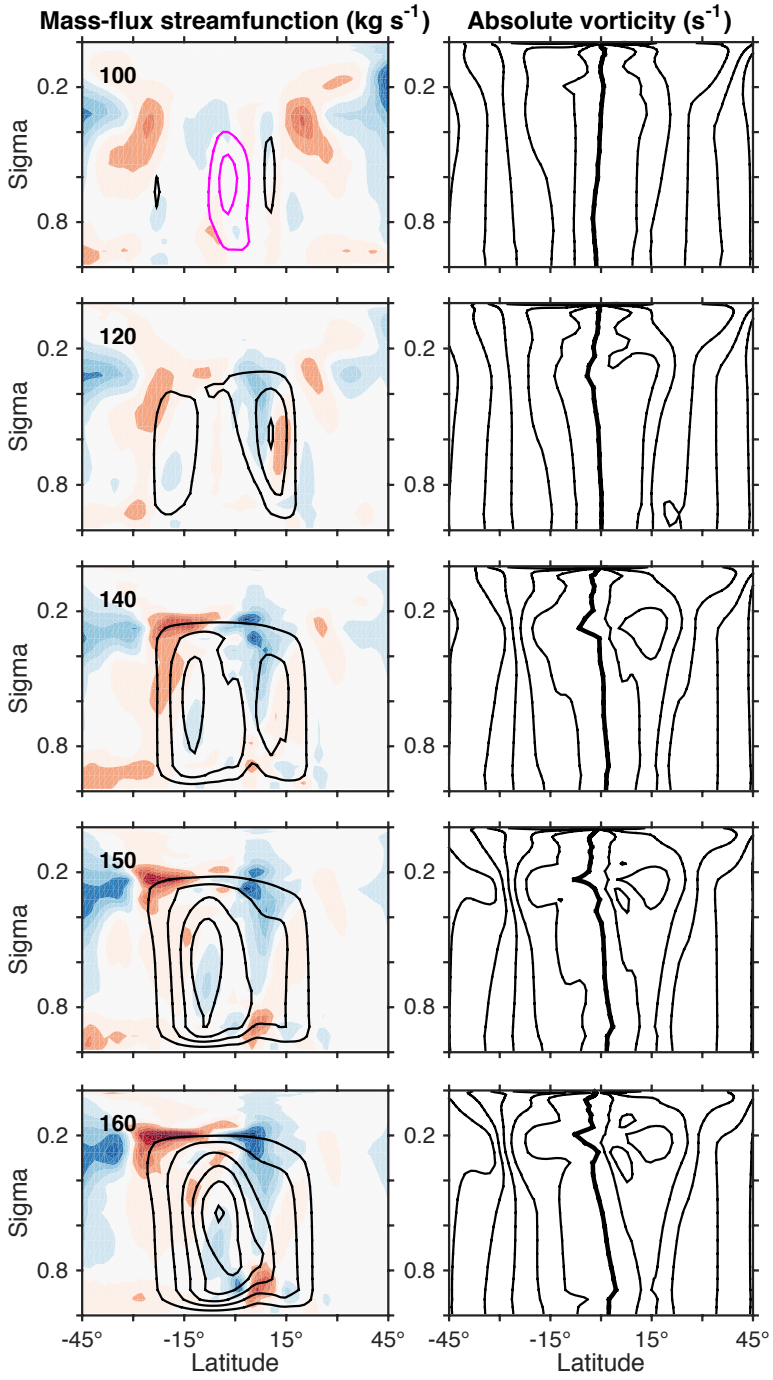

Figure 4.15: Left column: Eddy momentum flux divergence $\mathrm{div}(u'v'\cos\phi)$ (colors, contour interval 0.6×10^{-5} m s^{-2}) and mass-flux streamfunction (contours, contour interval 50×10^{9} kg s^{-1}, with black contours for counterclockwise and magenta contours for clockwise rotation). Right column: Absolute vorticity $\zeta_a = f + \zeta$ (contour interval 2×10^{-5} s^{-1}). Five pentads are shown, with the day number indicated in the top left corner of the left column. For reference, day 91 corresponds to April 1.

should be located further poleward in DJF than in JJA, but that is not what we see. In fact, the JJA ITCZ is 8° further poleward. This means that, at least in an idealized setting such as this one, seasonal changes of F_0^{net} (and specifically surface energy storage) matter for setting the ITCZ location. This also implies that the energy transport by the Hadley circulation is larger in DJF than in JJA, even though the cell itself is smaller in extent. This is in disagreement with axisymmetric theories of cross-equatorial Hadley cells (Lindzen and Hou 1988), albeit not very surprising since these axisymmetric models have fixed meridional pole-equator temperature gradients and static stability.

In the Asia case, it is the ocean energy storage that can close the gap between $\mathcal{S}_0 - \mathcal{L}_0$ and zero, causing $\partial_y \left\langle \overline{vh} \right\rangle_0$ to become very small[2]. This can only happen if there is a large surface heat capacity at the equator. Otherwise, theoretically there could be the same surface temperature pattern, but no ocean energy storage. In this case, there would still be a temporal asymmetry in F_0^{net} due to $\mathcal{L}_0$, but F_0^{net} would not be as temporally asymmetric and it would not go to zero. In this hypothetical case, $F_0^{net} \approx \mathcal{S}_0 - \mathcal{L}_0$ would be the denominator of the EFE position δ, and it would still be larger in DJF than in JJA (cf. Fig. 4.9), which by itself would have the effect of shifting the ITCZ poleward in JJA and equatorward in DJF, just like in the Asia experiment. During the monsoon onset it would also have the same effect, $\mathcal{S}_0 - \mathcal{L}_0$ is smaller for NH monsoon onset than for SH monsoon onset (cf. Fig. 4.9, blue arrows).

4.7.2 Comparison to observations and CMIP5

While very idealized, the results from our simulations bear resemblance to the seasonal cycle of precipitation in the Indian monsoon sector. Figure 4.16 shows the seasonal cycle of precipitation from TRMM daily data (top panel) and the CMIP5

[2]Note that in our idealized experiments, $\mathcal{O}_0$ is prescribed and constant in time. Therefore we omit it from this discussion of a hypothetical experiment.

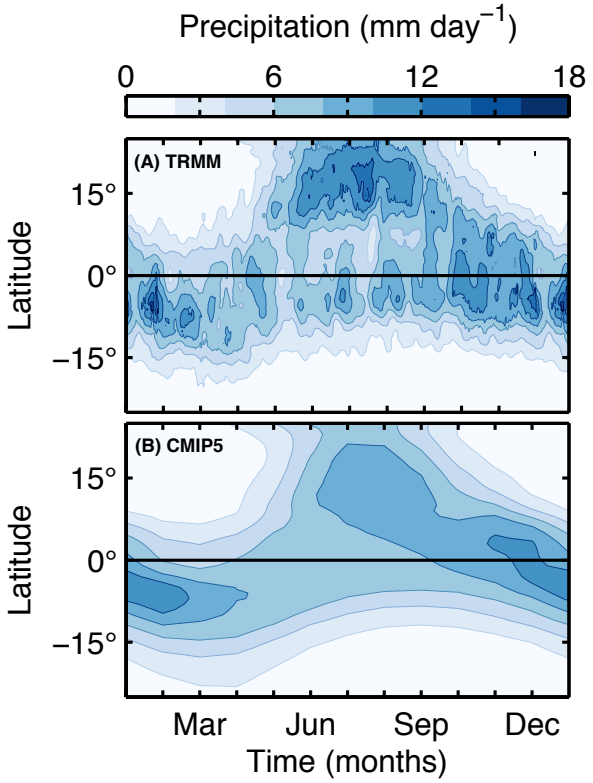

Figure 4.16: Seasonal cycle of precipitation (mm day^{-1}) for the Indian monsoon sector (70°E-110°E) from (a) TRMM daily observations from 1998-2012 and (b) multi-model mean of CMIP5 data.

(Coupled Model Intercomparison Project Phase 5) multi-model-mean (bottom panel) in the Indian monsoon sector (here taken to be 70°E-110°E). Obviously there are many complexities in the real climate system that are also included in the comprehensive GCMs in CMIP5, but the precipitation pattern looks similar to what we see in our idealized GCM. The peak rainfall jumps rather abruptly from near the equator to the northern hemisphere in May, but retreats back into the SH more gradually (e.g., Lau and Yang 1996).

It is interesting that even in the absence of many radiative and land surface feedbacks, simulations that crudely account for the surface heat capacity distribution associated with land-sea contrast reproduce similar patterns of precipitation. By focusing on fundamental mechanisms responsible for changes in the monsoonal cir-

culation and precipitation, it is expected that this work can provide insight into and more robustly constrain present-day simulations (and possibly future projections) of Earth's monsoons by state-of-the-art climate models in the CMIP5 archive.

4.8 Conclusions

This work illustrates that both spatial and temporal symmetry breaking of monsoonal precipitation patterns can occur in an idealized model with hemispherically asymmetric continental geometry.

The spatial symmetry is broken because of the hemispheric energy imbalance imposed by the asymmetry in surface heat capacity. Interestingly, the ITCZ migrates *further* poleward in JJA, even though the cross-equatorial energy transport is maximized in DJF. This seems at odds with previous work that has correlated the ITCZ position to the cross-equatorial energy transport. But, as discussed by Bischoff and Schneider (2014), this occurs because the net energy input to the equatorial atmosphere F_0^{net} dictates how sensitive the ITCZ position is to changes in the cross-equatorial energy transport, and in our simulations of seasonal cycles is smaller in JJA than in DJF.

The symmetry breaking in time is also due to the temporal difference in F_0^{net}. We found that the dynamics force a different response from the surface energy budget in the two different time periods. In NH spring, the circulation is very weak both because eddy activity is weak and because the ocean can store heat, which allows F^{net} to become very small in the tropics. This allows for abrupt shifts in the ITCZ location (when the linear approximation holds) and/or double-ITCZ phenomena (when the linear approximation breaks down). In the SH spring, eddy activity over the continent is strong, causing the circulation there to strengthen. The increased surface winds influence surface latent heat fluxes, which cool the ocean and warm the atmosphere.

This increases F^{net} in the tropics, making it more difficult to shift the ITCZ and resulting in a more gradual progression of the ITCZ.

Here we consider the true "monsoon onset" to be the development of a deep cross-equatorial circulation, which does not occur until June, well after the ITCZ crosses the equator. Future work will include a more realistic representation of land, with consideration of surface hydrology. We hypothesize that including these factors would suppress the ITCZ jumping across the equator in April (i.e., the double-ITCZ feature), and that the ITCZ progression in NH spring would match the monsoon onset.

One of the prominent open issues that remains is the reconciliation of the precipitation seasonality with the energetic framework. While useful to understand important features of the ITCZ seasonal cycle, the energetic framework fails to provide a quantitative argument for the ITCZ position because of significant discrepancies between the EFE and the ITCZ in this and other models (Donohoe et al. 2013; Chamales et al. 2015). Understanding the causes of these discrepancies could be a useful starting point. Additionally, as discussed by several previous papers, the energy framework constrains the energy transport, which is linked to the mass transport (more directly constrained by the momentum budget) through the GMS. In our simulations, there are times in the course of the seasonal cycle when the energy and the mass transports have different signs, implying a negative GMS with ITCZ and EFE positions that are on opposite sides of the equator. The GMS remains a poorly constrained quantity, for which closed theories have yet to emerge. It is also intriguing that the eddy EFE tracks the ITCZ position remarkably well, even better than the mean EFE. Further investigation of the seasonal cycles of these quantities will shed light on the applicability of this energetic framework to the seasonal cycle of precipitation.

Chapter 5

Conclusions

Here I briefly summarize conclusions and open questions from this thesis.

Janssen et al. (2013) (Appendix A) used 2.2-cm brightness temperature observations of Saturn to produce residual brightness temperature maps for five dates between 2005 and 2011. In Chapter 2 I interpreted these maps by making adjustments to the vertical ammonia distribution using the JAMRT radiative transfer program. We found that ammonia vapor must be depleted below the cloud base in some regions in order to obtain temperatures in agreement with observations. The depletion must extend to 2 bars or deeper for brightness temperatures greater than 160 K. To obtain these results, we assume that Saturn's latitudinal temperature profile is constant in our sensitivity range of 0.5-2 bars. The highest brightness temperatures we see are in the 2010-2011 northern storm and in the subtropical latitudes of the October 2009 map. The most striking feature, evident in Fig. 2.9, is the difference in the 2.2-cm brightness temperature right at the equator versus that just off the equator. We suspect that atmospheric dynamics plays a role in setting the ammonia distribution in the tropics.

We presented a couple possible explanations for the brightness temperature pattern observed at 2.2-cm. One option is that large-scale upwelling and downwelling, like the Earth's Hadley circulation, for example, creates dry zones like the subtropics of Earth. Another option is that the drying is an intrinsic property of convection in

giant planet atmospheres, and that it applies not just to the small southern lightning storms but also to the northern storm of 2010-2011. The subtropical dry bands are not copious producers of lightning and moist convection, so this might not apply there. It may be that that the meridional circulation explanation applies to the subtropics, and the deep convection explanation applies to the lightning storms.

Modeling of atmospheric circulations on giant planets has proven difficult, and the lack of observational data in the deep atmosphere below the clouds is a limitation. It is important to try to reconcile the atmospheric motions with latitudinal distributions of tropospheric gases such as NH_3 and PH_3. This chapter provides some insight into the distribution of ammonia vapor, with the hope that more work can be done with these observations to reconcile them with the energy and momentum balances of Saturn's atmosphere.

In Chapter 3, simulations and a scaling theory that establish conditions under which superrotation occurs in terrestrial atmospheres are presented. By varying the planetary rotation rate, the pole-equator temperature contrast in radiative equilibrium, and a scaling parameter for the convective lapse rate, we generated a wide range of atmospheric flows, some superrotating and some subrotating.

The theory presented in this chapter hinges on a simple idea going back to Saravanan (1993) that there are two competing sources for eddy angular momentum flux convergence at the equator. The first is a source at the equator: Rossby waves generated by convective heating fluctuations. As these waves dissipate away from the equator, they converge angular momentum into the equatorial region, increasing the propensity for superrotation. The other source is baroclinic instability in midlatitudes, which generates Rossby waves in midlatitudes that dissipate farther equatorward, thus extracting momentum from lower latitudes. This mechanism decreases the propensity for superrotation. Quantifying the magnitude of the two mechanisms, introducing their nondimensional ratio S_r, and developing a scaling for it in terms

of mean-flow quantities leads to our theory and sheds light on the conditions under which superrotation occurs. Our simulation results and scaling theory show that:

i. Superrotation occurs when the eddy angular momentum flux convergence associated with equatorial wave activity generation exceeds eddy angular momentum flux divergence near the equator produced by midlatitude baroclinic eddies (i.e., $S_r > 1$).

ii. Superrotation is favored for low planetary rotation rates and/or strong diabatic heating.

iii. Superrotation is favored when midlatitude baroclinicity is weak.

The S_r parameter only signifies whether or not an atmosphere will be superrotating, based on the atmospheric mean flow parameters. It does not say anything about how strong or weak an atmosphere's superrotation will be. Curiously, increasing S_r beyond $S_r \sim 1$ by decreasing Δ_h actually weakens the superrotation. More work must be done to investigate the reasons for this reversal in behavior beyond the $S_r \sim 1$ threshold.

Finally, in Chapter 4 an idealized GCM was used to study asymmetric precipitation patterns in an aquaplanet with a zonally-symmetric continent. We found the seasonal progression of the ITCZ in our idealized experiment to be roughly consistent with that observed in the Indian monsoon sector, with a somewhat abrupt transition from the southern to the northern hemisphere in NH spring, and a smoother and more gradual retreat back into the SH.

We found the large-scale atmospheric energy budget useful in explaining the seasonally-averaged hemispheric asymmetry in the ITCZ position. Even though more energy is transported across the equator in SH summer, the ascending branch of the monsoonal circulation lies equatorward of that in NH summer. This conclusion is

in disagreement with previous work that correlates the ITCZ position to the cross-equatorial energy transport. This discrepancy can be explained by the net energy input to the equatorial atmosphere, which changes significantly between the two seasons and alters the dependence of the ITCZ position on the cross-equatorial energy transport.

The timing of ITCZ shifts and monsoon onset/retreat was also examined. However, more work must be done to understand how the energetic framework can be applied to the seasonal progression of precipitation, given that there is a disparity between the EFE and ITCZ, with a lag of $\approx$ 30 days between them for the Asia experiment. We found that the net energy input to the equatorial atmosphere varies significantly throughout the seasonal cycle of simulations with ocean at the equator.

There is much interest in determining how the spatial and temporal distribution of precipitation associated with monsoons will change with climate. Thus it would be interesting to use this idealized GCM to study how the idealized monsoonal circulation responds to greenhouse gas forcing. By focusing on fundamental dynamical and thermodynamical mechanisms responsible for changes in the monsoonal circulation and precipitation, it is expected that this work might provide insight into and might more robustly constrain future projections of Earth's monsoons by state-of-the-art climate models in the CMIP5 archive.

Bibliography

Adam, O., T. Bischoff, and T. Schneider, 2015: The energy flux equator and the positions of the intertropical convergence zones in present climate. *Journal of climate (submitted)*.

Back, L. E. and C. S. Bretherton, 2009: On the relationship between sst gradients, boundary layer winds, and convergence over the tropical oceans. *Journal of Climate*, **22 (15)**, 4182–4196.

Bischoff, T. and T. Schneider, 2014: Energetic constraints on the position of the intertropical convergence zone. *Journal of Climate*, **27 (13)**, 4937–4951.

Bischoff, T. and T. Schneider, 2015: The equatorial energy balance, itcz position, and double itcz bifurcations. *Journal of climate (submitted)*.

Bordoni, S., 2007: On the role of eddies in monsoonal circulations: Observations and theory. Ph.D. thesis, University of California, Los Angeles.

Bordoni, S. and T. Schneider, 2008: Monsoons as eddy-mediated regime transitions of the tropical overturning circulation. *Nature Geoscience*, **1 (8)**, 515–519, doi: 10.1038/ngeo248.

Caballero, R. and M. Huber, 2010: Spontaneous transition to superrotation in warm climates simulated by CAM3. *Geophysical Research Letters*, **37 (11)**, doi:10.1029/2010GL043468.

Chamales, K. A., A. C. Clement, S. Bordoni, and L. N. Murphy, 2015: The effects of orbital precession on tropical precipitation: Mechanisms controlling precipitation changes over land and ocean. *Geophys. Res. Lett. (submitted).*

Chou, C., J. D. Neelin, and H. Su, 2001: Ocean-atmosphere-land feedbacks in an idealized monsoon. *Quarterly Journal of the Royal Meteorological Society*, **127**, 1869–1891.

Donohoe, A., J. Marshall, D. Ferreira, and D. Mcgee, 2013: The relationship between itcz location and cross-equatorial atmospheric heat transport: from the seasonal cycle to the last glacial maximum. *Journal of Climate*, **26 (11)**, 3597–3618.

Emanuel, K. A., 1995: On thermally direct circulations in moist atmospheres. *Journal of the atmospheric sciences*, **52 (9)**, 1529–1534.

Frierson, D. M., I. M. Held, and P. Zurita-Gotor, 2006: A gray-radiation aquaplanet moist gcm. part i: Static stability and eddy scale. *Journal of the atmospheric sciences*, **63 (10)**, 2548–2566.

Frierson, D. M. and Y.-T. Hwang, 2012: Extratropical influence on itcz shifts in slab ocean simulations of global warming. *Journal of Climate*, **25 (2)**, 720–733.

Frierson, D. M., et al., 2013: Contribution of ocean overturning circulation to tropical rainfall peak in the northern hemisphere. *Nature Geoscience*, **6 (11)**, 940–944.

Frierson, D. M. W., 2007: The Dynamics of Idealized Convection Schemes and Their Effect on the Zonally Averaged Tropical Circulation. *Journal of the Atmospheric Sciences*, **64 (6)**, 1959–1976, doi:10.1175/JAS3935.1.

Held, I. M. and A. Y. Hou, 1980: Nonlinear axially symmetric circulations in a nearly inviscid atmosphere. *Journal of the Atmospheric Sciences*, **37**, 515–533.

Janssen, M., et al., 2013: Saturns thermal emission at 2.2-cm wavelength as imaged by the Cassini RADAR radiometer. *Icarus*, **226 (1)**, 522–535, doi:10.1016/j.icarus.2013.06.008.

Kang, S. M., I. M. Held, D. M. Frierson, and M. Zhao, 2008: The response of the itcz to extratropical thermal forcing: Idealized slab-ocean experiments with a gcm. *Journal of Climate*, **21 (14)**, 3521–3532.

Lau, K. and S. Yang, 1996: Seasonal variation, abrupt transition, and intraseasonal variability associated with the asian summer monsoon in the gla gcm. *Journal of Climate*, **9 (5)**, 965–985.

Lindzen, R. S. and A. Y. Hou, 1988: Hadley Circulations for Zonally Averaged Heating Centered off the Equator. *Journal of the Atmospheric Sciences*, **45 (17)**, 2416–2427.

Lindzen, R. S. and S. Nigam, 1987: On the role of sea surface temperature gradients in forcing low-level winds and convergence in the tropics. *Journal of the Atmospheric Sciences*, **44 (17)**, 2418–2436.

Marshall, J. and R. Plumb, 2007: *Atmosphere, Ocean and Climate Dynamics: An Introductory Text*. International Geophysics, Elsevier Science, URL `https://books.google.com/books?id=KvJfvYBHiegC`.

Merlis, T. M., T. Schneider, S. Bordoni, and I. Eisenman, 2013: Hadley Circulation Response to Orbital Precession. Part I: Aquaplanets. *Journal of Climate*, **26 (3)**, 740–753, doi:10.1175/JCLI-D-11-00716.1.

Neelin, J. D., 2007: Moist dynamics of tropical convection zones in monsoons, teleconnections, and global warming. Princeton University Press, 267–301 pp.

O'Gorman, P. A. and T. Schneider, 2008: The hydrological cycle over a wide range of climates simulated with an idealized gcm. *Journal of Climate*, **21 (15)**.

Plumb, R. A. and A. Y. Hou, 1992: The Response of a Zonally Symmetric Atmosphere to Subtropical Thermal Forcing: Theshold Behavior. *Journal of the Atmospheric Sciences*, **49 (19)**, 1790–1799.

Privé, N. C. and R. A. Plumb, 2007a: Monsoon Dynamics with Interactive Forcing. Part I: Axisymmetric Studies. *Journal of the Atmospheric Sciences*, **64 (5)**, 1417–1430, doi:10.1175/JAS3916.1.

Privé, N. C. and R. A. Plumb, 2007b: Monsoon Dynamics with Interactive Forcing. Part II: Impact of Eddies and Asymmetric Geometries. *Journal of the Atmospheric Sciences*, **64 (5)**, 1431–1442, doi:10.1175/JAS3917.1.

Schneider, T., 2006: The General Circulation of the Atmosphere. *Annual Review of Earth and Planetary Sciences*, **34 (1)**, 655–688, doi:10.1146/annurev.earth.34.031405.125144.

Schneider, T., T. Bischoff, and G. H. Haug, 2014: Migrations and dynamics of the intertropical convergence zone. *Nature*, **513 (7516)**, 45–53.

Schneider, T. and S. Bordoni, 2008: Eddy-Mediated Regime Transitions in the Seasonal Cycle of a Hadley Circulation and Implications for Monsoon Dynamics. *Journal of the Atmospheric Sciences*, **65 (3)**, 915–934, doi:10.1175/2007JAS2415.1.

Schneider, T., P. A. OGorman, and X. J. Levine, 2010: Water Vapor and the Dynamics of Climate Changes. *Reviews of Geophysics*, **48 (2009)**, 1–22, doi:10.1029/2009RG000302.1.INTRODUCTION.

Shaw, T. a., 2014: On the role of planetary-scale waves in the abrupt seasonal tran-

sition of the Northern Hemisphere general circulation. *Journal of the Atmospheric Sciences*, **In press**, doi:10.1175/JAS-D-13-0137.1.

Sobel, A. H., 2007: Simple models of ensemble-averaged precipitation and surface wind, given the sea surface temperature. *The Global Circulation of the Atmosphere, edited by T. Schneider and AH Sobel*, 219–251.

Sperber, K. R., H. Annamalai, I.-S. Kang, A. Kitoh, A. Moise, A. Turner, B. Wang, and T. Zhou, 2013: The asian summer monsoon: an intercomparison of cmip5 vs. cmip3 simulations of the late 20th century. *Climate dynamics*, **41 (9-10)**, 2711–2744.

Walker, C. C. and T. Schneider, 2006: Eddy Influences on Hadley Circulations: Simulations with an Idealized GCM. *Journal of the Atmospheric Sciences*, **63 (12)**, 3333–3350, doi:10.1175/JAS3821.1.

Webster, P. J. and J. Fasullo, 2003: Monsoon Dynamical Theory. *Encyclopedia of Atmospheric Sciences*, 1370–1386.

Xie, S.-P. and N. Saiki, 1999: Abrupt Onset and Slow Seasonal Evolution of Summer Monsoon in an Idealized GCM Simulation. *Journal of the Meteorological Society of Japan*, **77 (4)**, 949–968.

Young, J. A., 1987: Physics of monsoons: The current view. *Monsoons: New York, John Wiley and Sons*, 211–243.

Appendix A

Saturn's thermal emission at 2.2-cm wavelength as imaged by the Cassini RADAR radiometer

[0]Reprinted from Elsevier. Formal publication located at doi:10.1016/j.icarus.2013.06.008

Icarus 226 (2013) 522–535

Contents lists available at SciVerse ScienceDirect

Icarus

journal homepage: www.elsevier.com/locate/icarus

Saturn's thermal emission at 2.2-cm wavelength as imaged by the Cassini RADAR radiometer

M.A. Janssen [a,*], A.P. Ingersoll [b], M.D. Allison [c], S. Gulkis [a], A.L. Laraia [b], K.H. Baines [a], S.G. Edgington [a], Y.Z. Anderson [a], K. Kelleher [a], F.A. Oyafuso [a]

[a] Jet Propulsion Laboratory, California Institute of Technology, Pasadena, CA, 91109, United States
[b] California Institute of Technology, Pasadena, CA, 91125, United States
[c] NASA Goddard Institute for Space Studies, New York, NY, 10025, United States

ARTICLE INFO

Article history:
Available online 21 June 2013

Keywords:
Saturn, Atmosphere
Atmospheres, Structure
Atmospheres, Composition
Radiative transfer
Radio observations

ABSTRACT

We present well-calibrated, high-resolution maps of Saturn's thermal emission at 2.2-cm wavelength obtained by the Cassini RADAR radiometer through the Prime and Equinox Cassini missions, a period covering approximately 6 years. The absolute brightness temperature calibration of 2% achieved is more than twice better than for all previous microwave observations reported for Saturn, and the spatial resolution and sensitivity achieved each represent nearly an order of magnitude improvement. The brightness temperature of Saturn in the microwave region depends on the distribution of ammonia, which our radiative transfer modeling shows is the only significant source of absorption in Saturn's atmosphere at 2.2-cm wavelength. At this wavelength the thermal emission comes from just below and within the ammonia cloud-forming region, and yields information about atmospheric circulations and ammonia cloud-forming processes. The maps are presented as residuals compared to a fully saturated model atmosphere in hydrostatic equilibrium. Bright regions in these maps are readily interpreted as due to depletion of ammonia vapor in, and, for very bright regions, below the ammonia saturation region. Features seen include the following: a narrow equatorial band near full saturation surrounded by bands out to about 10° planetographic latitude that demonstrate highly variable ammonia depletion in longitude; narrow bands of depletion at −35° latitude; occasional large oval features with depleted ammonia around −45° latitude; and the 2010–2011 storm, with extensive saturated and depleted areas as it stretched halfway around the planet in the northern hemisphere. Comparison of the maps over time indicates a high degree of stability outside a few latitudes that contain active regions.

1. Introduction

The thermal emission from the gas giant planets was first observed by single-antenna telescopes in the 1950s (Mayer et al., 1958), and quantitatively related to fundamental atmospheric properties in the following decade (Thornton and Welch, 1963; Gulkis et al., 1969; Wrixon and Welch, 1970). Subsequent observations through the 1980s filled in the disk-temperature spectra of Jupiter and Saturn through the millimeter- and centimeter-wavelength range. This combined with advances in understanding the high-pressure microwave absorption of ammonia, which possesses a strong inversion band just longward of 1-cm wavelength, led to a consistent story of deeply convective atmospheres with ammonia as the dominant absorber (Gulkis and Poynter, 1972; Berge and Gulkis, 1976; Klein and Gulkis, 1978). The whole disk spectrum through the microwave region for Saturn led to a value for the deep atmosphere mixing ratio of ammonia of about three times the solar abundance, value consistent with previous work (de Pater, 1990; Atreya, 2010), and our analysis in L13. The measured disk temperature spectrum of Saturn may be found in de Pater and Massie (1985) and van der Tak et al. (1999).

The advent around the same time of radio interferometers capable of using aperture synthesis to image the planets led to the first microwave image of Saturn, reported by Schloerb et al. (1979) using the interferometer Owens Valley Radio Observatory at 3.7-cm wavelength. The completion of the National Radio Astronomical Observatory's Very Large Array in New Mexico was followed by a series of images of Saturn and its rings made with this instrument reported by a number of authors at wavelengths ranging from 2- to 21-cm wavelength (e.g., de Pater and Dickel, 1982, 1991; Grossman et al., 1989; Grossman, 1990). These studies have resulted in a better understanding of Saturn's rings and atmospheric microwave spectrum, and have provided evidence of large-scale structure in Saturn's ammonia distribution including variable broad bands in the midlatitudes. However, they have been

* Corresponding author. Fax: +1 818 354 8895.
E-mail address: michael.a.janssen@jpl.nasa.gov (M.A. Janssen).

0019-1035/$ - see front matter © 2013 Elsevier Inc. All rights reserved.
http://dx.doi.org/10.1016/j.icarus.2013.06.008

Table 1
Nominal radiometer characteristics.

Frequency	13.78 GHz
Wavelength	2.18 cm
Polarization	One linear
Radiometer bandpass	135 MHz
Measurement noise	0.026 K/$\sqrt{}$Hz
Beam full width at half-power (beam 3)	0.36° Circular

limited by the capabilities of the VLA in spatial resolution and dynamic range for imaging extended objects, in addition to which the process of Earth-rotational aperture synthesis used for imaging averages out longitudinal structure. The theoretical capability for the synthesized beam of the VLA in its largest (D) configuration is 1.3″ at 2-cm wavelength, providing spatial resolution on Saturn comparable to that achieved here (1° latitude at the equator). However, results published to date show actual spatial resolutions achieved to be 6° or greater in latitude (e.g., Grossman et al., 1989; van der Tak et al., 1999; Dunn et al., 2002).

The presence of a microwave radiometer in orbit around Saturn provides a unique opportunity to image Saturn with the advantage of close range and without the limitations of a ground-based approach. In this paper we present global maps of Saturn obtained over the course of the Cassini prime and equinox missions by the radiometer that is incorporated into the Cassini RADAR instrument. The emphasis in this paper is to describe the observations, the mapping approach, and overall interpretations. We describe the observational approach and calibration in the next section. In Section 3 we concentrate on the generation of the maps and their interpretation in terms of the ammonia distribution, followed by a discussion of the nature and magnitude of residual errors in the maps. We pay particular attention to the latter since the mapping approach is unique. In Section 4 we offer a discussion and general interpretation of the features seen in the maps, leaving a more detailed discussion of the broader implications to a companion paper by Laraia et al. (2013), henceforth referred to as L13.

2. Observations

2.1. The Cassini radiometer

The Cassini RADAR instrument includes a radiometer that obtains measurements of externally generated (passive) radiation entering the receiver in all operating modes of the instrument, including the various radar modes during which internally-generated (active, or radar) signals are transmitted (Elachi et al., 2004; West et al., 2009; Janssen et al., 2009). The overall characteristics of the radiometer are given in Table 1. The RADAR instrument operates in repetitive "burst" cycles, in which each cycle is divided into active (radar transmit/receive) and passive (radiometer) segments. The radiometer segment employs a Dicke-switching technique in which the noise power received through the antenna is compared with that from an internal reference blackbody termination using a microwave switch to select either the external (sky) signal or an internal reference, using the comparison to stabilize the sky signal. In general operation a second switch is used to select among an array of five antenna feeds; e.g., cycling through these enable synthetic aperture radar observations to be obtained in a wide swath. The duration of the transmit/receive period is adjustable, as are the number and duration of the radiometer averaging intervals. In the Saturn observations we used a 1-s duration burst cycle in which the active segment was eliminated and the antenna was set to the central (and smallest) radar beam, beam 3. The radiometric segment was expanded to observe the target for the entire 1-s period except for a 25 ms integration on the reference load in each cycle, These choices provided the beamwidth and sensitivity given in Table 1.

2.2. Observational approach

The RADAR radiometer was used to observe Saturn during five equatorial periapsis passes occurring between 2005 and 2011 for the purpose of mapping its 2.2-cm thermal emission. The dates and general orbital parameters for these observations are given in Table 2, and details helpful for the interpretation of the maps are given in Table 3. The observations were centered approximately on the periapsis of each pass in order to obtain the best achievable spatial resolution, which is important given that the 0.36° beamwidth of the radiometer is large compared to the resolutions of typical imaging instruments. Saturn presents a challenge comparable to that of Titan for mapping and calibration – it is an extended source that requires a large number of individual observations to build an image, each of which must be corrected for gain and baseline drift as well as signal contamination by sidelobe contributions. The approach developed for Titan for calibration and sidelobe contribution removal was carried over directly to Saturn and is described further below. The actual mapping strategy was necessarily different than the raster scanning and long-term mosaicking approach used on Titan, however, because of the different spacecraft trajectories relative to the target and Saturn's rapidly changing surface structure. Our approach for Saturn was to scan repetitively from pole to pole through Saturn's nadir as rapidly as practical as the spacecraft moved along its trajectory through periapsis, letting the motion of the spacecraft combined with Saturn's rotation provide the westward longitudinal component of the scan. Each scan took from five to ten minutes depending on range, during which time the subspacecraft longitude increased somewhat more than a beamwidth. This led to a spatial asymmetry in sampling discussed further below. Fig. 1 shows both the scan pattern of the beam axis in inertial space as it progressed with time, and as a track on the surface of Saturn, where we take the December 2009 pass as an example (the underlying map is derived from the data as described later in this paper). The gap at approximately 11 h (25° west longitude in the lower panel) was caused by the need to unload the spacecraft momentum wheels. In the lower

Table 2
Mapping orbit characteristics.

Date	Start time (UT)	Segments	Mapping duration (h)	S/C orbit inclination relative to Saturn (°)	Ring plane crossing longitude (°W Lon.)	Periapsis	
						Distance (R_S)	Saturn longitude (°W Lon.)
September 23, 2005	2005 SEP 23 11:15	3	22.78	0.32	–	2.002	298.3
October 13, 2009	2009 OCT 13 23:26	4	11.83	0.55	190.5	2.198	148.5
December 09, 2009	2009 DEC 09 22:58	2	13.94	0.50	18.1	2.220	313.9
July 24, 2010	2010 JUL 24 22:15	2	12.90	4.66	282.1	2.475	312.7
March 20, 2011	2011 MAR 20 04:03	1	14.08	0.38	–	3.722	257.8

Table 3
Mapping details.

Date	Segment number	Relative time from start		Range		Ring inclination seen from S/C		Equatorial longitude scan spacing		Equatorial latitude beam footprint		S/C rotation axis (X/Y)	Orientation of 2nd to Saturn pole (N/S)
		Begin (h)	End (h)	Begin (R_S)	End (R_S)	Begin (°)	End (°)	Min (°)	Max (°)	Min (°)	Max (°)		
September 23, 2005	1	0	4.22	6.70	4.43	0.179	0.76	2.57	2.80	1.91	2.86	X	S
	2	4.97	12.55	2.69	2.45	−0.111	−0.278	1.50	2.32	0.86	1.16	X	S
	3	20.68	22.46	6.72	7.75	0.010	0.042	2.37	2.48	2.89	3.33	X	S
October 13, 2009	1	0	3.34	4.22	2.74	0.420	0.544	2.54	3.13	1.81	1.18	Y	S
	2	3.77	7.15	2.50	2.36	0.544	0.211	1.96	2.33	0.95	1.08	Y	S
	3	7.49	10.54	2.50	3.75	0.128	−0.224	2.44	3.12	1.08	1.61	Y	S
	4	10.96	11.83	4.04	4.41	−0.265	−0.310	2.96	3.12	1.74	1.90	Y	N
December 09, 2009	1	0	10.95	4.93	3.26	0.229	0.001	1.98	2.98	0.95	2.12	Y	S
	2	11.24	13.95	3.52	4.58	−0.051	−0.195	2.83	3.11	1.61	1.98	Y	N
July 24, 2010	1	0	11.29	2.79	4.60	2.788	−4.252	2.10	3.05	1.05	1.97	Y	S
	2	11.49	12.90	4.86	5.35	−4.128	−3.897	3.01	3.12	2.09	2.32	Y	N
March 20, 2011	1	0	14.08	5.64	5.12	0.049	0.261	2.66	2.93	1.60	2.41	Y	S

panel the mapping began at approximately 165° west longitude and proceeded westward. Each 1-s measurement is plotted as a single point.

Each scan crossed the limb onto cold sky (i.e., empty space with the approximately 2.7 K brightness temperature of the cosmic background), moving off the disk by a few beamwidths at each pole to enable the radiometric baseline determination described below. The net angular dimension of the pole-to-pole scan on the sky had to grow and shrink with time to follow Saturn's apparent diameter from the perspective of the spacecraft. In our operational sequence this dimension was readjusted only for a few scans at a time, leading to a sawtooth appearance in the off-disk data seen in later figures. The scanning was achieved using the spacecraft momentum wheels, accelerating and decelerating the spacecraft around one of its axes at the fastest possible rate (the respective spacecraft axes used for each observational segment are given in Table 3).

The 1-s integration time of the radiometer led to oversampling in latitude for all observations, but the limitations on spacecraft angular velocity using momentum wheels generally resulted in an undersampling in longitude. Fig. 2 illustrates this, showing the half-power beam footprints for two partial maps of Saturn that represent the highest (left) and lowest (right) spatial resolution achieved among all the observations. Both maps are from the September 2005 campaign (see Fig. 9). The brightness in latitude is actually oversampled – for clarity only every fourth footprint in latitude is shown here. The undersampling in longitude is real, however, and is unavoidable because of constraints on the spacecraft slew rate. The gap from 0° to 20° latitude in the scan at 298° is due to missing data and is filled in by interpolation in the image (this is the only such case for all the maps). Planetographic latitudes are used here and throughout except where explicitly noted. Table 3 illustrates that the variable geometrical aspects of the scanning conspired to give a fairly regular longitudinal spacing, in the approximate range 2–3° throughout. All of the mapping campaigns except that in 2011 were interrupted by the need to halt the scan to unwind the momentum wheels or, in the 2005 pass, to accommodate another observation as well. These pauses led to significant gaps in longitudinal coverage in all but the 2011 map.

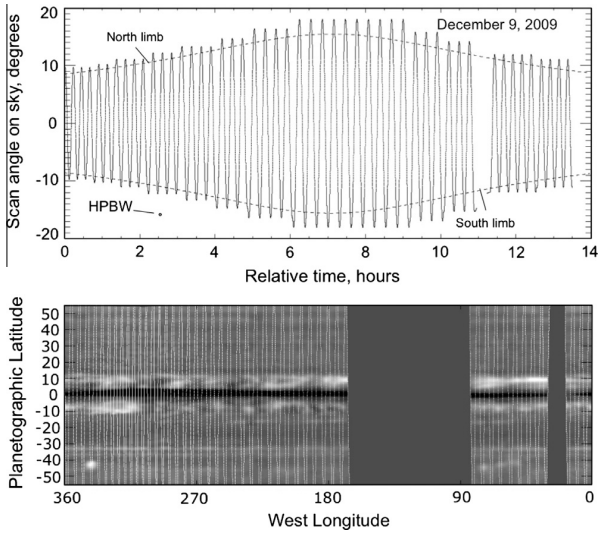

Fig. 1. Scan pattern of the radiometer for a mapping campaign in 2009, in inertial space and time (upper panel), and as tracks on the surface of Saturn (lower panel). The underlying map is derived from the data as described later in this paper. The 0.36° half-power beamwidth (HPBW) is shown in the upper panel for reference.

2.3. Calibration

The primary target for the RADAR instrument, including its radiometer, has been the surface of Saturn's moon Titan. The overall approach for radiometric observation and calibration used for Saturn in this paper was developed originally using Titan observations made through the period October 2004 to May 2007, as described by Janssen et al. (2009, henceforth referred to as J09). We have continued this effort through to the present, using a database on Titan that has now more than doubled. The approach is briefly summarized here. The radiometer provides an output signal (e.g., a voltage) that is proportional to the radiant power entering the radiometer within its 235 MHz bandpass (see Table 1). Both a cold and warm reference are required to determine a calibration factor that converts this output to radiance in appropriate units, which in the microwave region is brightness temperature in units of degrees Kelvin, or the temperature of a blackbody with equivalent radiance. This scale is effectively linear with radiant power since the microwave region is deep in the Rayleigh–Jeans regime of the Planck function, with differences that are negligible in the present study. Observation of cold sky (i.e., 2.7 K) provides the low-temperature reference, or baseline, while a source of known radiance is typically used to provide the high-temperature reference. The calibration factor, or gain, and the baseline both drift with time. For example, gain variations are caused by instrument thermal

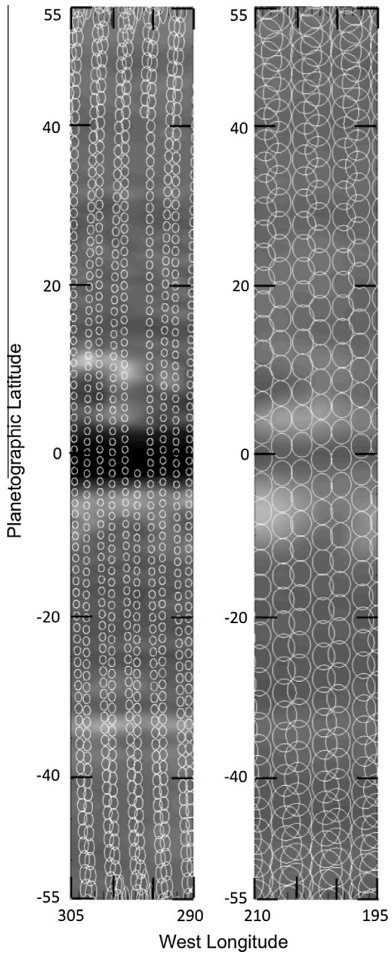

Fig. 2. Beam footprints on Saturn at two extremes of resolution. Shown are the half-power beam footprints on two partial maps of Saturn from September 2005.

variations resulting from instrument warm up after turn on as well as variations in the observing geometry and consequent solar illumination of the instrument during the course of the observations. Such variations also affect the baseline. Observations of cold sky obtained by moving off source from time to time enable the baseline drift to be tracked, while frequent views of our internal reference load allows relative gain variations to be tracked.

The absolute calibration, or the conversion of output voltage to radiometric brightness temperature in units of degrees Kelvin, must be independently obtained, and we used Titan for this purpose. During the period covered by J09, Titan was observed by the RADAR radiometer in 69 individual observing segments during 18 flybys of Titan by the Cassini spacecraft, at a variety of geometries and polarizations covering most of Titan, and at distances ranging from 1000 to 100,000 km. Global map mosaics of effective dielectric constant were determined from the measured thermal polarization. These enabled the construction of global maps of equivalent brightness temperature at normal incidence. We showed that the emissivity could be reliably predicted to better than 1% in special regions such as the dune fields and methane seas, which allowed us to make an absolute calibration of the brightness based on the measured physical temperature of the surface from the Huygens lander (93.7 K, Fulchignoni et al., 2005). In addition to the increased database of Titan observations, our physical reference temperature is now supplemented by extensive infrared surface temperature measurements by the Cassini Composite Infrared Spectrometer (CIRS, Jennings et al., 2009; Cottini et al., 2012), which we used to develop a seasonal surface temperature model for Titan's entire surface. This work will be reported in a future paper; however, we note here that the net calibration scale change from the J09 paper amounted to only about 0.5%.

Knowledge of the beam pattern is essential to construct absolute maps from the observations. The pattern of the circular central beam has been measured by scanning the Sun's emission to an accuracy of one part in 10^4 out to 2° from the boresight as described in J09. However, the sidelobes out to as far as 60° are responsible for a large additional signal, particularly at close range where the disk of Titan fills a significant fraction of the forward hemisphere; e.g., at close range the contribution of sidelobes outside 2° amount to nearly 30% of the main beam signal! These sidelobes were never measured in the ground calibrations and were unknown before the Titan observations; however, we solved for them as a byproduct of the mapping. Their knowledge allowed us to compute and remove this error signal for all Titan observations to within better than 1% of the main beam signal. Our solution was used for Saturn, which presents the same problem.

Finally, we consider that the gain of the radiometer may change in the long term over time, as for example might be expected due to aging of receiver components. Hence we included the determination of a slow linear drift of the gain in the Titan calibration over years. Although Titan was the reference used for this in the J09 calibration, we found that it was better determined from the present Saturn observations themselves. These considerations along with detailed error estimates are discussed following the presentation of the maps in the next section.

3. Mapping Saturn

3.1. Emission model

The results presented in this paper are given as maps of brightness temperature relative to brightness temperatures computed for an assumed model for Saturn's structure and ammonia distribution. The radiative transfer calculations used for this comparison rely on a computer program currently under development for the Juno Microwave Radiometer (MWR) experiment at Jupiter (Janssen et al., 2005, in preparation). This program, called the Juno Atmospheric Microwave Radiative Transfer (JAMRT) program, constructs model atmospheres and carries out radiative transfer calculations at microwave frequencies. This program was written specifically to support the Juno mission to Jupiter, but it is equally useful for the analysis of the Saturn observations reported here when the physical parameters and composition appropriate for Saturn are substituted for those of Jupiter.

The model atmosphere part of the JAMRT program builds deep convective models, including dry adiabatic lapse rates in the deep atmosphere and wet adiabatic lapse rates in the cloud forming regions. The release of heat in the ortho–para transition of H_2, assumed to be in equilibrium in all levels, is included. The gravitational potential is calculated using the equation for the potential function for a fluid having a uniform angular velocity (i.e., Lindal et al., 1985). We use the JPL NASA web site (ssd.jpl.nasa.gov/?gravity_fields_op) to obtain the gravity field data. The gravitational moments are referred to the distance 60,330 km. The radius of Saturn is taken to be 60,268 km. We use a rotation period of 10 h 32 m 35 s. The mass of Saturn in units of GM is taken to be 37,931,208 km^3/s^2. For the purposes of the radiative transfer calculations, we assume the atmosphere be stratified with the normal to the stratified layers following the normal to the equipotential surfaces of Saturn. The reference surface is located at the 1-bar

pressure level with a temperature that is selectable by the user. The full model atmosphere extends over the pressure range from 1000 bars to ~550 mb where the temperature is 110 K. Layer thicknesses are generally taken to be 100 m except in the vicinity of cloud layers, where we reduce the layer thickness to account for the transition that accompanies the formation of the clouds. The dry atmosphere components are H_2, He, CH_4, and the noble gas Argon. The condensable gases are H_2O, H_2S, PH_3 and NH_3. The condensates are H_2O ice, H_2O liquid, NH_3/H_2O solution, NH_4SH ice, and NH_3 ice. The program calculates the depletion of NH_3 both in the water cloud region, due to its absorption into water droplets, and in the ammonium hydrosulfide cloud region due to its interaction with H_2S to form NH_4SH. Vapor pressures and moist adiabats for these gases and condensates are given in Atreya (1986).

The brightness temperature of the atmosphere depends on the distribution of microwave absorbers with temperature. Central to the development of the JAMRT program was an effort, also funded by the Juno project, to better determine the microwave absorption coefficients of the constituents that contribute to Jupiter's thermal microwave emission. The potential absorbers include (1) the polarized gases NH_3, H_2O, PH_3, and H_2S, (2) pressure-induced absorption due to the non-polarized gases that constitute the bulk of the atmosphere, H_2, He, and CH_4, and (3) cloud particles. Gaseous ammonia, as the dominant source of microwave opacity in the gas giant planet atmospheres, has been given the most attention. Its absorption is due primarily to its very strong inversion band centered around 1.4-cm wavelength, and its absorption at longer wavelengths can be modeled as due to the pressure-broadened wings of the lines in this band along with some contribution from infrared rotational transitions. Its absorption coefficient has been measured in H_2–He mixtures over a pressure–temperature range consistent with the atmospheres of the gas giant planets, up to limiting values of 100 bars and 500 K respectively (Hanley et al., 2009; Deveraj, 2011). The data were fit with the help of a Ben-Reuven line-broadening model to produce an empirical expression for the NH_3 absorption coefficient that covers the 1.3–50-cm wavelength range of the Juno experiment. The uncertainty applicable to the 2.2-cm wavelength range for Saturn is estimated to be better than 10% (Hanley et al., 2009).

Our absorption model for PH_3 is based on pressure-broadened rotational transitions using a Van Vleck–Weisskopf lineshape, with absorption consistent with laboratory measurements (Hoffman et al., 2001; Mohammed, 2004). A similar calculation for H_2S is also consistent with laboratory measurements (DeBoer and Steffes, 1994). Although H_2O is a significant source of opacity in the deep atmosphere, it is largely absent from the region responsible for the 2.2-cm emission and of negligible importance here. Our model for H_2O absorption is from Karpowicz and Steffes (2011a, 2011b). Other polarized molecules (e.g., HCN, CN, and CO) are of much lower abundance and are not considered. Cloud NH_3 and NH_4SH ice particle absorption is estimated based on an assumed complex dielectric constant of $4.5 + 3.25 \times 10^{-6}\nu$ (GHz) for particle size $\ll$2.2 cm, a value based on data taken at 1 MHz on NH_3 ice by Lorenz (1998) and highly uncertain, while the absorption of H_2O/NH_3 mixtures in the water cloud region are based on laboratory measurements (Duong, 2011).

The JAMRT program has the capability to compute radiometric brightness temperatures for user-selectable absorber concentrations and cloud properties of condensable species, including their relative humidities in the cloud regions. Table 4 gives an estimate of Saturn's deep atmosphere composition based on values derived from Atreya (2010). Fig. 3 shows the absorption with pressure of the leading absorbers in the atmosphere computed for an atmosphere with this composition, assuming that all condensable species form fully saturated clouds (i.e., 100% relative humidity) with no precipitation. Gaseous ammonia is seen to be by far the dominant absorber in the atmosphere, particularly in the region responsible for the 2.2-cm emission. Phosphine is the next most important absorber above the water cloud region, although with a contribution three or four orders of magnitude less than that of NH_3 in the effective region of emission. H_2S absorption is yet smaller, besides which it effectively disappears in the region where the 2.2-cm emission originates as it combines with NH_3. We note that although H_2S contributes negligibly to the absorption directly, its deep abundance can have a significant impact on the 2.2-cm brightness through this depletion of upper-level ammonia. Other polarized molecules (e.g., HCN, CN, and CO) are of much lower abundance and are not considered. The sum of collision-induced absorption due to H_2, He, and CH_4 collisions is shown (Orton et al., 2007; Birnbaum et al., 1996; Borysow and Frommhold, 1986) and seen to be negligible at our wavelength. The contributions from NH_3 and NH_4SH ice particle shown in the figure are reasonable but rough estimates, but are highly conservative because of the assumption that no precipitation occurs. We consider their possible contributions to be negligible.

The JAMRT program has much flexibility (see L13 for a more general application). In this paper, we take as our standard only the very simple case illustrated in Fig. 4, which assumes the model atmosphere described above with the composition given in Table 4, moist adiabatic temperature lapse rates and full saturation for cloud regions, and a temperature of 134.8 K at the 1-bar pressure level based on the Voyager measurement by Lindal et al. (1985). We use this case as a reference model with which to compare our brightness measurements. Fig. 4 depicts the atmosphere's

Table 4
Composition of the Saturn reference model atmosphere (based on Atreya (2010)).

Constituent	Solar abundance (mixing ratio relative to H_2)	Enrichment of the Saturn atmosphere relative to solar
He	0.195	0.6955
CH_4	5.5×10^{-4}	9.4
H_2O	1.026×10^{-3}	3.0
NH_3	1.352×10^{-4}	3.0
H_2S	3.10×10^{-5}	5.0
Ar	7.24×10^{-6}	1.0
PH_3	5.14×10^{-7}	7.5

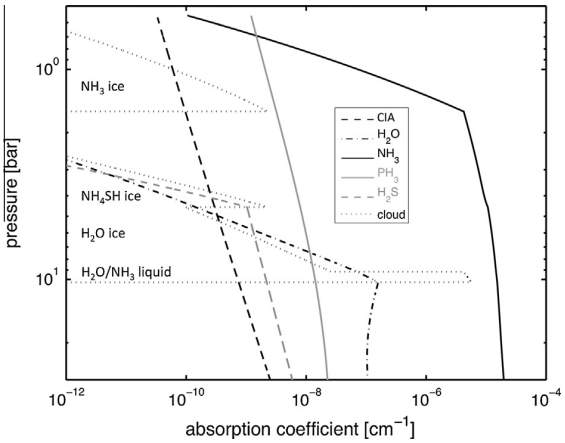

Fig. 3. Microwave absorption profiles at 2-cm wavelength for possible absorbing constituents through the NH_3 cloud region. The atmospheric composition is that of our reference model as given in Table 4. The dotted lines indicate conservative estimates for various particulate absorbers as indicated, while the other lines represent individual gases identified in the legend. The curve labeled CIA includes the sum of H_2–H_2, H_2–He, and H_2–CH_4 collision-induced absorption.

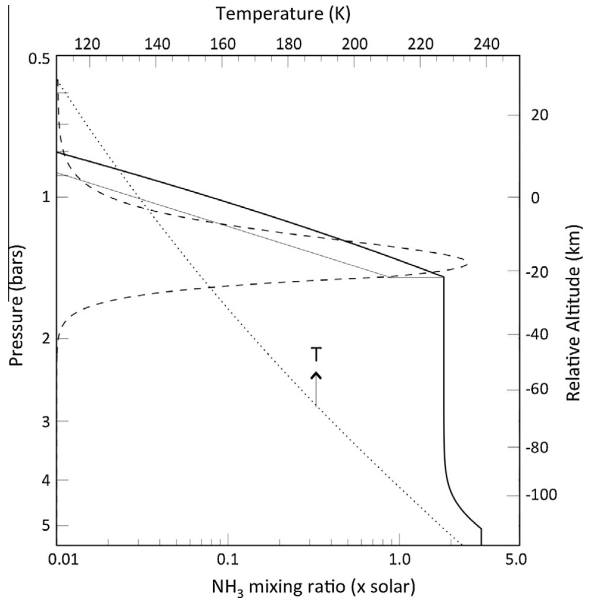

Fig. 4. Atmospheric model used to compute reference brightness temperatures. The temperature (dotted line) and NH_3 mixing ratio in units of solar abundance (thick solid line) are shown as a function of pressure and altitude in the vicinity of the ammonia cloud region in the atmosphere. The reference model assumes 100% relative humidity for ammonia above its saturation level, while the light solid line shows a case for 50% relative humidity. The decrease in NH_3 mixing ratio above the 5-bar level is due to reaction with H_2S to form NH_4SH ice. The dashed line shows the 2.2-cm wavelength weighting function in arbitrary linear units at normal incidence for the reference model.

pressure–temperature relationship along with the ammonia distribution and the corresponding weighting function at 2.2 cm. Note that the ammonia mixing ratio is not constant beneath its nominal saturation level – this is because it is assumed to interact with subcloud H_2S to form ammonium hydrosulfide, which reduces the NH_3 mixing ratio until all of the sulfur is depleted (the loss of NH_3 into water cloud drops is small relative to this). For example, the microwave spectrum has been interpreted to show such a subcloud depletion (Briggs and Sackett, 1989; Grossman, 1990; de Pater et al., 2001). The ammonia concentration above the saturation level is assumed to follow the Clausius–Clapeyron equation, equivalent to the assumption that the cloud region relative humidity is everywhere 100%.

All results in the following are presented as residuals after the subtraction of the reference model brightness values from the measured values, where we take into account both emission angle and latitude dependence in the model for each measurement point. Unless supersaturation is allowed, any plausible redistribution of ammonia in this model for a given deep abundance can only reduce the amount of vapor in the emission region, which lowers the weighting function and results in a higher brightness temperature because of the atmospheric temperature lapse rate. Hence the brightness temperature residuals are expected to all be positive. Since the 2-cm weighting function lies almost entirely within the saturation region in the reference model, the computed brightness temperatures are only weakly dependent on the deep abundance of ammonia. Further, the brightness temperature is insensitive to physical temperature variations in the cloud region. If the specific humidity were held constant, then the brightness temperature would indeed vary directly with the kinetic temperature; however, at constant relative humidity as assumed in the model, the weighting function follows the ammonia as the temperature of the cloud-region atmosphere is varied and tends to stay constant in relation to temperature. There is a small effect, about 1 K of brightness temperature change for a 5 K shift in the adiabat, caused by the corresponding pressure shift with temperature and the effect of this on the absorption model. In view of these considerations we conclude that the radiometric brightness at 2.2 cm depends to first order only on the ammonia distribution, and in particular only on the cloud-level humidity for small departures from the reference model. However, when the cloud-level ammonia becomes highly depleted, the weighting function descends into the subcloud region and the interpretation becomes more complicated. This condition occurs in several important regions in the present maps, and L13 presents a more complete discussion of the implications that the 2.2-cm data hold for the ammonia subcloud distribution in such a case.

3.2. Generating maps

The time-ordered scan data consist of a stream of relative values for the antenna temperatures on the sky and the reference load obtained each second. Maps were produced from these data in a series of steps, which we outline here and illustrate below. To begin, we note that we use the same convention as described in J09 for defining the power collected by the antenna, the "antenna temperature", and the source brightness, or "brightness temperature". In usual practice the antenna temperature, or radiant power collected by the antenna, is the brightness temperature integrated over the whole sky as weighted by a normalized antenna gain pattern; e.g., the antenna temperature of a blackbody distribution over the whole sphere would be the blackbody brightness temperature (cf. Janssen, 1993). In principle the brightness temperature distribution may be determined from measured antenna temperatures by inverting this relationship, subject to a loss of spatial resolution at scales smaller than the main antenna beam. However, we assume here an antenna temperature calibration scale that is normalized over only the measured antenna pattern inside a cutoff angle of 2° where the pattern is well known (see Section 2.2 of J09), with a gain calibration factor applied to the raw radiometer signal as appropriately determined for this convention. It remains then to determine and subtract the sidelobe contributions, after which the correctly scaled brightness distribution is obtained with knowledge of this truncated main beam pattern (henceforth called the TMB). This approach is convenient for the case where the absolute calibration of measurements over an extended source is based on source "ground truth", as was the case for Titan, since residual errors in the knowledge of both the near and far beam pattern are canceled out to first order. For example, the net results were shown in J09 to be insensitive to the exact choice of cutoff angle.

The gain calibration determined for Titan was first directly applied to the raw data on Saturn to convert them to the Kelvin scale without concern for baseline variations, using the above convention for beam normalization. At the same time, the beam pattern was convolved with the brightness temperature distribution of our reference model for the observing geometry of each measurement point to produce a set of model antenna temperatures. As with Titan, the beam pattern convolution was performed separately for the TMB and the far sidelobe pattern (FSL in the following). This convolution took into account the modeled emission-angle variation of the brightness across Saturn and assumed a value of 2.7 K for points off the disk. The model included a simple description of the ring blockage for the FSL convolution, but not for the TMB convolution for reasons discussed later. The cold sky baseline was determined from the excursions off the disk at the end of every scan, using the sum of the TMB and FSL convolutions to correct the baseline for all sidelobe contributions to the off-disk measurements. Specifically, each off-disk excursion was used to estimate a baseline correction to the calibrated data set applicable

for that time, and the offset for all data points was then determined by linear interpolation with time between adjacent baseline estimates. Subtraction of the FSL convolution from all the data then removes this contribution as if it were an error signal, while application of the baseline correction adjusts the data to an absolute scale consistent with our normalization. Subtraction of the TMB convolution over the reference model from this calibrated and baseline-adjusted data set then produces a set of time-ordered residual antenna temperatures, which we interpret as residual brightness temperatures of Saturn relative to the model corrected for both near and far sidelobes. These were then interpolated onto a regular grid in cylindrical coordinates to produce maps. The remainder of this paper deals only with such maps of brightness temperature residuals.

We use the December 2009 mapping campaign as an example to illustrate the steps leading to a set of time-ordered residual brightness temperatures as well as an initial map based on them prior to the removal of remaining systematic errors. The four panels of Fig. 5 show the steps taken to obtain the calibrated and baseline-adjusted antenna temperatures from this campaign. Each 1-s measurement is plotted as a single point in all panels. Top to bottom, the panels show respectively: (a) the time-ordered data on a scale that is calibrated for brightness temperature but uncorrected for a variable offset due to far sidelobe contributions and baseline drift; (b) the individual convolutions over the reference model for Saturn's brightness distribution by the truncated main beam and complementary far sidelobe pattern, labeled TMB and FSL respectively in the right-hand portion of this panel; (c) the zero offset correction for the time-ordered calibrated data derived using the modeled off-disk antenna temperatures and far sidelobe corrections shown in (b); and (d) the final calibrated and baseline-adjusted antenna temperatures obtained by subtracting the zero offset and the far sidelobe contribution from the calibrated data set in (a). The right-hand section of each panel shows a subset of the data on an expanded time scale centered near the center of the pass.

Systematic features seen in these plots are artifacts due to the scan pattern and model assumptions. The ragged signal shown at the base of the measured antenna temperatures in panel (a) is due to the presence of contributions from both near and far sidelobes when the beam axis moves off the disk, with the sawtooth appearance of the minima reflecting the periodic adjustments made in the scan to follow the limb. Panel (b) shows that this pattern is predicted by the modeling. This panel shows two overlying plots representing the separate convolutions of the model by the TMB and FSL patterns. The signal from the latter is observed as the set of points in the middle of the plot smoothly ranging from about 5 K to nearly 25 K. These are largest when the beam approaches the center of the disk, and remain relatively large (7–10 K) even when the beam goes off the disk. The TMB values go to zero when the beam axis moves more than 2° off the disk as seen near the center of the scan, leaving the observed sawtooth pattern where it does not. The baseline in the final adjusted and calibrated data set in panel (d) is seen to correspond to the 2.7 K sky background brightness, while examination of the right-hand plot shows that the scatter of points below this baseline are due to the transition of the beam across the disk edge where the measured signal is sensitive to small pointing errors.

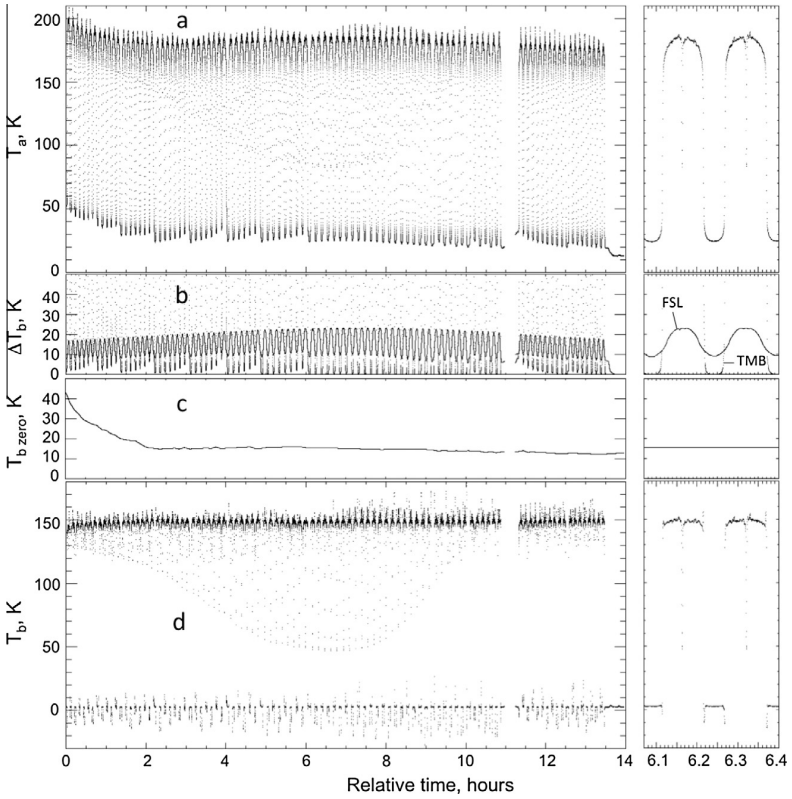

Fig. 5. Initial steps in the calibration process are illustrated for the December 2009 map. Each 1-s measurement from this observing campaign is plotted as a single point in all panels. Top to bottom, the panels show respectively: (a) the time-ordered data with an initial scale calibration but without a baseline correction; (b) model convolutions over the reference model to obtain estimates of the sidelobe contributions; (c) a derived zero offset correction; and (d) the final calibrated and baseline-adjusted antenna temperatures. The right-hand section of each panel shows a subset of the data on an expanded time scale centered near the center of the pass.

The brightness residuals were then used to generate the global cylindrical map shown in Fig. 6. This map was made using the idl TRIANGULATE procedure and TRIGRID function to interpolate the irregularly-spaced time-ordered measurements onto a regular grid with 0.5° spacing, using idl's CONTOUR plotting routine to produce the map. The gray scale was chosen to show the unmeasured portion of the plot as a dark gray corresponding to a residual of 0 K, i.e., as the brightness of the reference model, compared to which the maps points are expected to show a lighter shade. The black region along the equator is due to blockage by the rings, which are mostly optically thick and of much lower brightness than the disk. This and all following maps were cut off beyond an emission angle of 70°, where small errors in pointing begin to dominate the brightness uncertainty.

This map demonstrates the ability of the radiometer to distinguish among small features with brightness variations approaching the 0.1 K white-noise level of the measurements, a capability also demonstrated in the Titan observations. Nevertheless the map contains artifacts with greater brightness variations on large spatial scales that need to be accounted for. The most obvious occurs at the start of the scan at approximately 165° west longitude, where the first 30° or so of the map westward from this appears significantly cooler than the remainder of the map. This is an artifact seen only in the December 2009 map. In all other observations we used a warm-up period of 3 h prior to operations to allow the radiometer to thermally stabilize; however, in this case we were prevented from doing this by a power conflict with a previous (non-RADAR) observation. We elected to start our mapping immediately at RADAR turn-on knowing that our calibration algorithm was not valid for the resulting thermal transient. We in fact see about a 3 K brightness temperature drift in the map, a warm-up effect also apparent in the baseline drift seen in panel (c) of Fig. 5. Another apparent artifact is a striping with longitude, a smaller systematic effect that we ascribe to the incomplete removal of sidelobe signal in the establishment of the baseline.

An artifact not immediately apparent but also important to consider is a low-spatial-frequency brightness error caused by range-related errors in removing the far sidelobe contribution. The solution for the Titan mapping was less dependent on the removal of this error signal because of the way the map mosaic was constructed. The Titan mapping used low-resolution observations made at long range, with small and ultimately accountable far sidelobe contributions, to provide the absolute map level, while observations at closer range were used to provide the higher spatial resolution components. At the same time the far sidelobe contributions were determined from the range-dependent offsets obtained in reconciling near and far-range measurements of the same regions on Titan. The sidelobe pattern was retrieved as part of this reconciliation, for example. This was simplified by assuming it to depend only on polar angle, i.e., to be uniform in azimuth. This process essentially filtered out residual errors associated with the large sidelobe contributions from the close-range measurements, and so was adequate for Titan. This solution left the possibility of residual low-spatial-frequency errors for the Saturn mapping, however, and are estimated based on the J09 analysis to be present at around the 1% level.

We searched for such residual sidelobe contamination in the maps, anticipating that they would appear as systematic errors that depend on spacecraft range and orientation. We took advantage of regions of latitude in both hemispheres in which there is little or no longitudinal structure; in particular, we considered the bands from about 15° to 55° latitude in the north, and −15° to 32° latitude in the south, where no longitudinal structure was discernable in any of the maps except for the northern storm in the 2011 map and the ring blockage in the 2010 map. Excluding the latter, we expected the average brightness across these latitudes to be approximately the same for each scan. Fig. 7 shows the weighted average of these "quiescent" bands in both hemispheres plotted for each scan as a function of elapsed time, with the mean for all scans subtracted to give a zero mean offset. The features in these plots can be associated with the three main sources of error we expect to see. First, the general trend among the plots follows the shape of the respective range curves, which are also plotted and shown as solid lines. This trend indicates an uncorrected sidelobe contribution that varies by as much as 1 K with range, consistent with the ∼1% sidelobe error residual anticipated. Secondly, gain drifts are present, most notably the ∼2% drift seen at the start of the December 2009 mapping campaign. Another possible gain variation is apparent in the third segment of the September 2005 campaign, which is offset by about 1% relative to the average over the same range in the first segment. Thirdly, the remaining scatter may be explained by errors in the baseline correction, caused by a combination of short-term gain drifts and residual errors in the offset modeling. The latter explanation is consistent with the correlation between the patterns in these and the TMB modeling of the off-limb scans in panel (b) of Fig. 5; e.g., compare the upward drift seen in Fig. 7 for the December 2009 plot from about 11 to 12 h to the minima at the same times in the TMB values in panel (b) of Fig. 5.

We also used the quiescent band mean brightness for each map to examine the long-term dependence on gain (or Saturn's mean brightness) with time. The original Titan calibration used a series of measurements of Titan's unresolved disk brightness temperature made from long range to search for gain calibration drift in the measurements (J09). This was reexamined with distant Titan observations obtained through 2012, finding a downward gain drift of 0.2% per year, but barely statistically significant. This rate was incorporated into the present Saturn calibration. Fig. 8 shows the dependence with time on the quiescent band mean brightnesses obtained using this gain drift rate. If correct, this would indicate a steady brightness temperature decrease of Saturn in these quiescent bands, which we consider unlikely. Rather, we take the drift

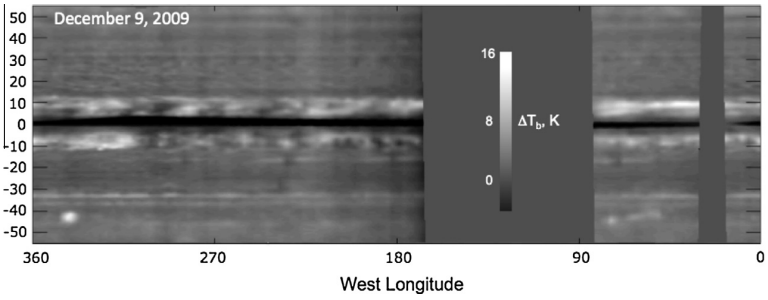

Fig. 6. Global map of brightness temperature residuals from December 2009, before further adjustment to remove artifacts.

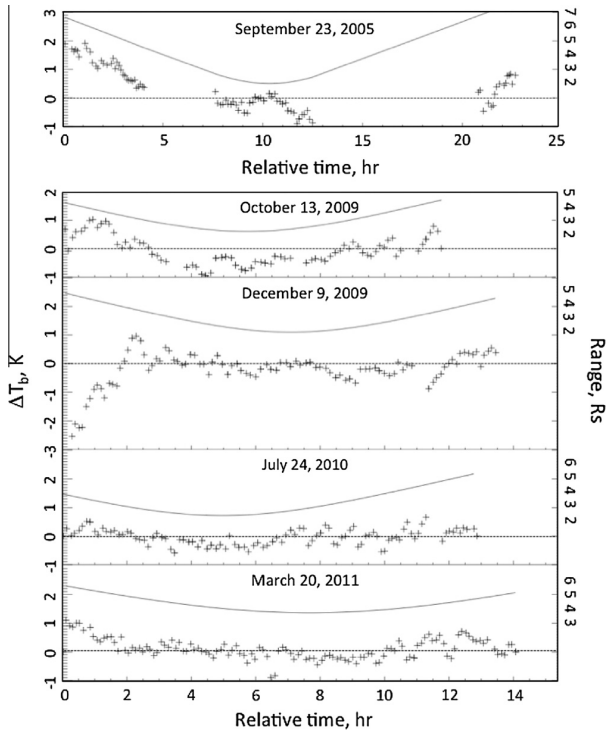

Fig. 7. Mean values by scan of "quiescent" latitudinal bands in northern and southern hemispheres, plotted by elapsed time and compared with range for each map. Each point (+) shows the mean brightness temperatures of each individual scan in these bands, plotted relative to the overall mean, with values given on the left-hand scale. The solid curves show range in units of Saturn radii as given on the right-hand scale.

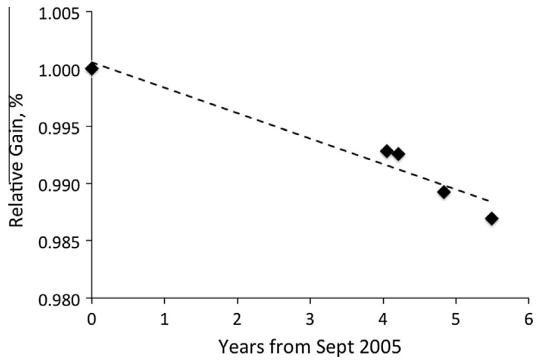

Fig. 8. Values of global mean quiescent band brightness temperatures as described in the text for each calibrated Saturn map relative to that for September 2005. The dashed line is a linear fit that we take to indicate a radiometer gain drift with time.

apparent in Fig. 8 to indicate a net radiometer gain decrease of about 0.4% per year. This is larger than that obtained from the current distant Titan observations, but it is within its error margin and has better precision. We then used this revised rate to adjust each of the maps relative to the epoch valid for the transfer of the Titan absolute calibration from J09.

3.3. The maps

After correcting the data for gain drift, the final residual maps were produced by subtracting the quiescent-band averages of Fig. 7 from each scan in the time-ordered data, using the interpolation described for Fig. 6 to produce the final gridded cylindrical maps shown in Fig. 9. Table 3 supplements these maps by providing details of the map characteristics, which vary with latitude and longitude because of the changing geometry. These maps then represent our best estimates of Saturn's brightness distribution at the times of observation.

We have searched for other sources of error in the mapping but have found nothing of such significance as to warrant further analysis. In principle the steps leading to these maps could be iterated, using the map from one iteration to generate the residuals of the next, continuing until the solution converged on the best estimate of Saturn's brightness temperature distribution consistent with the measurements. However, we find that the solution converges sufficiently well in a second iteration that used Saturn's mean brightness instead of the reference model to recompute and remove the FSL contribution, with remaining uncertainties such as those due to ring blockage limiting the usefulness of further iterations. Fig. 10 shows the brightness temperature distribution with latitude for a single scan across the rings where they were the most open in the July 2010 mapping campaign. The behavior of this blockage with ring inclination could be modeled from the present data and likely contains information about the scattering properties of the rings; however, this is not easily accomplished, and the gain to understanding Saturn's atmosphere was deemed to be small and beyond our scope. In particular, we neglect the contribution from the inner sidelobes of the main beam, which affect the brightness measured within a few beamwidths of the edge of the ring blockage. In the far sidelobe convolution the details of the ring brightness distribution are not important; however, their integrated effect needs to be considered, particularly for the July 2010 map. As an approximation we assumed, for all maps, a constant brightness of 40 K for all inclinations in the region of geometrical blockage. This simple model is sufficient for our purposes; for example, a 10 K error in this value would primarily affect the July 2010 modeling, where it is estimated to lead to an error less than 0.5 K. This being the worst case, we ignore this source of error overall.

The far sidelobe solution for Titan assumed the pattern to be independent of azimuth angle. A possible north–south asymmetry in the far sidelobes could have an impact on the determination of asymmetries between Saturn's northern and southern hemispheres. The scanning used in the three mapping campaigns in 2009 and 2010 inverted the spacecraft rotation axis with respect to Saturn's poles in the final observational segment of each map (see Table 3), however, and this allows us to test for such an artifact. In Fig. 11 we compare the latitudinal dependencies before and after the spacecraft inversion by individually averaging the longitudinal brightness at each latitude. An asymmetry in the pattern would appear in the difference of these averages. We see no sign of such an asymmetry in the figure within the variability caused by real longitudinal brightness structure, which is less than 1 K outside the active latitudes and regions of ring blockage. A systematic polar angle error in this pattern is not detected by this approach, however, and remains possible in the range-dependent signal seen in Fig. 7. We anticipate that an uncompensated systematic error as large as 1 K that is symmetric around the equator could be present based on studies described in J09.

The absolute calibration for Titan was determined to be about 1% in J09. This result is confirmed and improved by current work in progress, although here we claim only the calibration accuracy described in detail by J09. The transfer of this calibration to Saturn involves additional uncertainties that follow from the steps described above. A range-dependent effect on the order of 1% was anticipated in the Titan calibration process, and is apparent in

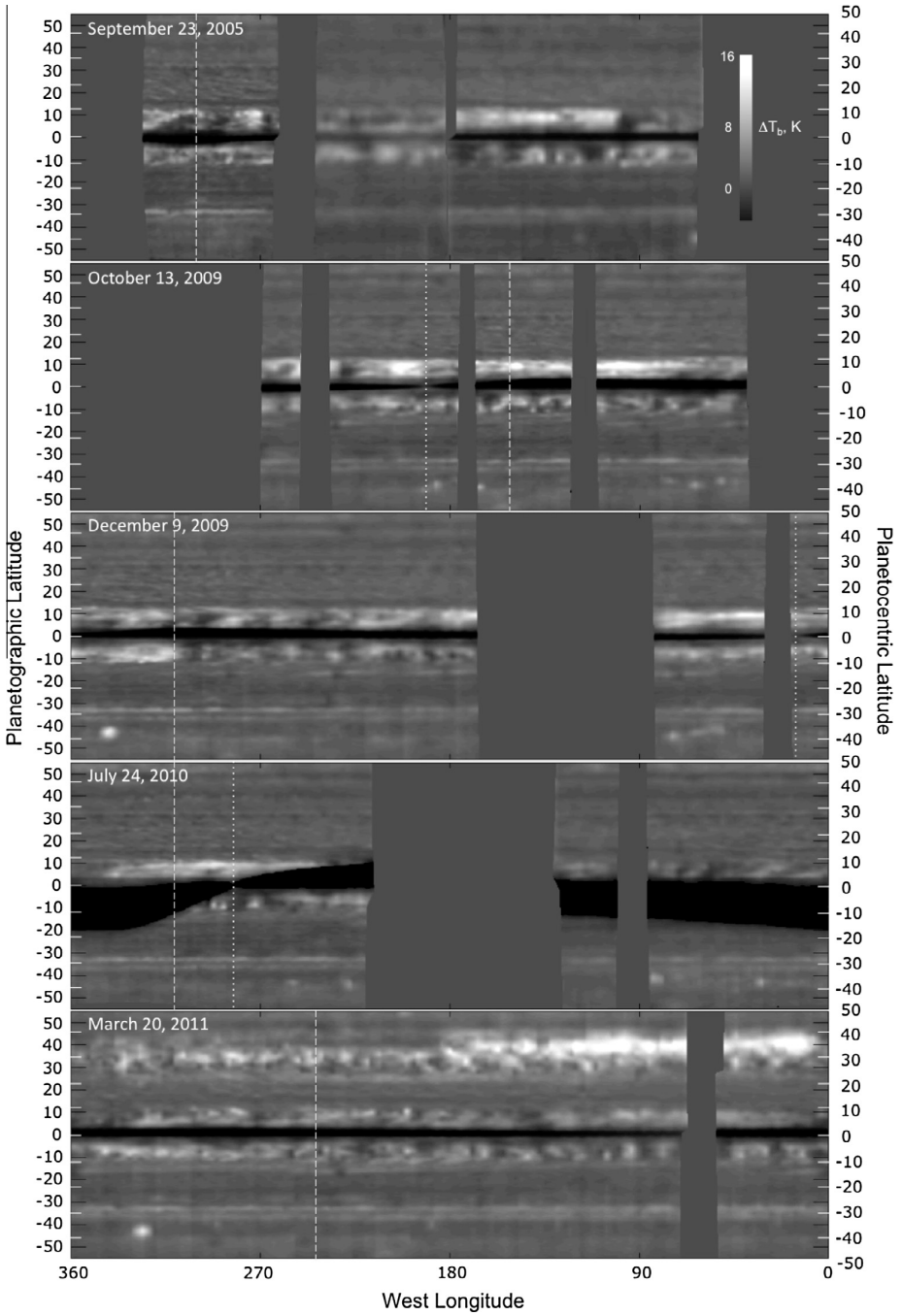

Fig. 9. Final cylindrical maps of Saturn from the five observation campaigns. The absolutely calibrated maps are shown in the five panels as residuals from a model that assumes ammonia to be fully saturated in the cloud-forming region. The dashed and dotted lines indicate periapsis and ring plane crossings, respectively (there were no observations made exactly at ring plane crossing for the 2005 and 2011 maps). Planetographic latitudes are indicated by black ticks on the vertical scales, planetocentric by white. The unobserved portions of the maps are shaded to the equivalent brightness for the fully saturated model, so that, except for the ring blockage around the equator, the maps indicate that the ammonia cloud region is everywhere unsaturated. Orbital characteristics and mapping details are given in Tables 2 and 3, and uncertainties and caveats concerning the maps are given in the text.

Fig. 7 with a value ranging over about ±0.5%. Errors in the removal of gain as well as sidelobe signal variations using the quiescent-band averages will lead to errors as well, which we judge to be relatively small by examining the time dependence of these averages in Fig. 8. Conservatively, we expect an absolute uncertainty better than 2%, or a brightness temperature uncertainty less than 3 K. Large-scale systematic errors are smaller, perhaps as much as 1 K from equator to pole as discussed above, and <1 K elsewhere Small-scale errors are consistent with the white noise of the individual measurements, ~0.1 K.

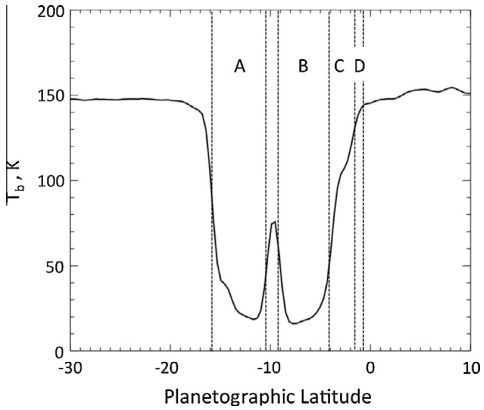

Fig. 10. Brightness distribution through the region of ring blockage. The calibrated brightness temperature is shown for one scan in latitude around the time of peak ring inclination with respect to the spacecraft in the July 2010 mapping campaign. The boundaries between the rings are indicated. The Cassini Division is clearly seen.

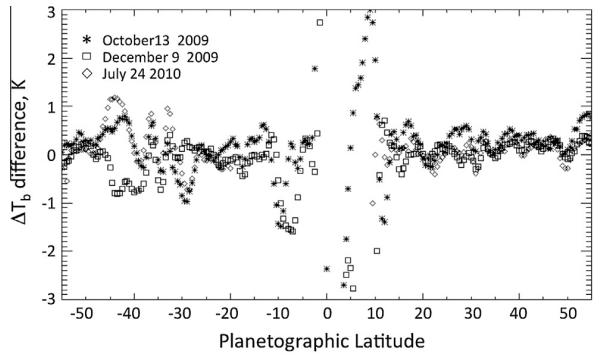

Fig. 11. Differenced longitudinal averages of the latitudinal brightness distribution for the three maps in which the spacecraft *Y*-axis was inverted partway through the observation. The longitudinal brightness at each 0.5° in latitude was averaged separately for the two orientations and subtracted to search for an asymmetry in the N–S sidelobe pattern. None is apparent.

4. Discussion

The maps in Fig. 9 reveal features either never before seen or known features viewed from a perspective never before available. The region of the atmosphere responsible for the microwave brightness variations, ~0.5–2 bars, has been extensively observed with high-resolution instruments at infrared wavelengths. Nevertheless, the unique value of observations at 2.2-cm wavelength is the simple origin of the observed structure – it is just ammonia vapor and variations in its distribution. Low residual brightnesses indicate the presence of gas phase ammonia in the cloud region at concentrations approaching but not exceeding its saturation level, whereas higher brightnesses indicate depletion relative to this. The variability of the brightness distribution across Saturn suggests the existence of circulations that cause the depletion or enhancement of the ammonia by means of gas flow into and out of the ammonia condensation region, while the morphologies of these variations give clues as to the nature of the dynamical forcing causing these flows. Obvious features include the bright bands that are symmetric about the equator from approximately 3° to 10° latitude north and south respectively, where regions of high brightness alternate with low brightness regions resulting in longitudinal variability not seen at higher latitudes until the great northern storm in the 2011 map. The regions of high brightness in these bands are "dry" in the sense of low ammonia abundance, and therefore resemble the dry sub-tropics of Earth. They are perhaps indicative of the convective organization of planetary waves similar to related pervasive features within the Earth's tropics and the 11–13 wavenumber plumes and 5-μm hot spots on Jupiter (Allison, 1990; Arregi et al., 2006).

In between these bands, at the equator, is a central band of relative calm with the lowest brightness seen on Saturn. The low brightness seen here indicates ammonia concentration to be near saturation, consistent with the greatly enhanced NH_3 abundances found by VIMS in this region (Fletcher et al., 2011). Although difficult to discern because of the ring blockage, this band is apparent at or near the ring crossings, most notably in the central segment of the 2005 map. Although at relatively low resolution, the ring inclination in this segment is near 0.01° as seen from the spacecraft, with the blockage causing less than a 1 K influence on the brightness. L13 presents a more thorough examination of the ring blockage, using a ring model to retrieve the equatorial brightnesses at the ring plane crossings for all maps to confirm the presence generally of near-saturated ammonia in the equatorial belt.

Relatively strong narrow bands with less longitudinal structure are seen in the south at −33° and −37° latitude. The northern latitudes show milder banding (until the eruption of the great northern storm) with little similarity to the southern hemisphere. A major feature seen in the southern hemisphere is a series of large circular bright features between −42° and −47° latitude. These are apparently related to lightning storms observed at optical and infrared wavelengths (Porco et al., 2005). They appear just south of the westward jet at −41° (−35° planetocentric) latitude (Sanchez-Lavega et al., 2000). Their development and life cycle is uncertain and likely complex. In methane band images they first appear as high, thick clouds with irregular, convective morphology. Baines et al. (2009) see spectroscopically-identifiable ammonia clouds first appearing in association with lightning, followed by the emergence of dark clouds that are optically-thick at 5 μm with a spectrum consistent with dark carbon soot. Meanwhile, Dyudina et al. (2007) report their emergence after a few days as circular spots with only a thin haze over a cloud-free deep atmosphere (see her Figs. 3 and 4). At the stage we see them (possibly later in their development) they have become relatively extensive areas that are depleted in ammonia, likely well below the ammonia condensation level (see L13).

The great northern storm appearing in the 2011 map is depicted again in Fig. 12 with a shading stretch that better shows its structure, along with the beam footprints to illustrate the spatial resolution in this image. Overall, this is a brighter and more widespread feature than seen elsewhere in any of the maps. There are a few regions elsewhere that show peak residuals as high as seen throughout the storm, but these are localized (e.g., occasional spots in the equatorial storm bands) and likely represent extremes for a relatively weaker class of feature. The 2011 image of the great northern storm indicates the depletion of ammonia on much larger scales than seen in the other maps. Implications of this for atmospheric processes at work are discussed further in L13.

Fig. 13 shows the latitudinal structure and its variability with time for all maps. Each point represents the unweighted average of the brightness residuals in each map at 0.5° increments of latitude. With the exception of unobserved regions, all values are included irrespective of ring blockage, etc. The overall latitudinal structure in this representation shows a remarkable degree of repeatability, apart from the readily apparent ring blockage in the equatorial region and the singular effect of the 2011 storm. A north–south asymmetry is evident in both brightness and structure. The narrow bright bands and circular bright features dominate the southern structure, while the northern midlatitudes

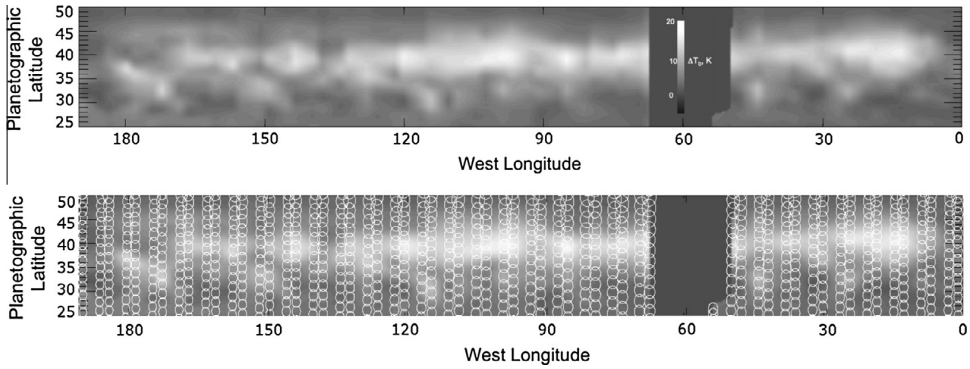

Fig. 12. The great northern storm of 2010. The section of the March 2011 map containing the storm is shown in the upper panel with a stretch that enhances the high brightness regions. The lower panel gives the half-power footprints (showing only every fourth footprint in latitude).

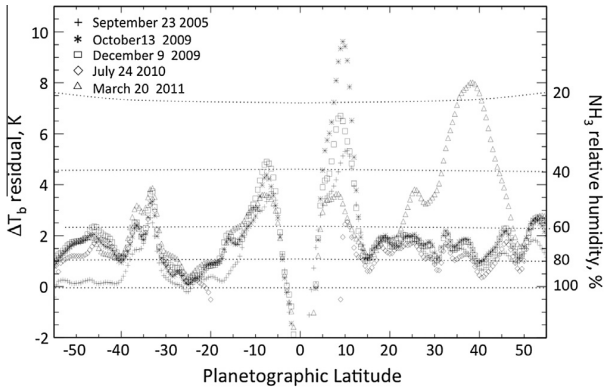

Fig. 13. Longitudinal averages of the latitudinal brightness distribution for all maps. The equatorial region within 5° is generally dominated by ring blockage, as is the region from −20° to 0° for the July 2010 map – the plunge to negative residuals in these regions is an artifact of this. The dotted lines indicate model brightness residuals that would be observed if cloud relative humidity were allowed to vary relative to the fully saturated model.

show repetitive banding at approximately 10° spacing. Residual brightness temperatures in the region from about −15° to −30° are almost as low as those in the central equatorial band inside 3°. Finally, the north equatorial band from 3° to 10° shows significant variability, while its southern counterpart appears relatively constant. We have no simple explanation for the asymmetries we see. These may have to do with seasonal variations, or may reflect some degree of chaos in Saturn's large-scale circulations. For example, Jupiter has a small obliquity compared to Saturn, but has demonstrated considerable and apparently chaotic variability in belt-zone structure over the decades. Seasonal shadowing by Saturn's rings resulting from its large obliquity could lead to seasonal variations between hemispheres if solar forcing were significant in driving circulations. We call attention to the structural asymmetry in the banding apparent in the maps of Fig. 9 from approximately 10° to 30° latitude, best seen in the high-resolution segment of the 2005 map. The southern hemisphere in this region shows faint but discernably regular banding, while the northern counterpart appears mottled. The latter was in the ring shadow in 2005 and the irregular appearance may reflect a lack of solar forcing.

We use a simple variation on our reference model to illustrate the dependence of the brightness residuals on ammonia distribution in this figure. As in the reference model we assume a constant deep ammonia mixing ratio of 3 × solar, however, above its condensation level we assume a constant relative humidity, the value of which we allow to vary (this is equivalent to the parameter DF_{cb} in L13). For example, the light solid line in Fig. 4 shows such a case for a cloud relative humidity of 50%. The dotted lines in Fig. 13 show the brightness then expected for a given cloud relative humidity, which varies weakly as a function of the viewing geometry and is aliased closely with latitude. Our immediate interpretation is that most of the brightness structure seen throughout the maps can be explained by varying ammonia concentrations in the cloud region alone. The exceptions are the equatorial bright bands bracketing the equator, the circular bright features seen between −42° and −47° latitude, and the northern storm in the 2011 map, all of which have regions that cannot be explained unless subcloud ammonia is depleted as well. The companion paper L13 considers the effect of subcloud mixing ratios using a more realistic model involving both cloud-level and subcloud variations in ammonia concentration.

5. Conclusions

The advantage of proximity gained from a spacecraft platform has enabled a significant advance to be made in observing Saturn in the microwave region. Earth-based platforms such as the VLA and more recent millimeter and submillimeter arrays have provided the best imaging results on Saturn prior to this work, but their capabilities are limited by the aperture synthesis approach they require. Although theoretically capable of higher spatial resolution and sensitivity, reported VLA images of Saturn in the centimeter-wavelength region show 0.9 arcsec resolution at best, equivalent to ∼6° latitude at the equator, with brightness temperature sensitivity >1 K. Broad latitudinal banding has been observed under these conditions, and the use of multiple frequencies has enabled useful interpretations of the distribution of absorbers (Grossman et al., 1989; Grossman, 1990; van der Tak et al., 1999). However, longitudinal structure on rotating planets is difficult to obtain by aperture synthesis, and has never been attempted for Saturn. The present maps resolve latitudinal structure as small as 1° and longitudinal structure to 2°, a significant improvement. Our absolute calibration of 2% represents an improvement by at least a factor of two as well. The sensitivity for features on small scales, as good as 0.1%, appears to be over an order of magnitude better, while the largest remaining source of error is the possibility of a systematic error of ∼1 K that is symmetric about the equator.

As a result we see structure at resolutions approaching those achieved by ground-based optical and infrared telescopes, and begin to identify features that appear related to those seen both from ground and space at these shorter wavelengths. Our 6-year baseline and excellent stability allows us to contribute to the

question of Saturn's long-term stability. We find that Saturn's brightness has been remarkably stable over this period at most latitudes, with variations much less than 1%. Exceptions include the north equatorial bright band, possibly the southern storm alley around −45° latitude, and the great storm in the March 2011 map. These contrast with time variability seen by the VLA in the late 1980s and early 1990s, where van der Tak et al. (1999) report substantial latitudinal brightness variations in both hemispheres. We also see a southern hemisphere that is somewhat (∼1%) cooler than the north, while van der Tak et al. see a southern hemisphere from 1990 to 1995 that was brighter than the northern by 5%, at wavelengths of 2 and 6 cm. Some of the variability may be due to the different wavelengths used and the insensitivity of the 2.2-cm emission to atmospheric temperature and subcloud ammonia variations; however, the 2-cm VLA banding seen earlier by van der Tak et al. is clearly different than the 2005–2011 results presented here and implies the existence of long-term variability in our "quiescent" bands. For example, a storm equivalent to the 2010–2011 storm might have been present in the southern hemisphere at that time. Unlike the northern storm, however, it must have persisted for 5 years to explain the observations, which we consider unlikely. One more global equatorial map is planned for 2015, which will extend our time base to 10 years if successful, allowing us to further address the question of long-term variability. Finally, improvements to the VLA and the coming on-line of new millimeter-wavelength arrays should enable this question to be pursued for many more years, using the present results as a baseline.

We have limited our interpretation to that allowed by the present observations themselves, noting that L13 goes more thoroughly into interpretations involving both the horizontal the vertical ammonia distribution and relates them to dynamical models for the circulations. We also remark that the 2.2-cm radiometric mapping campaign was part of a combined effort with the Visual Infrared Mapping Spectrometer (VIMS) on Cassini that was begun after the 2005 radiometer mapping effort proved successful. This consisted of VIMS observations of the same regions imaged by the microwave radiometer both before and after the pass so that wind-corrected overlays of the infrared maps with the microwave maps could be examined. Since the VIMS instrument observes the same pressure range of the atmosphere but is affected by other constituents (clouds and haze in particular), questions concerning circulations and related processes can be examined more fully. Work is currently in progress to compare the VIMS and microwave mapping. Further, the calibrated data and derived maps from the present work have been submitted to the Atmospheres Node of the Planetary Data System and will be available for comparative studies in general around the time of the publication of this paper. Lastly, interpretations of the present results are limited because only one frequency was used. Improved VLA capabilities and future missions using multiple microwave frequencies can achieve much more in understanding the deep circulations and vertical structure of the microwave-active constituents ammonia and water. For example, the Juno mission currently on route for arrival at Jupiter in 2016 carries a six-frequency microwave radiometer that will observe Jupiter's deep atmosphere to pressures greater than 100 bars with such a goal (Janssen et al., in preparation).

Acknowledgments

This research was conducted at the Jet Propulsion Laboratory (JPL), California Institute of Technology, under contract with the National Aeronautics and Space Administration (NASA). It is partly based upon work supported by NASA under Grant No. 10-CDAP10-0051 issued through the Cassini Data Analysis and Participating Scientist (CDAPS) Program. We acknowledge Sushil Atreya, Lena Adams, and Virgil Adumantroi for their invaluable contributions to the Juno Atmospheric Microwave Radiative Transfer (JAMRT) program, P. Steffes for discussions on the microwave absorption of ammonia in the Saturn atmosphere, Scott Bolton, Steve Levin, and the Juno project for their encouragement of this work, Alice Le Gall for her contributions to the calibration, Bryan Butler for discussion of the capabilities of ground-based interferometers, and Glenn Orton for useful discussions on sources of microwave absorption as well as related visual and infrared observations of giant planet atmospheres. We also gratefully acknowledge the Cassini RADAR team in general for their support, along with those who designed, developed and operate the Cassini/Huygens mission, which is a joint endeavor of NASA, the European Space Agency (ESA), and the Italian Space Agency (ASI) and is managed by JPL/Caltech under a contract with NASA.

References

Allison, M., 1990. Planetary waves in Jupiter's equatorial atmosphere. Icarus 83, 282–307.

Arregi, J. et al., 2006. Phase dispersion relation of the 5-micron hot spot wave from a long term study of Jupiter in the visible. J. Geophys. Res. 111, E09010. http://dx.doi.org/10.1029/2005JE002653.

Atreya, S.K., 1986. Atmospheres and ionospheres of outer planets and their satellites. Springer-Verlag.

Atreya, S.K., 2010. Atmospheric moons Galileo would have loved. In: Galileo's Medicean Moons – Their Impact on 400 Years of Discovery. Cambridge University Press, pp. 130–140 (Chapter 16).

Baines, K.H. et al., 2009. Storm clouds on Saturn: Lightning-induced chemistry and associated materials consistent with Cassini/VIMS spectra. Planet. Space Sci. 57, 1650–1658.

Berge, G.L., Gulkis, S., 1976. Earth-based radio observations of Jupiter: Millimeter to meter wavelengths. In: Gehrels, T. (Ed.), Jupiter. Univ. of Arizona Press, Tucson, pp. 621–692.

Birnbaum, G., Borysow, A., Orton, G.S., 1996. Collision-induced absorption of H_2–H_2 and H_2–He in the rotational and fundamental band for planetary applications. Icarus 123, 4–22.

Borysow, A., Frommhold, L., 1986. Theoretical collision-induced rototranslational absorption spectra for the outer planets: H_2–CH_4 pairs. Astrophys. J. 304, 849–865.

Briggs, F.H., Sackett, P.D., 1989. Radio observations of Saturn as a probe of its atmosphere and cloud structure. Icarus 80, 77–103.

Cottini, V. et al., 2012. Spatial and temporal variations in Titan's surface temperature from Cassini CIRS observations. Planet. Space Sci. 60, 62–71.

de Pater, I., 1990. Radio images of the planets. Annu. Rev. Astron. Astrophys. 28, 347–399.

de Pater, I., Dickel, J.R., 1982. New information on Saturn and its rings from VLA multifrequency data. In: Proceedings of Planetary Rings/Anneaux des Planetes Conference, Toulouse, France, August 1982 (abstract).

de Pater, I., Dickel, J.R., 1991. Multifrequency radio observations of Saturn at ring inclination angles between 5° and 26°. Icarus 94, 474–492.

de Pater, I., Massie, S.T., 1985. Models of the millimeter–centimeter spectra of the giant planets. Icarus 62, 143–171.

de Pater, I., Dunn, D., Zahnle, K., Romani, P.N., 2001. Comparison of Galileo probe data with ground-based radio measurements. Icarus 149, 66–78.

Deboer, D.R., Steffes, P.G., 1994. Laboratory measurements of the microwave properties of H_2S under simulated jovian conditions with an application to Neptune. Icarus 109, 352–366.

Deveraj, K., 2011. The Centimeter- and Millimeter-Wavelength Ammonia Absorption Spectra under Jovian Conditions. Ph.D. thesis, Georgia Institute of Technology, Atlanta.

Dunn, D.E., Molnar, L.A., Fix, J.D., 2002. More microwave observations of Saturn: Modeling the ring with a Monte Carlo radiative transfer code. Icarus 160, 132–160.

Duong, D., 2011. The Complex Dielectric Properties of Aqueous Ammonia from 2 GHz to 8.5 GHz in Support of the NASA Juno Mission. M.S. Thesis, Georgia Institute of Technology, Atlanta, GA.

Dyudina, U.A., Ingersoll, A.P., Ewald, S.P., Porco, C.C., Fischer, G., Kurth, W., Desch, M., Del Genio, A., Barbara, J., Ferrier, J., 2007. Lightning storms on Saturn observed by Cassini ISS and RPWS during 2004–2006. Icarus 190, 545–555.

Elachi, C. et al., 2004. RADAR: The Cassini Titan radar mapper. Space Sci. Rev. 115, 71–110.

Fletcher, L.N., Baines, K.H., Momary, T.W., Showman, A.P., Irwin, P.G.J., Orton, G.S., Roos-Serote, M., Merlet, C., 2011. Saturn's tropospheric composition and clouds from Cassini/VIMS 4.6–5.1 μm nightside spectroscopy. Icarus 214, 510–533.

Fulchignoni, M. et al., 2005. Titan's physical characteristics measured by the Huygens Atmospheric Structure Instrument (HASI). Nature 438, 785–791.

Grossman, A.W., 1990. Microwave Imaging of Saturn's Deep Atmosphere and Rings. Ph.D. thesis, California Institute of Technology.

Grossman, A.W., Muhleman, D.O., Berge, G.L., 1989. High resolution microwave observations of Saturn. Science 245, 1211–1215.

Gulkis, S., Poynter, R., 1972. Thermal radio emission from Jupiter and Saturn. Phys. Earth Planet. Interiors 6, 36–43.
Gulkis, S.R., McDonough, T.R., Craft, H., 1969. The microwave spectrum of Saturn. Icarus 10, 421–427.
Hanley, T.R., Steffes, P.G., Karpowicz, B.M., 2009. A new model of the hydrogen and helium broadened microwave opacity of ammonia based on extensive laboratory measurements. Icarus 202, 316–335.
Hoffman, J.P., Steffes, P.G., DeBoer, D.R., 2001. Laboratory measurements of the microwave opacity of phosphine: Opacity formalism and application to the atmospheres of the outer planets. Icarus 152, 172–184.
Janssen, M.A., 1993. An introduction to the passive microwave remote sensing of atmospheres. In: Janssen, M. (Ed.), Atmospheric Remote Sensing by Microwave Radiometry. Wiley & Sons, New York, pp. 1–35 (Chapter 1).
Janssen, M.A., Hofstadter, M.D., Gulkis, S., Ingersoll, A.P., Allison, M., Bolton, S.J., Kamp, L.W., 2005. Microwave remote sensing of Jupiter's atmosphere from an orbiting spacecraft. Icarus 173, 447–453.
Janssen, M.A., Lorenz, R.D., West, R., Paganelli, F., Lopes, R.M., Kirk, R.L., Elachi, C., Wall, S.D., Johnson, W.T.K., Anderson, Y., Boehmer, R.A., Callahan, P., Gim, Y., Hamilton, G.A., Kelleher, K.D., Roth, L., Stiles, B., Le Gall, A.the Cassini Radar Team, 2009. Titan's surface at 2.2-cm wavelength imaged by the Cassini RADAR radiometer: Calibration and first results. Icarus 200, 222–239.
Jennings, D.E. et al., 2009. Titan's surface brightness temperatures. Astrophys. J. 691, L103–L105.
Karpowicz, B.M., Steffes, P.G., 2011a. In search of water vapor on Jupiter: Laboratory measurements of the microwave properties of water vapor under simulated jovian conditions. Icarus 212, 210–213.
Karpowicz, B.M., Steffes, P.G., 2011b. Corrigendum to "In search of water vapor on Jupiter: Laboratory measurements of the microwave properties of water vapor under simulated jovian conditions" [Icarus 212 (2011) 210–213]. Icarus 214, 783.
Klein, M.J., Gulkis, S., 1978. Jupiter's atmosphere: Observations and interpretation of the microwave spectrum near 1.25-cm wavelength. Icarus 35, 44–60.
Laraia, A., Ingersol, A.P., Janssen, M.A., Gulkis, S., Oyafuso, F.A., Allison, M.D., 2013. Analysis of Saturn's thermal emission at 2.2-cm wavelength: Spatial distribution of ammonia vapor. Icarus, this issue.
Lindal, G.F., Sweetnam, D.N., Eshleman, V.R., 1985. The atmosphere of Saturn: An analysis of the Voyager radio occultation measurements. Astron. J. 90, 1136–1146.
Lorenz, R.D., 1998. Preliminary measurements of the cryogenic dielectric properties of water-ammonia ices: Implications for radar observations of ice satellites. Icarus 136, 344–348.
Mayer, C.H., McCullough, T.P., Sloanaker, R.M., 1958. Observations of Mars and Jupiter at a wavelength of 3.15 cm. Astrophys. J. 127, 11–16.
Mohammed, P., 2004. Laboratory measurements of the W band (3.2 mm) properties of phosphine (PH_3) and ammonia (NH_3) under simulated conditions of the outer planets. J. Geophys. Res. 109, 1–9.
Orton, G., Gustafsson, M., Burgdorf, M., Meadows, V., 2007. A revised ab initio model for collision-induced H_2–H_2 absorption. Icarus 189, 455–459.
Porco, C.C. et al., 2005. Cassini imaging science: Initial results on Saturn's atmosphere. Science 307, 1243–1247.
Sanchez-Lavega, A., Rojas, J.F., Sada, P.V., 2000. Saturn's zonal winds at cloud level. Icarus 147, 405–420.
Schloerb, F.P., Muhleman, D.O., Berge, G.L., 1979. Interferometric observations of Saturn and its rings at a wavelength of 3.71 per cm. Icarus 39, 214–231.
Thornton, D.D., Welch, W.J., 1963. 8.35 mm radio emission from Jupiter. Icarus 2, 228–232.
van der Tak, F., de Pater, I., Silva, A., Millan, R., 1999. Time variability in the radio brightness distribution of Saturn. Icarus 142, 125–147.
West, R. et al., 2009. Cassini RADAR sequence planning and instrument performance. IEEE Trans. Geosci. Remote Sensing 47, 1777–1795.
Wrixon, G.T., Welch, W.J., 1970. The millimeter wave spectrum of Saturn. Icarus 13, 163–172.